POLITECNICO
MILANO 1863

SCUOLA DI INGEGNERIA INDUSTRIALE
E DELL'INFORMAZIONE

Monolithic and hybrid semiconductor photonic devices for quantum information

Tesi di Laurea Magistrale in
Engineering Physics - Ingegneria Fisica

Author: **Lorenzo Lazzari**

Student ID: 944073
Advisor: Prof. Roberto Osellame
Co-advisor: Prof. Sara Ducci
Academic Year: 2021-22

Acknowledgments

Ringraziamenti/Remerciements

Il primo ringraziamento non può che andare a Sara Ducci, senza la quale questa tesi non sarebbe mai venuta alla luce: se il tuo spessore umano è risultato evidente dal primo incontro, in questi mesi ho avuto modo di conoscere anche la tua dimensione professionale, di guida presente, paziente e sicura. Grazie per avermi accolto e fatto sentire valorizzato e sereno, nonché per la possibilità di continuare a lavorare insieme: mi auguro di essere all'altezza di quanto ricevuto.

Da lato Politecnico, uno speciale ringraziamento va al prof. Roberto Osellame, per aver accettato di accompagnarmi in quanto relatore in questo progetto: grazie per la sua disponibilità e professionalità, per la prontezza nell'accogliere le mie richieste anche dalla distanza. Voglio poi ringraziare il prof. Ermanno Pinotti, per l'infinita pazienza con la quale mi ha aiutato a realizzare e gestire dal punto di vista burocratico questo percorso di tesi.

Du côté MPQ, je tiens tout particulièrement à remercier Florent Baboux, une référence précieuse et toujours disponible, et Maria Amanti, pour ses entretiens éclairants. Merci également à Luca Guidoni et Jean-Pierre Likforman pour leur indispensable soutien technique. Merci ensuite à Nathalie Merlet, Sandrine Di Concetto et Jocelyne Moreau pour avoir patiemment résolu tous les problèmes administratifs rencontrés.

Merci à Frédéric Boeuf : ça a été un plaisir de collaborer ces derniers mois, et je suis sûr que ce le sera pour les années à venir. En particulier, je te remercie pour tes remarques, toujours très pertinentes, et pour avoir intercédé personnellement auprès de ST afin que la possibilité d'obtenir un doctorat devienne une réalité. Merci également à Fabrice Raineri, pour ses précieux enseignements en salle blanche et pour sa confiance à poursuivre ce chemin ensemble.

On pourrait dire qu'il s'agit d'une thèse à quatre mains, car j'ai eu la chance de travailler à côté d'une personne spéciale : merci Jérémie de m'avoir appris tant de choses, de la table d'optique à la conjugaison des verbes en français, de comment être écologiste à comment

se sentir bien à Paris. ça a été un plaisir et un honneur de partager cette aventure avec toi, et je te souhaite toute la chance possible dans la conclusion de ton parcours : tu le mérites. Merci également aux autres collègues et amis de l'équipe QITe : Arnault, toujours prêt à donner un coup de main et à résoudre les problèmes informatiques ; Félicien, qui n'a mis que quelques mois à se faire aimer et à me convaincre de rester ici ; Othmane, avec qui je peux partager une passion pour le foot (une denrée rare chez les physiciens); Iannis, pour avoir toujours apporté gaieté et gentillesse au bureau et avoir fait de moi un "cathaphile"; Théo et Derwell, pour votre sympathie et pour nous prêter tout ce dont nous avons besoin. Merci ensuite à tous les gars de l'équipe DON, avec qui c'est toujours un plaisir de discuter de physique autour d'un café pendant la pause déjeuner ou d'une bière après le travail.

Questi mesi non sarebbero certo stati la stessa cosa senza le fantastiche persone che ho incontrato lungo la strada, specialemente il gruppo di amici italiani: vi ringrazio per le avventure vissute insieme e per aver dato un'anima a questa strana Parigi, da Rue des Moines e Belleville fino a Cachan. Thanks also to all the international friends from the Erasmus and met along the way, especially to Jesus, for hosting me when I first arrived in Paris.

Questo momento segna la conclusione di un percorso iniziato 6 anni fa, ma probabilmente anche molto prima. Sono anni che credo di aver vissuto appieno, non privi di momenti bui e piccoli grandi rimorsi, ma nei quali sono cresciuto, ho imparato molto e ho avuto l'occasione di apprezzare tanta della bellezza che mi circonda. Se oggi sono quello che sono, ritengo sia soprattutto grazie alle persone che questo percorso l'hanno condiviso con me. Grazie agli amici del liceo, della Seriana e Seriana Birra, dell'oratorio e a tutti coloro che hanno contribuito a dare colore alla mia vita e che, anche se ora mi trovo un po' più lontano, rappresentano sempre il mio porto sicuro.

Il ringraziamento più grande va alla mia famiglia, che mi ha sempre e incondizionatamente sostenuto e incoraggiato, ispirato e spronato ad essere felice prima che realizzato e a fare tesoro di quanto ricevuto, regalandomi quella serenità e quel supporto senza i quali non sarei potuto arrivare dove sono ora. Spero che questo possa, almeno in piccola parte, ripagare dei tanti sacrifici fatti per consentirmi di essere qui.

Grazie infine a Laura, per aver scelto di crescere insieme e di iniziare, quasi allo sbaraglio, questa inattesa avventura. Sei stata presenza costante, mi hai spinto a non aver paura di guardare sempre un po' più in là e mi hai insegnato, magari senza accorgertene, molto più di quanto pensi. A quello che verrà, quindi: *dans notre rue*.

Abstract

Photonic quantum technologies represent a promising platform for several quantum information applications, ranging from long-distance communications to the simulation of complex phenomena. On the one hand, the advantages offered by single photons (robustness to decoherence, propagation over very large distances) make them the candidate of choice to carry quantum information for many applications. On the other hand, the emergence of integrated quantum photonics has led to the demonstration of photon manipulation on complex circuits with near-perfect phase stability. Among the various investigated platforms, AlGaAs semiconductor chips emerge for their strong nonlinearity and direct bandgap, for their capability of generating non-classical states of light at room temperature and for their high integrability. Here we demonstrate a broadband photon pair source consisting of an AlGaAs waveguide based on Bragg reflectors, supporting all three types of possible phase-matching (PM) and thus providing a high versatility in the polarization of the emitted photons in view of various applications. The nonlinear response of the device is first characterized through second harmonic generation (SHG) measurements: the three types of available PM are retrieved on the same chip, with type 0 and type 2 PM offering a considerably high conversion efficiency ($\sim$120%$\mathrm{W}^{-1}\mathrm{cm}^{-2}$).

Photon pairs are then generated via spontaneous parametric down-conversion (SPDC), with a measured brightness of $10^3\mathrm{s}^{-1}\mathrm{mW}^{-1}\mathrm{nm}^{-1}$ over a bandwidth larger than 80nm. The non-classicality of the emitted state is characterized through an energy-time entanglement measurement, using a fibred Franson interferometer in the folded configuration. The broadband nature of the produced biphoton states combined with the PM versatility of the source offers a testbed to investigate the interplay of chromatic and polarization dispersion in the energy-time entanglement visibility. Visibilities up to 99% are observed for both type 0 and type 2 generation processes. This high visibility, together with its intrinsic robustness to environment perturbations, makes the generated state an appealing resource for quantum information applications, especially in quantum communication.

Besides the intrinsic interest, this AlGaAs source is envisioned for its integration with Silicon-on-Insulator (SOI) photonic circuits, in order to leverage the strengths of each material platform. The design and fabrication of a hybrid AlGaAs/SOI device has already

been accomplished, together with the optical mode transfer via adiabatic coupling. The demonstration of the quantum properties of this device is the next step towards the validation of the device as hybrid platform to generate and manipulate quantum states of light.

Keywords: *integrated photonics, AlGaAs waveguide, energy-time entanglement, Franson interferometer, hybrid photonic circuits*

Abstract in italiano

Le tecnologie quantistiche fotoniche rappresentano una piattaforma promettente per diverse applicazioni nell'ambito dell'informazione quantistica, che vanno dalle comunicazioni a lunga distanza alla simulazione di fenomeni complessi. Da un lato, i vantaggi offerti dai singoli fotoni (robustezza alla decoerenza, propagazione su distanze molto grandi) li rendono il candidato d'elezione per trasportare informazioni quantistiche per un'ampia varietà di applicazioni. D'altra parte, l'emergere della fotonica quantistica integrata ha portato alla dimostrazione della manipolazione di fotoni in circuiti complessi con una stabilità di fase quasi perfetta. Tra le varie piattaforme studiate, i chip a semiconduttore in AlGaAs emergono per la loro forte non linearità e il bandgap diretto, per la loro capacità di generare stati non classici di luce a temperatura ambiente e per la loro elevata integrabilità. Qui si dimostra una sorgente di coppie di fotoni a banda larga costituita da una guida d'onda in AlGaAs basata su riflettori di Bragg, che supporta tutti e tre i tipi di phase-matching (PM) possibili e fornisce quindi un'elevata versatilità nella polarizzazione dei fotoni emessi, in vista di varie applicazioni. La risposta non lineare del dispositivo viene innanzitutto caratterizzata attraverso misure di generazione di seconda armonica (SHG): i tre tipi di PM disponibili vengono rilevati sullo stesso chip, con i PM di tipo 0 e 2 che offrono un'efficienza di conversione notevole ($\sim$120%$\mathrm{W^{-1}cm^{-2}}$).

Le coppie di fotoni vengono poi generate tramite la conversione parametrica spontanea (SPDC), con una luminosità misurata di $10^3\mathrm{s^{-1}mW^{-1}nm^{-1}}$ su una larghezza di banda maggiore di 80 nm. La non classicità dello stato emesso è stata caratterizzata attraverso una misura di entanglement energia-tempo, utilizzando un interferometro di Franson fibrato in configurazione *folded*. La natura a banda larga degli stati bifotonici prodotti, combinata con la versatilità in termini di PM della sorgente, offre un banco di prova per studiare l'interazione tra dispersione cromatica e polarizzazione nella visibilità dell'entanglement energia-tempo. Si osservano visibilità fino al 99% sia per i processi di generazione di tipo 0 che di tipo 2. Questa elevata visibilità, insieme alla sua intrinseca robustezza alle perturbazioni ambientali, rende lo stato generato una risorsa appetibile per applicazioni nell'informazione quantistica, in particolare nella comunicazione quantistica.

Oltre al suo interesse intrinseco, questa sorgente in AlGaAs è concepita per l'integrazione

con circuiti fotonici in silicio-su-isolante (SOI), al fine di sfruttare i punti di forza di ciascuna piattaforma materiale. La progettazione e la fabbricazione di un dispositivo ibrido AlGaAs/SOI sono già state realizzate, insieme al trasferimento dei modi ottici tramite accoppiamento adiabatico. La dimostrazione delle proprietà quantistiche di tale dispositivo rappresenta un prossimo passo verso la sua validazione come piattaforma ibrida capace di generare e manipolare stati quantistici di luce.

Parole chiave: *fotonica integrata, guide d'onda AlGaAs, entanglement energia-tempo, interferometro di Franson, circuiti fotonici ibridi*

Contents

Introduction

Following the cutting-edge development of the theoretical foundations of quantum mechanics at the beginning of last century, scientists were able to describe under a new lens some of the unsolved problems of classical physics and hence to predict unimagined electronic and optical properties of materials. This led, in the 1960's, to the invention of new history-changing technologies, such as the laser [1] and the transistor [2]. This process in known as *first quantum revolution*. Nowadays, we are living the so-called *second quantum revolution*, corresponding to the emergence of the domain of quantum information starting from the 1990's. Quantum information can be encoded in qubits, two-level systems representing the quantum analogous of the classical bit; in this way, the quantum properties of such physical systems – from state superposition and non-cloning theorem to entanglement – are exploited to overcome the limits of classical information protocols, pursuing, for example, the establishment of unconditionally secure communications, the creation of new computational tools to address classically unsolvable or inefficient algorithms, the proficient simulation of complex systems. This has been made possible thanks to the realization of single and entangled photon sources and detectors and to the development of nano-fabrication techniques, paving the way to the implementation of increasingly complex devices and measurements. The latest achievements obtained with these technologies range from the demonstration of the quantum computing advantage [3] to quantum key distribution on satellite infrastructures [4] and from loophole-free quantum non-locality [5] to the detection of gravitational waves making use of squeezed states of light [6].

Among all the currently available physical platforms for the development of quantum technologies, spanning from atomic and solid state systems to superconductive circuits, we focus our attention on photons. Thanks to their high speed and immunity to decoherence, they are particularly suited for carrying quantum information and are employed not only in quantum communication protocols but also in quantum simulation and computing [7]. Polarization entangled photons were used for the first experimental violation of Bell's inequality in 1981 [8], which proved the non-local nature of quantum entanglement, thus solving the Einstein-Podolsky-Rosen paradox [9]: this attested how the counter-intuitive

quantum properties of a system can represent useful resources, not only theoretical artifacts. On this line, the first protocol for quantum cryptography (BB84) was designed for photons and proposed in 1984 [10]. Experiments able to measure single and two-photon interference were set up by the end of the 1980's, demonstrating the wave-particle duality of light and enabling new experimental pathways based on interferometry, which led to novel methods and protocols to encode information [11] and to metrology applications [12]. As a further achieved milestone, photons were successfully employed for quantum teleportation in 1997 [13]. The development of sources of single or entangled photons, such as quantum dots [14] or parametric sources [15], has been a major objective of the last decades. The new available technologies assisted the accomplishment of cutting-edge results, as the demonstration of the quantum computing advantage in a photonic implementation [16], the efficient simulation of complex molecular dynamics [17] and the already mentioned detection of gravitational waves.

A large variety of degrees of freedom of photons can be used to implement qubits in quantum information protocols [7], such as polarization, arrival time at a detector, spatial path, frequency and orbital angular momentum. The efficient generation, manipulation, distribution and detection of such qubits is the final goal towards which is devoted most of the research effort of the last two decades, combining fundamental studies of quantum phenomena with practical engineering challenges. Several material platforms are investigated for the implementation of scalable, robust, controllable, low-power consumption and high fabrication yield devices featuring increasingly complex functions, being the ultimate target the realization of miniaturized chips able to perform all those tasks. Integrated photonics [18] relies, indeed, on the possibility to confine and to guide light at the micrometer scale via nano-fabricated waveguides; nonlinear effects can be exploited for the generation of quantum states, which can be directly manipulated through thermal or electro-optic phase shifters and directional couplers, and eventually measured on-chip with integrated single-photon detectors.

In this manuscript, we treat the implementation of integrated photonic devices using AlGaAs, a semiconductor III-V material: we describe the design and implementation of a parametric source of entangled photon pairs at room temperature and its characterization in terms of nonlinear performances and entanglement quality, in view of its application for quantum information. Furthermore, we propose a hybrid device resulting from the heterogeneous integration of the AlGaAs source with a silicon-on-insulator (SOI) circuit, in the aim of merging the two material platforms and leveraging their complementary assets. The hybridization is, in fact, one of the investigated ways to achieve the realization of a single chip featuring all the previously mentioned functions. In particular:

Chapter 1 offers an essential outlook on the theoretical concepts, introducing the nonlinear optical processes, with particular attention on the spontaneous parametric down-conversion. Quantum entanglement is then theoretically derived and discussed in some of the forms in which it can appear when considering photon pairs. Finally, a brief overview of the state of the art photon-pair sources is proposed, presenting the main material platforms and the characterizing figures of merit.

Chapter 2 is devoted to the description of our photon-pair sources: Bragg reflectors AlGaAs waveguides. Design, working principles and fabrication procedure are discussed in details, together with the properties of the generated quantum state.

Chapter 3 presents the experimental results obtained for the source characterization, in terms of optical losses, nonlinear conversion efficiency and photon-pair generation rate. Furthermore, we discuss the measurement of the energy-time entanglement visibility of the produced quantum state, via a fibered Franson interferometer in the folded configuration.

Chapter 4 introduces the challenge of the III-V/SOI integration. The hybrid AlGaAs/SOI device is here presented: we describe the design, the fabrication procedure and the working principles, together with the first experimentally obtained results. In conclusion, the short and long term perspectives are briefly presented.

1 | Theoretical background

In this chapter, we give an overview of the main theoretical concepts employed in the presented work. The first section offers a brief introduction about nonlinear optics, with focus on second order processes and the importance of the phase-matching condition; the second section describes the process of Spontaneous Parametric Down-Conversion (SPDC), explaining its connection with quantum entanglement, which is here introduced; finally, the last section is devoted to a review of photon-pair sources, and the tools used to characterize their quality.

1.1. Nonlinear optical processes

When intense electromagnetic fields interact with matter, we observe optical phenomena that can only be described with nonlinear equations. Such intense fields can be produced with lasers, therefore nonlinear optics is a quite recent branch of physics: the first laser was demonstrated in 1960 by Maiman [1] and the first observation of a nonlinear optical process by Franken was published in 1961 [19]. Since then, the domain of nonlinear optics has never ceased to develop and bring new applications, including nonlinear integrated quantum photonics, which is the topic of this thesis.

A nonlinear optical response of the medium means that new fields are generated at frequencies different from the excitation one. In a basic picture, matter can be seen as an ensemble of microscopic dipoles (the atoms with positively charged nuclei surrounded by negatively charged electrons) that behave as oscillators: high order harmonics appear when the field intensity increases, acting as new radiation sources at new optical frequencies. This *frequency conversion* can be described with a semi-classical treatment, meaning that we consider the quantum nature of the medium while we use the classical electromagnetic field theory for the light; however, for a rigorous description, an approach based on quantum electrodynamics, in which both the medium and the field are quantized systems, is needed, and we will use it in section 1.2.1.

1.1.1. Nonlinear polarization

The response of the medium to an external electromagnetic field can be, in practice, described by the electric polarization vector, $\mathbf{P}(\mathbf{r}, t)$; this is, by definition, related to the incoming field, $\mathbf{E}(\mathbf{r}, t)$, and to the electric displacement field, $\mathbf{D}(\mathbf{r}, t)$, by:

$$\mathbf{D} = \epsilon_0 \mathbf{E} + \mathbf{P} \tag{1.1}$$

where ϵ_0 is the free space electric permittivity. Polarization is linear with the applied field in low intensity regime; when the magnitude increases, higher order responses can be mathematically included with a power series expansion:

$$\mathbf{P} = \underbrace{\epsilon_0 \chi^{(1)} \cdot \mathbf{E}}_{\mathbf{P}_L} + \underbrace{\epsilon_0 \chi^{(2)} : \mathbf{E}^2 + \epsilon_0 \chi^{(3)} \vdots \mathbf{E}^3 + \dots}_{\mathbf{P}_{NL}} \tag{1.2}$$

where $\chi^{(m)}$ is the mth-order electrical susceptibility tensor of the medium, whose amplitude decreases rapidly with the nonlinear order[1]. That is why, when the external field is weak, the response is essentially linear, and characterized by $\chi^{(1)}$, which is related to the refractive index of the material, defined as $n = \sqrt{1 + \mathrm{Re}(\chi^{(1)})}$. The second part of Equation (1.2) becomes relevant in high field intensity regimes, and models the higher orders processes. In particular, $\chi^{(2)}$ drives the second order nonlinear response, which is quadratic with the interacting field, giving rise to three-wave mixing processes, as will be discussed later; $\chi^{(3)}$ is the third order susceptibility, driving four-wave mixing processes. In this work, we will only consider second order processes, thus, in the following, we will assume:

$$\mathbf{P}_{NL} = \epsilon_0 \chi^{(2)} : \mathbf{E}^2. \tag{1.3}$$

For a deeper physical interpretation of $\mathbf{P}_{NL}$ we need to recall Maxwell's equations for a non-magnetic dielectric material in the absence of charges and currents:

$$\begin{cases} \nabla \times \mathbf{E} + \dfrac{\partial \mathbf{B}}{\partial t} = \mathbf{0}, & \text{(1.4a)} \\ \nabla \times \mathbf{B} - \mu_0 \dfrac{\partial \boldsymbol{D}}{\partial t} = \mathbf{0}, & \text{(1.4b)} \end{cases}$$

where $\mathbf{B}$ is the magnetic induction field and μ_0 the magnetic permeability in vacuum. When taking the curl of (1.4a) and plugging it into (1.4b) we obtain a wave equation

[1] $|\chi^{(1)}| \sim 1$, $|\chi^{(2)}| \sim 10^{-11}$ m/V, $|\chi^{(3)}| \sim 10^{-22}$ m^2/V^2 for the dielectric media used in this work, as reported in [20]

containing the relation between electrical field and induced polarization:

$$\nabla^2\mathbf{E} - \frac{n^2}{c^2}\frac{\partial^2\mathbf{E}}{\partial t^2} = \mu_0\frac{\partial^2\mathbf{P}_{NL}}{\partial t^2}, \tag{1.5}$$

with c speed of light in vacuum. The nonlinear polarization term acts here as a source term for new field components, in principle at different frequencies with respect to the driving one, as a consequence of the interaction with the medium.

1.1.2. Three-wave mixing

Let us consider, for the sake of simplicity, an isotropic and homogeneous medium: in this case, $\chi^{(2)}$ is no more a tensor, but a scalar. Therefore, Equation (1.3) turns into:

$$P_{NL}(t) = \epsilon_0\chi^{(2)}E^2(t), \tag{1.6}$$

where we can assume the electric field to be the sum of two monochromatic fields at frequencies ω_1, ω_2 with $\omega_1 > \omega_2$:

$$E(t) = \frac{1}{2}\left(E_1e^{i\omega_1 t} + E_2e^{i\omega_2 t} + c.c.\right). \tag{1.7}$$

Thus, when plugging this field expression in (1.6), we obtain:

$$\begin{aligned} P_{NL}(t) = \epsilon_0\chi^{(2)}\frac{1}{4}\Bigg[& \underbrace{E_1^2e^{2i\omega_1 t} + E_2^2e^{2i\omega_2 t}}_{SHG} \\ & + \underbrace{2E_1E_2e^{i(\omega_1+\omega_2)t}}_{SFG} + \underbrace{2E_1E_2^*e^{i(\omega_1-\omega_2)t}}_{DFG} \\ & + \underbrace{|E_1|^2 + |E_2|^2}_{OR} + c.c.\Bigg]. \end{aligned} \tag{1.8}$$

As we can see from the terms in Equation (1.8), second order nonlinearity is responsible of a series of possible interactions between three fields, hence the expression *three-wave mixing* processes. In a quantized picture, three photons, each one in a given frequency mode (ω_1, ω_2 or ω_3), will interact within the nonlinear medium leading to the creation or annihilation of one of them (respectively, upward and downward arrows in Figure 1.1). Note that the only available processes are the ones respecting energy conservation, which means in our example:

$$\hbar\omega_3 = \hbar\omega_1 + \hbar\omega_2 \tag{1.9}$$

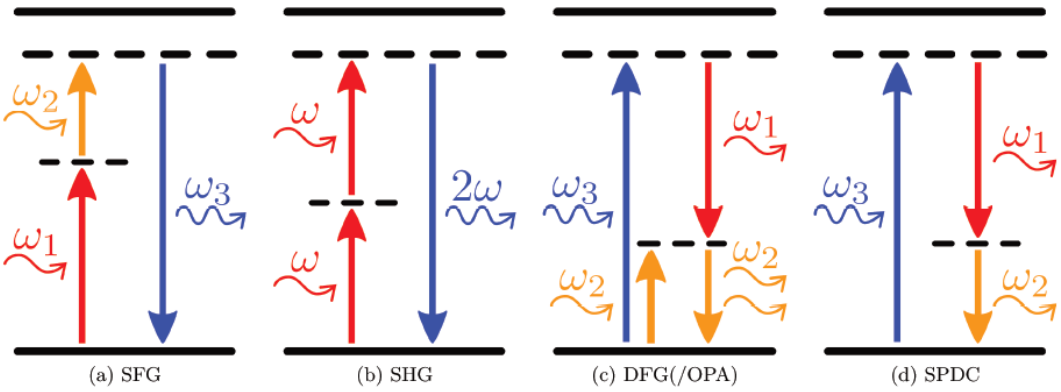

Figure 1.1: Sketch of the three-wave mixing processes: (a) SFG; (b) SHG; (c) DFG and OPA; (d) SPDC. Solid black lines represent real energy levels of the medium, while dashed black lines correspond to the virtual states of the transitions. From [21].

with $\hbar$ as the reduced Planck's constant. The available second order processes are then:

SFG: Sum Frequency Generation, when two fields at frequencies ω_1 and ω_2 produce a third field at $\omega_3 = \omega_1 + \omega_2$ (Figure 1.1.a, second underbraced term in Equation (1.8)).

SHG: Second Harmonic Generation, when a pump field at frequency ω interacts with the medium and generates a field at double the frequency, 2ω (Figure 1.1.b, first underbraced terms in Equation (1.8)); it is the degenerate case of SFG.

DFG: Difference Frequency Generation, when the result of the interaction between the two fields (at ω_3 and ω_2) is a field with a lower frequency than the starting ones ($\omega_1 = \omega_3 - \omega_2$); to preserve energy conservation, the lower frequency pump field is amplified (**OPA**, **Optical Parametric Amplification** process – Figure 1.1.c, third underbraced term in Equation (1.8) when replacing E_1 with E_3).

SPDC: Spontaneous Parametric Down-Conversion, when, triggered by vacuum fluctuations, a photon at frequency ω_3 spontaneously annihilates, instantaneously generating two photons at frequencies ω_1 and ω_2 (Figure 1.1.d).

The last underbraced term in Equation (1.8) stands for the **Optical Rectification** (**OR**) process, which is not of interest for this work.

1.1.3. Phase-matching condition

The three electric fields involved in three-wave mixing processes can be written as:

$$\mathbf{E}_i(z,t) = \frac{1}{2}\left[\mathbf{A}_i(z)e^{i(\omega_i t - k_i z)} + c.c.\right], i = 1,2,3, \tag{1.10}$$

where we have expressed the dependence on the propagation direction z, and k_i is the modulus of the wave-vector of the field at frequency ω_i ($k_i = n_i\omega_i/c$, with n_i the refractive index at frequency ω_i), whose direction is, by definition, coincident with the one of propagation. These could be, for example, the fields involved in the SFG process introduced in the last section ($\omega_1 + \omega_2 = \omega_3$). When plugging this field expression in Equation (1.5), under the slowly varying envelope approximation[2], we obtain a set of nonlinear coupled differential equations, one per each frequency component:

$$\begin{cases} \dfrac{dA_1}{dz} = -i\dfrac{\omega_1}{n_1 c} d_{eff} A_2^*(z) A_3(z) e^{-i\Delta k z}, & \text{(1.11a)} \\ \dfrac{dA_2}{dz} = -i\dfrac{\omega_2}{n_2 c} d_{eff} A_1^*(z) A_3(z) e^{-i\Delta k z}, & \text{(1.11b)} \\ \dfrac{dA_3}{dz} = -i\dfrac{\omega_3}{n_3 c} d_{eff} A_1(z) A_2(z) e^{i\Delta k z}, & \text{(1.11c)} \end{cases}$$

where d_{eff} is the effective susceptibility, which will be described in Section 1.1.4, and $\Delta k = k_3 - k_1 - k_2$ is the *phase-mismatch*. This is a crucial factor, since, due to the travelling nature of the waves involved, this is an extended – not a point – interaction: if $\Delta k \neq 0$, an oscillating term will drive the evolution of the field amplitudes, affecting the efficiency of the frequency conversion process; on the other hand, if $\Delta k = 0$, the complex exponential will turn into a constant, and the amplitude of the generated field will increase with the propagation, thanks to the constructive interference. This is the *phase-matching* condition: among all the possible interactions satisfying energy conservation, only those satisfying this condition will occur efficiently within the medium.

When integrating Equation (1.11c) between $z = 0$ and $z = L$, being L the length of the medium, with the additional assumptions of absence of losses in the medium and undepleted pump[3], we obtain:

$$A_3(L) = -i\frac{\omega_3}{n_3 c} d_{eff} A_1 A_2 L e^{i\frac{\Delta k L}{2}} \mathrm{sinc}\left(\frac{\Delta k L}{2}\right). \tag{1.12}$$

From the latter expression, we can derive the intensity of the generated field:

$$I_3(L) = 2\frac{\omega_3^2}{n_1 n_2 n_3 \epsilon_0 c^3} d_{eff}^2 L^2 I_1 I_2 \mathrm{sinc}^2\left(\frac{\Delta k L}{2}\right). \tag{1.13}$$

[2]When the variation of the field amplitude in the propagation direction is small compared to the wavelength, that is: $\left|\frac{\partial^2 A}{\partial z^2}\right| \ll \left|\frac{2\pi}{\lambda}\frac{\partial A}{\partial z}\right|$.

[3]This means that the portion of the electromagnetic field power exchanged in the frequency conversion process is small. If the pump fields are at frequencies ω_1 and ω_2, in Equation (1.11c) $A_1(z) \simeq A_1(0) = A_1$ and $A_2(z) \simeq A_2(0) = A_2$ will be considered as constants under this assumption.

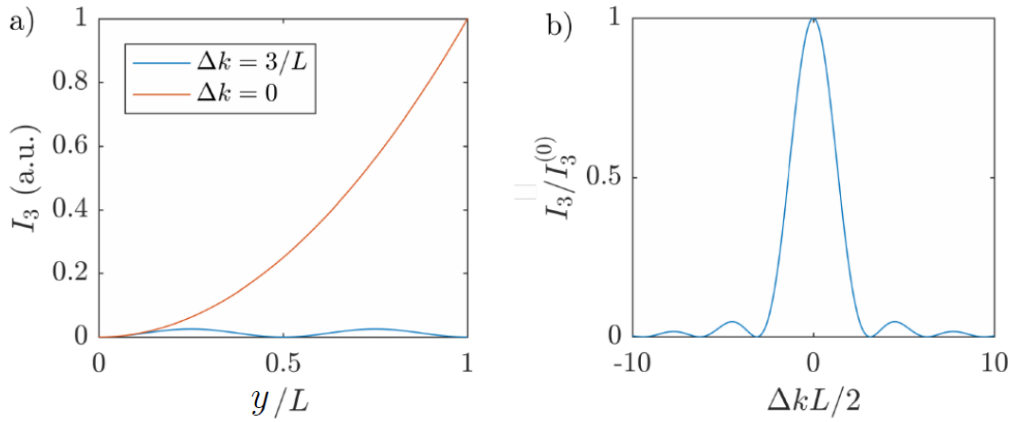

Figure 1.2: (a) SFG intensity as a function of the normalized propagation distance in case of phase-matching (red curve) and non-zero mismatch (blue curve); (b) SFG intensity for fized z as a function of the mismatch Δk.

In Figure 1.2.a we can see the intensity of the sum frequency generated field as a function of the propagation distance: note that this is valid only while the undepleted pump approximation is valid, so if $I_3 \ll I_1, I_2$; with reference to Equation (1.13), we define $I_3^{(0)} \equiv 2\frac{\omega_3^2}{n_1 n_2 n_3 \epsilon_0 c^3} d_{eff}^2 L^2 I_1 I_2$. In Figure 1.2.b, the characteristic squared cardinal sine profile of the process.

1.1.4. The second order nonlinear susceptibility tensor

In Section 1.1.3 we have introduced the effective susceptibility, d_{eff}; here, we will properly define it and describe some of its relevant characteristics. To do this, we first rewrite Equation (1.3) taking into account all Cartesian coordinates ($i, j, k \in x, y, z$) for the SFG process (ω_1, ω_2 pump fields with $\omega_1 + \omega_2 = \omega_3$):

$$P_{NL,i}(\omega_3) = \epsilon_0 \sum_{j,k} \chi^{(2)}_{i,j,k} E_j(\omega_1) E_k(\omega_2), \tag{1.14}$$

where we have assumed that the nonlinear susceptibility tensor does not depend on the frequency. This is the so-called Kleinmann's symmetry assumption, and it is valid when the frequencies involved in the nonlinear interaction are far from the resonance frequency of the medium itself, which is typically the case for the materials employed in this work. In addition, with respect to reciprocal interactions ($\omega_3 = \omega_1 + \omega_2$, $\omega_1 = \omega_3 - \omega_2$ and $\omega_2 = \omega_3 - \omega_1$), the $\chi^{(2)}$ tensor exhibits the following permutation symmetry:

$$\chi^{(2)}_{i,j,k} = \chi^{(2)}_{j,k,i} = \chi^{(2)}_{k,i,j}. \tag{1.15}$$

It is therefore possible to use a contracted notation with only two indices:

jk	11	22	33	23/32	13/31	12/21
l	1	2	3	4	5	6

which turns the nonlinear susceptibility from a 3-ranked tensor to a 3x6 matrix. If we now define the *effective susceptibility* as:

$$d_{il} \equiv \frac{1}{2}\chi_{il}^{(2)}, \tag{1.16}$$

we will have second order processes whenever $d_{il} \neq 0$, for given reference system, medium geometry and interacting fields.

1.2. Spontaneous parametric conversion and quantum entanglement

In Section 1.1.3 we introduced the process of Spontaneous Parametric Down-Conversion (SPDC), a three-wave mixing interaction in which a photon at frequency ω_3 is down-converted into two photons at frequencies ω_1 and ω_2, with $\omega_3 = \omega_1 + \omega_2$. In this section, we will describe this process under the lens of the quantum electrodynamics theory. In addition, we will define the property of entanglement, that is characteristic of the photons generated by SPDC, focusing our attention on the polarization and energy-time entanglements.

1.2.1. Spontaneous parametric down-conversion

The quantized description of the electromagnetic field passes through the definition of a proper Hamiltonian operator, whose physical meaning is to contain the total energy of the field. In the case of free radiation in vacuum, it takes the form [22]:

$$\hat{H}_R = \sum_l \hbar\omega_l \left(\hat{a}_l^\dagger \hat{a}_l + \frac{1}{2}\right), \tag{1.17}$$

where the index l points to any available mode of the field. This is functionally equivalent to the description of a quantum harmonic oscillator, where the quantum of energy is $\hbar\omega_l$ and each elementary excitation is a photon.

$\hat{a}_l$ and $\hat{a}_l^\dagger$ are the non-Hermitian operators describing, respectively, the annihilation and creation of one photon in mode l. In particular, being $|vac\rangle$ the vacuum state, if the state of a mode contains a single quantum of energy – or, which is the same, is populated by a

single photon –, we can write it as:

$$|1_l\rangle = \hat{a}_l^\dagger |vac\rangle. \tag{1.18}$$

It can be easily demonstrated that $|1_l\rangle$ is an eigenstate of the so-called *number operator* $\hat{N}_l = \hat{a}_l^\dagger \hat{a}_l$, with eigenvalue 1[4]. If we consider the case in which the mode is determined by the frequency (that is a continuous variable) and another discrete-valued property μ (for example, a linear vertical or horizontal polarization, $\mu \in H, V$), Equation (1.17) becomes:

$$\hat{H}_R = \sum_\mu \int \hbar \left[\hat{a}_\mu^\dagger(\omega)\hat{a}_\mu(\omega) + \frac{1}{2} \right] d\omega. \tag{1.19}$$

The SPDC process can be taken into account by introducing an interaction Hamiltonian, $\hat{H}_I$, so that the overall Hamiltonian writes:

$$\hat{H} = \hat{H}_R + \hat{H}_I, \tag{1.20}$$

with, not considering for the moment the dependence on the variable μ:

$$\hat{H}_I = i\hbar\chi^{(2)} \left(\hat{a}^\dagger(\omega_1)\hat{a}^\dagger(\omega_2)\hat{b}(\omega_3) - H.c. \right), \tag{1.21}$$

where $\hat{b}$ is the annihilation operator for the pump beam and *H.c.* stands for *Hermitian conjugate*. In Equation (1.21) we have just formalized the down-conversion process: a pump photon annihilates generating two other photons satisfying the conservation of energy (and the opposite for the *H.c.*), all driven by the nonlinear susceptibility. If we now assume that the process is very inefficient, so that the pump beam is undepleted after the interaction, we can substitute the operator with its expectation value, which remains constant; this is the so-called *parametric approximation*. We can rewrite the interaction Hamiltonian as:

$$\hat{H}_I = i\hbar \left(\eta \hat{a}^\dagger(\omega_1)\hat{a}^\dagger(\omega_2) - H.c. \right) \tag{1.22}$$

where $\eta = \chi^{(2)}\beta$, with $\beta = \langle \hat{b} \rangle$. In the interaction picture [23], which allows to decouple the dynamics of the interaction term and of the free-radiation one, the state will evolve according to the operator

$$\hat{U}(t) = \exp\left(-i\frac{\hat{H}_I}{\hbar} t \right) = \exp\left(\eta \hat{a}^\dagger(\omega_1)\hat{a}^\dagger(\omega_2)t - H.c. \right). \tag{1.23}$$

[4]In general, if the mode l is populated by n photons, we will have: $\hat{N}_l|n_l\rangle = n_l|n_l\rangle$; this is the case for the so-called Fock states.

The state at time t will simply be $|\psi(t)\rangle = \hat{U}(t)|\psi(0)\rangle$; we now assume to have the vacuum state for $t = 0$, so that $|\psi(0)\rangle = |vac\rangle$. We further assume to be in low pumping regime, meaning $\eta t \ll 1$: this is the case if we want to limit multiple-pair emission processes. In this case, the exponential can be expanded into a power series:

$$|\psi(t)\rangle \simeq \left[1 + \left(\eta \hat{a}^\dagger(\omega_1)\hat{a}^\dagger(\omega_2)t - H.c.\right) + ...\right]|vac\rangle, \tag{1.24}$$

where the higher order terms correspond to multiple-pair emission. The second term of Equation (1.24) corresponds to the two-photon state we where searching for, while the first term is just the vacuum contribution and the $H.c.$ can be removed with post-selection. This state is still separable, since it can be rewritten as the tensor product of states of the two modes, $|\psi(t)\rangle \propto \hat{a}^\dagger(\omega_1)|vac\rangle \otimes \hat{a}^\dagger(\omega_2)|vac\rangle$; however, if we now consider the possibility that the two photons are emitted in two distinct modes of the electromagnetic field ($\mu \in u, v$), Equation (1.22) becomes:

$$\hat{H}_I = i\hbar\eta_1 \hat{a}_u^\dagger(\omega_1)\hat{a}_v^\dagger(\omega_2) + i\hbar\eta_2 \hat{a}_v^\dagger(\omega_1)\hat{a}_u^\dagger(\omega_2) + H.c. \tag{1.25}$$

As a consequence, the resulting state will now be:

$$|\psi(t)\rangle = \left(\eta_1 \hat{a}_u^\dagger(\omega_1)\hat{a}_v^\dagger(\omega_2) + \eta_2 \hat{a}_v^\dagger(\omega_1)\hat{a}_u^\dagger(\omega_2)\right) t|vac\rangle, \tag{1.26}$$

that is a non-separable – or, *entangled* – two-photon state.

In conclusion, SPDC, triggered by vacuum fluctuations, will occur efficiently in the medium only for those interactions with a non-null nonlinear susceptibility element and satisfying phase-matching relations, generating two-photon states.

1.2.2. Qubits and Bell's states

A quantum bit, or *qubit*, is a two-state quantum system representing the quantum analog to classical bits. In the most general form, it can be written as:

$$|\phi\rangle = \alpha|0\rangle + \beta|1\rangle, \tag{1.27}$$

where $|\alpha|^2 + |\beta|^2 = 1$. While a classical bit can be either 0 or 1, a qubit is in a coherent superposition of the two states, $|0\rangle$ and $|1\rangle$; when measured, it will give the value 0 with probability $|\alpha|^2$ and 1 with $|\beta|^2$. These two states are orthogonal and form a complete basis for the 2D-Hilbert space $\mathbb{H}$ occupied by the qubit.

Consider now two qubits, respectively in the Hilbert spaces $\mathbb{H}_A$ (with basis $|0\rangle_A, |1\rangle_A$) and $\mathbb{H}_B$ (with basis $|0\rangle_B, |1\rangle_B$). We can find separable or non-separable – in the sense explained in Section 1.2.1 – combinations of these qubits, spanning a 4D-Hilbert space $\mathbb{H}_{AB} = \mathbb{H}_A \otimes \mathbb{H}_B$; between all possible combinations, the so-called *Bell's states* are two-qubit entangled states that constitute a suitable (orthonormal, complete) basis for this new space:

$$|\Psi^{\pm}\rangle = \frac{1}{\sqrt{2}} \left(|0\rangle_A|1\rangle_B \pm |1\rangle_A|0\rangle_B\right), \tag{1.28a}$$

$$|\Phi^{\pm}\rangle = \frac{1}{\sqrt{2}} \left(|0\rangle_A|0\rangle_B \pm |1\rangle_A|1\rangle_B\right). \tag{1.28b}$$

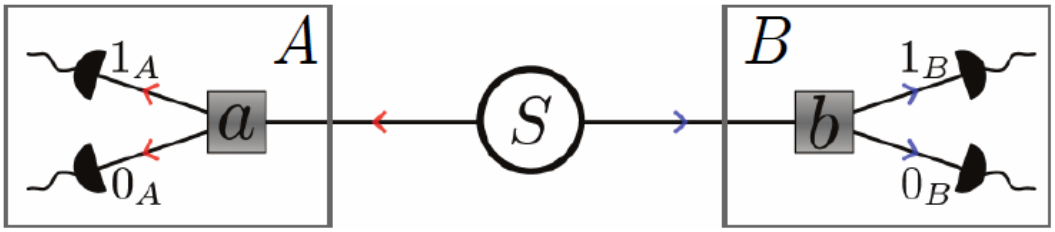

Figure 1.3: Setup for a Bell-type measurement. A source S produces pairs of correlated particles, and sends one to A and the other to B. They perform a measurement whose outcome is either 0 or 1. From [21].

It is now possible to better understand the meaning of entanglement. Consider a source that, as depicted in Figure 1.3, produces a pair of particles in a Bell's state (say, $|\Psi^+\rangle$) and sends one particle to the observer A and the other to the observer B. If the outcome of the measurement of A is $|0\rangle_A$[5], then it will instantaneously project the state of the particle received by B in $|1\rangle_B$, and viceversa, independently on the space-time separation of the two detection events.

This violation of the classical principle of locality can be demonstrated with the violation of the so-called Bell inequalities [24], and it has been done for the first time in 1981 by the team of A. Aspect [8], experimentally confirming the non-local character of quantum mechanics. Nowadays, entanglement is a fundamental resource in the field of quantum information, and the experimental violation of the Bell's inequalities has become a test bench to quantify the performances of the sources in the framework of the development of quantum technologies.

Note that quantum entangled systems can be produced in several ways, involving different

[5]The observer measures either 0 or 1, the eigenvalues related to the respective state, in which the superposition has collapsed after the measurement. This is why, even if a state cannot be directly measured, we can write as done above.

physical supports, hence presenting different properties. Some systems – such as cold ions [25] and atoms [26], superconductive systems [27] or color centers [28] – will be more suitable for quantum computation, where high interacting capability is required; when long distance distribution of entanglement becomes a key feature, as for quantum communication and cryptography, photonics shows relevant advantages with respect to other candidates: photons have high speed, they do not interact with each other and they are almost decoherence-free in free space or in optical fibers. This work is devoted to the development of integrated quantum photonic systems.

1.2.3. Polarization entanglement

Consider the case in which the particles used to encode the information are photons, and the discrete-valued variable μ introduced in Section 1.2.1 refers to two orthogonal polarization states, horizontal (H) and vertical (V). The state of a horizontally polarized photon can be written as $|H\rangle = \hat{a}_H^\dagger|vac\rangle$, while a vertical one $|V\rangle = \hat{a}_V^\dagger|vac\rangle$. Therefore, the generic polarization state of a single photon can be written as:

$$|\phi\rangle = \alpha|H\rangle + \beta|V\rangle, \tag{1.29}$$

with the same meaning of α and β as in Equation (1.27). We can then rewrite the Bell's state using polarization as degree of freedom:

$$|\Psi^\pm\rangle = \frac{1}{\sqrt{2}}\left(|H\rangle_A|V\rangle_B \pm |V\rangle_A|H\rangle_B\right), \tag{1.30a}$$

$$|\Phi^\pm\rangle = \frac{1}{\sqrt{2}}\left(|H\rangle_A|H\rangle_B \pm |V\rangle_A|V\rangle_B\right), \tag{1.30b}$$

which form a basis of entangled states for the 4D-Hilbert space occupied by the two-qubit photon states. For polarization Bell's states the measurement on the polarization of one photon (done, for example, with a polarized beam-splitter in combination with two single-photon detectors) will instantaneously project the state of the other one, according to the given superposition. Note that, as shown in Equation (1.26), this kind of entanglement can be produced through SPDC processes, as we will detail in the following.

1.2.4. Energy-time entanglement

The simultaneous emission of the photons of a pair by SPDC allows also to generate another type of entanglement: energy-time entanglement. In fact, if the pump beam (centred at ω_p) is narrowband, due to energy conservation ($\omega_1 + \omega_2 = \omega_p$) the two-photon

state will present strong frequency anti-correlation, leading to the following inequality:

$$\Delta(\omega_1 + \omega_2)\Delta(t_1 - t_2) < 1, \tag{1.31}$$

where Δ stands for the uncertainty on the knowledge of the pump frequency and the difference in arrival times at the detectors for the two photons. It can be demonstrated [29] that the opposite inequality holds for a separable state; therefore, if a two-photon state respects the inequality in (1.31), it will be, by definition, energy-time entangled. In Ref. [29], they where able to experimentally resolve the uncertainty on the arrival times, hence directly test the inequality.

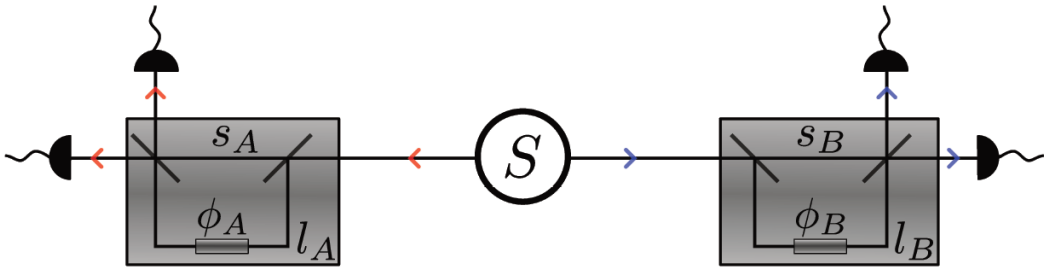

Figure 1.4: Setup for a Franson-type measurement. A source S produces pairs of correlated photons, and sends one to A and the other to B. Each particle enters an unbalanced interferometer, and it is then revealed with the use of single-photon detectors. From [21].

Energy-time entanglement can also be indirectly revealed through the so-called Franson interferometric setup, first used to demonstrate the violation of the classical locality principle exploiting a Bell's inequality for time and frequency [11]. As shown in Figure 1.4, a source S produces a pair of photons (for example, via SPDC), and sends one to the observer A and the other to B. Before being measured, each photon enters an unbalanced interferometer, made by two beam splitters (BS) connected by a long arm l and a short arm s; the difference between the two paths, ΔT, must be much larger than the coherence time of the photon, τ_c, in order to avoid single-photon interference [30]. In this way, only two-photon interference is revealed, at the additional condition that the pump coherence time, τ_p, is much larger than ΔT[6]. Furthermore, a tunable phase shifter is introduced, for example, in the long arms, inducing phase shifts of ϕ_A and ϕ_B. In this configuration, when travelling through the interferometers, each photon will either take l or s; considering the pair, four path combinations are possible: $s_A - l_B$, $l_A - s_B$, $s_A - s_B$ and $l_A - l_B$. Those combinations can be revealed by measuring the number of coincidences as a function of

[6] A detailed explanation on practical ways to experimentally implement this will be given in Section 3.4.1.

the difference in arrival times (Δt) of the two photons (see Section 1.3.3). Thus, three different peaks are expected: $\Delta t = -\Delta T$ for the first situation, $\Delta t = \Delta T$ for the second one and a third peak for $\Delta t = 0$, corresponding to the last two cases, as shown in Figure 1.5a.

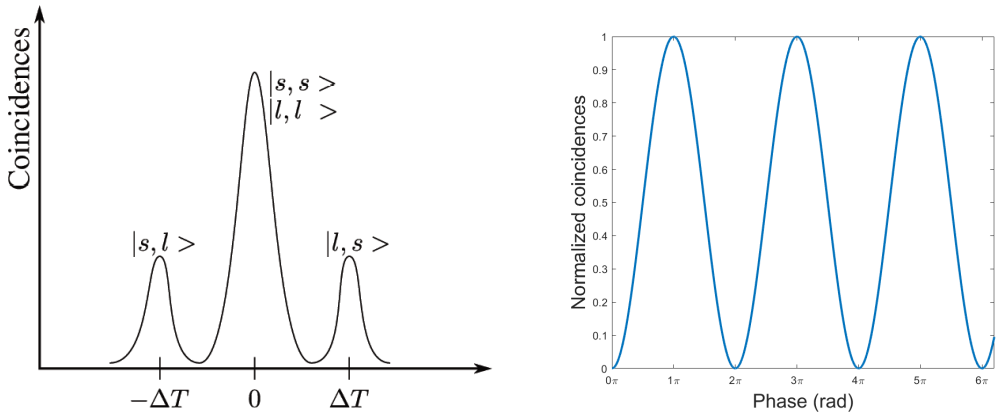

Figure 1.5: (a) Sketch of the possible result of the coincidences count for a Franson-type experiment: $|s,l\rangle = |s_A\rangle|l_B\rangle$, $|s,s\rangle = |s_A\rangle|s_B\rangle$, $|l,l\rangle = |l_A\rangle|l_B\rangle$ and $|l,s\rangle = |l_A\rangle|s_B\rangle$. (b) Ideal interference profile for the central peak, as a function of the relative phase ϕ between the two long arms of the interferometers.

The two biphoton states falling in the central peak, $|s_A\rangle|s_B\rangle$ and $|l_A\rangle|l_B\rangle$, are, at the conditions imposed so far, indistinguishable, hence giving quantum interference. The interference profile will be governed by the relative phase, $\phi = \phi_A - \phi_B$, acquired by each photon when travelling through the long arm of its interferometer, as shown in Figure 1.5b in the ideal case of two perfectly entangled photons. By post-selecting the photons in the central peak, we obtain the following entangled two-photon state:

$$|\psi_{A,B}\rangle = \frac{1}{\sqrt{2}}\left(|s_A\rangle|s_B\rangle + e^{i\phi}|l_A\rangle|l_B\rangle\right). \tag{1.32}$$

The visibility of the interference fringes is a figure of merit for the level of entanglement of the generated state. It can be demonstrated [31, 32] that for a separable state it cannot exceed 50%; any measurement exceeding this threshold is an indirect and sufficient demonstration of energy-time entanglement.

1.3. Photon-pair sources: an overview

In this section, a general overview about nonlinear integrated photon-pair sources is given, based on Ref. [33]. In particular, we discuss the main material platforms, enlightening the most relevant properties, and the figures of merit used to characterize and evaluate their performances and the produced quantum state.

1.3.1. Nonlinear integrated photon-pair sources

Nonlinear photon-pair sources are based on nonlinear optical processes, as described in Section 1.1: most of them exploit – included the ones used in this work – either second-order nonlinearity, generating pairs by SPDC (Section 1.2.1), or third-order interactions, generating pairs by Spontaneous Four-Wave Mixing (SFWM). The two processes are illustrated in Figures 1.6a and 1.6b. Those processes are typically carried into waveguides, physical structures that guide electromagnetic radiation, as shown in Figure 1.6c, or ring resonators, in Figure 1.6d. This is a common characteristic for all the material platforms in the attempt of achieving efficient integration.

A waveguide confines light in the two transverse directions, while letting it propagate in the longitudinal one. The waves are confined in the so-called *core* of the structure, and the confinement can be obtained with total reflection at the *cladding* surrounding it, or with periodical cladding used as reflectors, as will be detailed in Section 2.2.1. The phenomenon of total internal reflection occurs when the refractive index of the core, n_{core}, is larger than the one of the cladding, n_{clad}. In the simplified vision of geometric optics, we can imagine that a critical angle for the propagation exists, meaning that light entering the structure with a larger angle cannot be transmitted through the cladding, but it will be continuously reflected up to the end of the guide. The cladding can be another material with a lower refractive index than the one in the core, or the air itself, in the case of ridge waveguides.

A solution of the wave equations in the waveguide is a propagation *mode*: only for a discrete set of frequencies and shapes for the wave function it is possible to have constructive interference out of the multi-reflections at the core/cladding interfaces. According to the frequency, each mode has a different effective refractive index, n_{eff}, such that $n_{core} > n_{eff} > n_{clad}$.

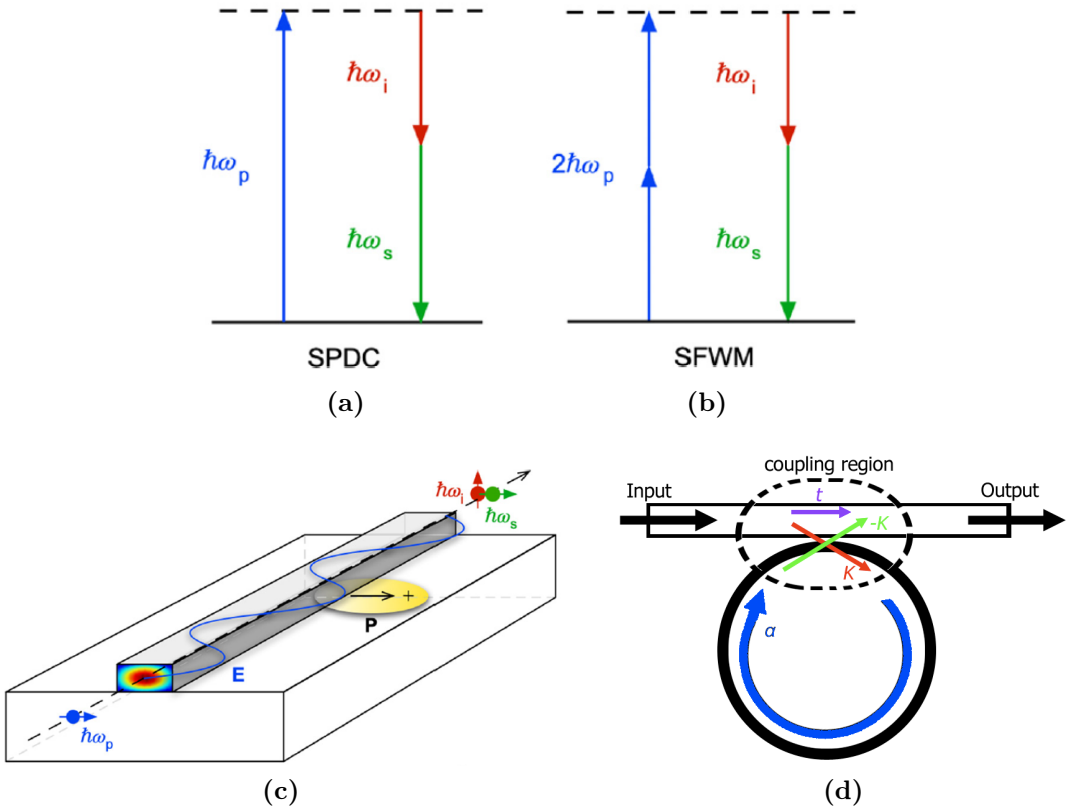

Figure 1.6: Fundamentals of photon-pairs generation. Scheme of (a) SPDC and (b) SFWM processes.(c) Sketch of a ridge waveguide with electromagnetic field mode propagation and (d) of a ring resonator. (a), (b) and (c) taken from Ref. [33], (d) from https://commons.wikimedia.org/w/index.php?curid=17670439.

1.3.2. Main material platforms

Material platforms for photon-pair sources are chosen according to their linear and nonlinear properties, such as the strength of the nonlinear tensor ($\chi^{(2)}$ and $\chi^{(3)}$, see Section 1.1.4), optical losses at the desired wavelength, availability of pump sources and maturity of manufacturing processes. In addition, in the field of quantum communication, a critical requirement will be the compatibility with the existent telecom infrastructure, meaning that the best performances must be achieved and the photons produced in the appropriate bands (in particular, the C-L band: $1530 - 1625nm$). Considering all these constraints, we list here the most employed and efficient platforms employed in current research:

Silicon. Platforms made of silicon, especially silicon-on-insulator (SOI), are probably the leaders in linear integrated photonics, thanks to the advanced process maturity that makes them suitable for the realization of crucial integrated components, such as modulators, couplers or multiplexers. They are typically transparent in

the range $1.1 - 2\mu m$, but they lack of intrinsic $\chi^{(2)}$ nonlinearity, being silicon a centro-symmetric crystal [20]. However, it shows quite strong third-order nonlinearity, suitable for pairs production with SFWM. Silicon nitride (SiN, Si_3N_4) based platforms are also an alternative, showing comparable overall performances in pairs production: while SOI has stronger nonlinearity, silicon nitride shows lower losses.

III-V semiconductors. Semiconductors formed by elements of the III group (B, Al, Ga, In) and the V one (N, P, As, Sb) can show very relevant nonlinear properties. The most used platforms are GaAs and related compounds: this material is transparent in the range $0.8 - 10\mu m$, has one of the highest $\chi^{(2)}$ values and a strong $\chi^{(3)}$, making it suitable for pair production with either SPDC and SFWM. It can also be used for the realization of relevant integrated components and electrically-pumped sources [34]. Furthermore, AlGaAs-on-insulator (AlGaAs-OI) is emerging as a new promising platform, matching the nonlinear properties of AlGaAs with the characteristics of, for example, SOI; efficient SHG and photon-pair production have already been demonstrated [35, 36].

Lithium niobate. Ultra-low-loss waveguides can be realized out of lithium niobate (LN) for the range $0.5 - 4\mu m$. This material show both second and third order nonlinear responses, and intrinsic ferroelectricity, so that it can be periodically poled (PPLN) to meet phase-matching requirements (see Section 2.1.2). It is also particularly suitable for the realization of integrated components or for chip-scale integration with insulator, III-V and glass platforms [37–39].

Glasses. Optical fibers, the backbone of the telecom infrastructure, are realized with fused silica glass, which shows exceptional transparency but essentially null nonlinearity. However, they can be engineer in terms of geometry and poling, enabling pairs production; tools exploiting these platforms are already commercialized [40]. Other glasses, such as chalcogenide glasses, are characterized by high third-order nonlinearity and transparence, allowing pairs production via SFWM, especially in the mid-IR region.

1.3.3. Figures of merit: performances

In this section, we list a series of parameters commonly used to quantitatively characterize the performances of photon-pair sources; we will refer to them in the following of this work to evaluate the results of the proposed devices.

First of all, it is useful to formally introduce what we mean with *coincidence* and *coincidence rate*. Assume that, in a given time interval ΔT, a photon-pair source S produces

r pairs, that are collected with a collection efficiency of η_c; assume, in addition, that we can (arbitrarily) separate the two photons[7], so that one is the so-called *signal* and the other the *idler*. We can now detect each photon with a single photon detector (SPD), with efficiency η_d, and measure the difference in arrival time (Δt) between the two with a time-correlated single photon counting (TCSPC) module. The finite resolution of this module, δt, discretizes the time axis in *time bins*. Per each time bin, we can count the number of detected photon pairs arrived with that precise delay: this constitutes the number of coincidences for that bin. Since the two photons are produced instantaneously (see Section 1.2.1), the difference in arrival time will be constant, given by the measurement setup: the bin(s) collecting those coincidences can be assumed to correspond to $\Delta t = 0$, and the coincidences counted there will be our experimental result. In Figure 1.9 we can see the sketch of the setup used for this kind of measurements (1.7a) and the resulting histogram of the counted coincidences per time bin (1.7b).

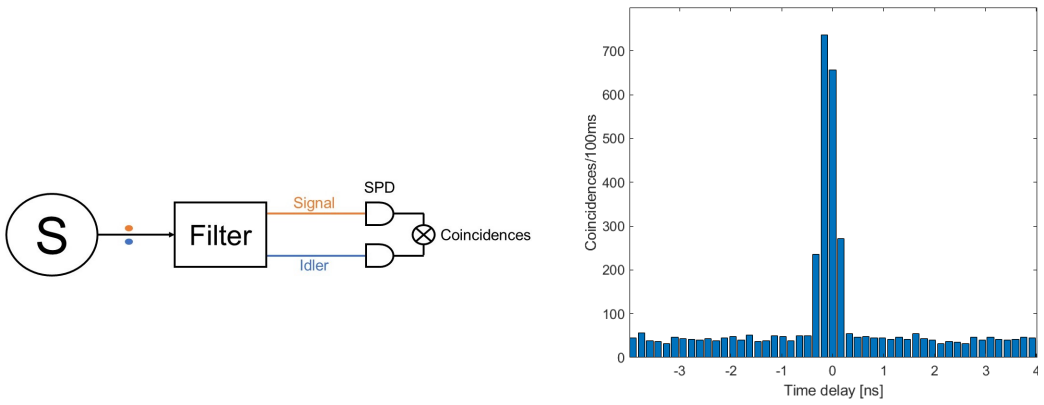

(a) **(b)**

Figure 1.7: (a) Sketch of the setup for coincidences measurement. S: source, SPD: single-photon detector. (b) Recorded histogram of coincidences: each column corresponds to a time bin.

The counted coincidences c are related to the actual number of generated pairs through:

$$c = \eta_c \eta_d r. \tag{1.33}$$

If we divide each term by the integration time ΔT, we obtain the respective measured

[7]For example, if we have a cross-polarized biphoton state, as the ones described in Section 1.2.3, we can separate in a deterministic way the two particles with the use of a polarizing beam splitter (PBS).

coincidence (C) and *generation* (R, PGR) rates:

$$C = \eta_c \eta_d R. \tag{1.34}$$

We can then define the *brightness* B of a source as the PGR per unit pump power P_p and spectral bandwidth $\Delta\lambda$:

$$B = \frac{R}{P_p \Delta\lambda}, \tag{1.35}$$

which is typically expressed in $\mathrm{s}^{-1}{\cdot}\mathrm{mW}^{-1}{\cdot}\mathrm{nm}^{-1}$. To be more precise, we should include the possibility of accidental counts, A, coming from detector dark counts and noise produced in the generation process, and the fact that the efficiencies have to be referred separately to each photon of the pair, so that:

$$\begin{aligned} C_{raw} &= (\eta_{c,s}\eta_{d,s})(\eta_{c,i}\eta_{d,i})R + A \\ &= \eta_s \eta_i R + A \\ &= C_{net} + A, \end{aligned} \tag{1.36}$$

where s and i refer to signal and idler, and we have multiplied the different efficiencies assuming the collection and detection events of each photon of the pair (η_s, η_i) as independent. The measured (*raw*) number of coincidences is, hence, the *net* value plus the contribution of the accidental counts.

Therefore, the signal-to-noise ratio (SNR) for such sources can be expressed as coincidence-to-accidental ratio (CAR):

$$CAR = \frac{C_{net}}{A}. \tag{1.37}$$

It can be demonstrated [33] that, being D the detector dark count rate, for low pump power regimes ($\eta R \ll D$, with $\eta_s \simeq \eta_i = \eta$) we have $CAR \sim \eta^2 R/D^2$, while for high pump power regimes $CAR \sim 1/R$. Thus, there is an optimal value for the pump power, for which the maximum CAR is reached.

1.3.4. Figures of merit: quantum state

The produced quantum state is also quantitatively evaluated with the use of proper parameters.

Through the *second-order correlation function*, $g^{(2)}(\tau)$, the degree of photon anti-bunching can be characterized for each photon of the pair. This is done with the Hanbury Brown-Twiss (HBT) experiment [41], whose setup is shown in Figure 1.8a: note the the measure-

ment is performed on one photon of the pair only, while the other is used for heralding. $g^{(2)}(\tau)$ is defined as:

$$g^{(2)}(\tau) = \frac{\langle I(t)I(t+\tau)\rangle}{\langle I(t)\rangle\langle I(t+\tau)\rangle}, \tag{1.38}$$

where $I(t)$ is the field intensity measured by the detector, and angle brackets are a time average over a period much longer than τ. If photons are in a Fock state $|n\rangle$ (see Section 1.2.1), the intensity is simply the number of photons n, and Equation 1.38, evaluated in $\tau = 0$ becomes:

$$g^{(2)}(0) = 1 - \frac{1}{n}, \tag{1.39}$$

which is zero for the case of single-photon state, $|n\rangle = |1\rangle$. The more $g^{(2)}(0)$ approaches zero, the more the source is capable to produce heralded single photons.

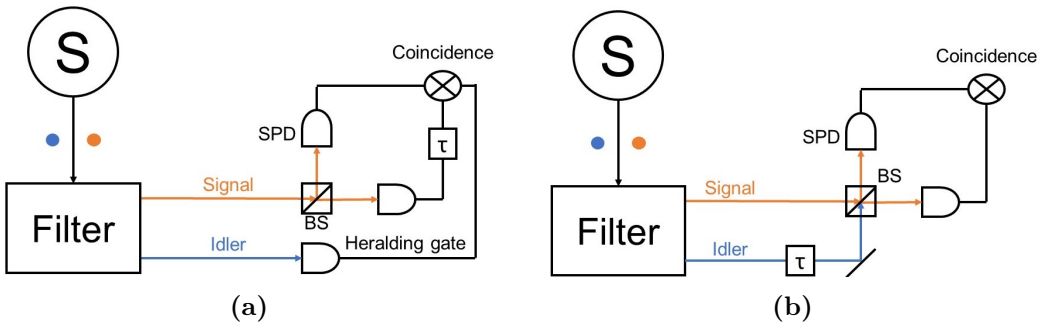

Figure 1.8: Sketches of the setup for the (a) HBT and (b) HOM experiments. S: source, SPD: single-photon detector, BS: beam splitter, τ: delay line.

The *indistinguishability* of the two photons can also be evaluated, thanks to the Hong-Ou-Mandel (HOM) interferometry [42] (setup in Figure 1.8b). When the two photons enter the beam splitter, four different outcomes are possible, as shown in Figure 1.9a: if the photons are distinguishable, all the possibility are equally probable and the overall probability of coincidences is 50%; if they are perfectly indistinguishable, the first two possibilities destructively interfere[8], and the overall probability of coincidences is 0. By tuning the controllable delay τ, we retrieve the so-called HOM dip (Figure 1.9b), whose visibility characterizes the level of indistinguishability. The width is given by the temporal overlap of the two photons, whose coherence time we assume to be δt.

For what concerns the evaluation of the entanglement quality, a detailed discussion can be found in Sections 1.2.3 and 1.2.4.

[8]The two events are, as well, perfectly indistinguishable, but with an opposite phase introduced by the beam splitter.

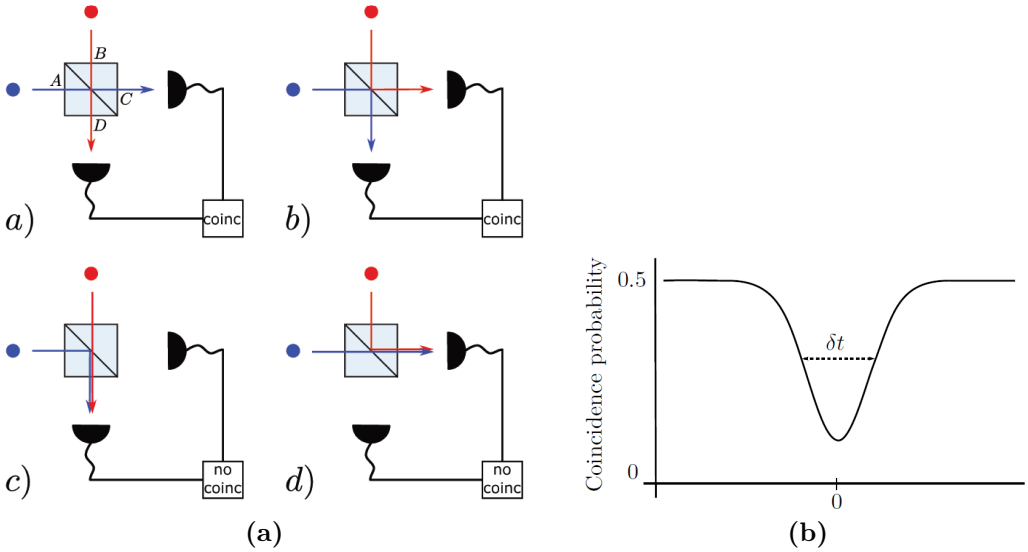

Figure 1.9: (a) The possible outcomes when two photons impinge on a 50/50 BS. (b) HOM interference profile with the typical HOM dip, which gives the degree of indistinguishability. From [21].

2 | AlGaAs waveguides as photon-pair sources

This chapter is devoted to the detailed description of the AlGaAs-based photon-pair sources, from design to fabrication. For this purpose, the theoretical concepts introduced in Chapter 1 are here developed and discussed in the specific case of waveguides, especially for what concerns three-wave mixing, phase-matching conditions and SPDC processes.

2.1. Nonlinear optics in waveguides

In Section 1.3.1, we introduced the ridge waveguide structure for guiding electromagnetic field thanks to total internal reflection, and the concept of propagation mode. With reference to the coordinate system in Figure 2.1, we define the propagation direction as the axis y, and the transverse directions as x and z. The field of a mode can be decomposed, in the transverse plane, with respect to the vertical and to the horizontal axis, as underlined in the same figure: a mode will be *transverse magnetic* (TM) if its electric field has only the vertical component, *transverse electric* (TE) if only the horizontal; in other words, the mode will be either TM- or TE-polarized. This specification is essential for proceeding with the next steps.

In this work, the modes profiles and the respective effective indices in a given waveguide are numerically calculated with finite difference methods through the use of Lumerical, a commercial electromagnetic simulation software; in fact, analytical solutions to the wave equation are only available for elementary geometries.

2.1.1. Wave mixing efficiency

In waveguides, not only the light is guided, but, according to the material and its design, nonlinear processes can be triggered: the field of nonlinear integrated photonics is very active in this sense. The fields, confined in the guide, are colinear, in the sense that they share the same propagation direction: this is clearly an advantage for non-point

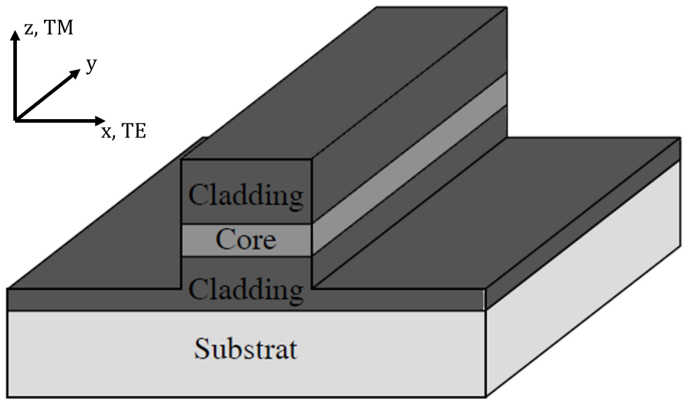

Figure 2.1: Sketch of a ridge waveguide structure with the reference frame and the TE and TM directions underlined.

interactions. However, when considering a frequency conversion process – for example, the usual SFG: $\omega_1 + \omega_2 \rightarrow \omega_3$ –, we need to modify the expression derived in (1.13) in order to include the characteristics of the guided modes. In particular, the strength of the interaction strongly depends on the overlap between the involved modes in the transverse directions. Hence, we can define the *nonlinear overlap* as:

$$\Gamma = \frac{\iint_S \mathrm{d}x\mathrm{d}z d_{eff}(x,z) A_1^*(x,z) A_2^*(x,z) A_3(x,z)}{\left[\iint_S \mathrm{d}x\mathrm{d}z |A_1(x,z)|^2\right]^{\frac{1}{2}} \left[\iint_S \mathrm{d}x\mathrm{d}z |A_2(x,z)|^2\right]^{\frac{1}{2}} \left[\iint_S \mathrm{d}x\mathrm{d}z |A_3(x,z)|^2\right]^{\frac{1}{2}}}, \tag{2.1}$$

where the integrals are carried over the waveguide transverse section S, the denominator is the normalization factor for the fields and we have assumed y to be the propagation direction. Note that we have also included in the integral the effective susceptibility, accounting for the possibility that it can vary within the transverse section, as it is usually the case due to the multi-layer epitaxial structure. Equation (1.13) becomes then:

$$P_3 = 2\frac{\omega_3^2}{n_1^{eff} n_2^{eff} n_3^{eff} \epsilon_0 c^3} L^2 |\Gamma|^2 P_1 P_2 \mathrm{sinc}^2\left(\frac{\Delta k L}{2}\right), \tag{2.2}$$

where $P_i = \int \int_S I_i dx dz$ is the time-averaged optical power and n_i^{eff} is the effective refractive index of the core for the mode i. Therefore, the *conversion efficiency*, defined as optical power of the generated field divided by the optical power of the pump fields, will be:

$$\eta_{SFG} = \frac{P_3}{P_1 P_2} = \eta_{SFG}^0 L^2 \mathrm{sinc}^2\left(\frac{\Delta k L}{2}\right), \tag{2.3}$$

where

$$\eta_{SFG}^0 = 2\frac{\omega_3^2}{n_1^{eff} n_2^{eff} n_3^{eff} \epsilon_0 c^3} |\Gamma|^2 \tag{2.4}$$

is the *normalized* conversion efficiency, typically given in $\%W^{-1}cm^{-2}$. The same formula can be applied in the case of SHG and DFG processes.

The conversion efficiency is a critical parameter for waveguides, that must be taken into account for a proper design; as it can be seen from Equations (2.3) and (2.4), it mainly depends on the nonlinear overlap, Γ, related to the nonlinear properties of the chosen material and to the waveguide geometry, and on the phase mismatch Δk, which should be the closest possible to zero to provide maximum efficiency (phase-matching condition). The squared dependence on the waveguide length L is limited by a trade-off with the transmitted optical intensity, which decreases exponentially with the same parameter.

As a last remark, it can be demonstrated [43] that η_{SFG} is proportional to the SPDC conversion efficiency, η_{SPDC}:

$$\eta_{SPDC} = \eta_{SFG}\hbar\frac{\omega_1\omega_2}{\omega_3}\frac{\Delta\omega}{2\pi}, \tag{2.5}$$

where $\Delta\omega$ is the spectral bandwidth of the emitted state, given by the phase-matching condition. This relation can intuitively be understood considering that SFG and SPDC are reverse processes.

2.1.2. Phase-matching methods

Phase-matching is a crucial condition to obtain an efficient frequency conversion. Considering a process between three waves (at frequencies ω_1, ω_2 and ω_3), which satisfies the requirement of energy conservation for $\omega_3 = \omega_1 + \omega_2$, the phase-matching condition writes:

$$\mathbf{k_3} = \mathbf{k_1} + \mathbf{k_2}, \tag{2.6}$$

with $n_i = n(\omega_i)\omega_i/c$ for dispersive materials, meaning that the refractive index is a function of the frequency. In the case of colinear fields, the latter equation can be rewritten as:

$$n(\omega_3)\omega_3 = n(\omega_1)\omega_1 + n(\omega_2)\omega_2. \tag{2.7}$$

Being $n(\omega)$ a monotonic increasing function in the spectral region of interest (see Figure 2.2a for typical profiles[1] of the modal refractive index in an AlGaAs structure), it is straightforward to see that such a condition is in principle impossible to meet; for instance, if we consider a SHG process ($\omega_1 = \omega_2 = \omega$ and $\omega_3 = 2\omega$), Equation (2.7) turns into $n(2\omega) = n(\omega)$, which is clearly in contrast with the function profile.

[1] This is the so-called *dispersion* or *chromatic dispersion* curve.

Several strategies are, thus, implemented to practically overcome this issue and meet the phase-matching condition:

Birefringence. If the refractive index of a dielectric material depends on the polarization of the field propagating, the material is said to be birefringent. Phase-matching can be achieved if, given two different modes with two different polarization directions u and v, $n_u(2\omega) = n_v(\omega)$. In AlGaAs, the intrinsic birefringence is not enough to satisfy this condition; a solution can be to induce artificial birefringence (or *form birefringence*) by introducing layers of aluminium oxyde (AlOx) [44, 45]. This, however, introduces roughness and optical losses, detrimental to quantum optical applications.

Quasi-phase-matching (QPM). Periodic modulation of the nonlinear coefficient enables to obtain an increase of conversion efficiency along the propagation length. In fact, if the sign of $\chi^{(2)}$ is reversed with a period of length $\pi/|\Delta k|$, the oscillation shown in Figure 1.2 will ramp up from its maximum at each interface, producing the profile in Figure 2.2b. In practice, the material is divided into regions of the given length along the propagation direction: the result is a constructive interaction between the fields, even though there is still a non-null wave-vector mismatch. This method is extensively implemented, for example, in PPLN, PPKTP and PPGaAs crystals and waveguides [46–48].

Counter-propagating phase-matching. The practical scheme for the implementation of this technique is displayed in Figure 2.2c: the pump beam (at ω_3) impinges on the top of the waveguide with a given angle θ, and the two produced fields will propagate in opposite directions. In the longitudinal direction, phase-matching is achieved by tuning the angle θ, so that $\omega_3 \sin\theta = \omega_1 n(\omega_1) - \omega_2 n(\omega_2)$; in the transverse direction, by alternating AlGaAs layers of different concentrations[2], to implement a QPM scheme such that $k_3 \cos\theta = k_{QPM}$ (see Figure 2.2d). This method was demonstrated in [49].

Modal phase-matching. In multimode waveguides, we can have guided modes with different chromatic dispersion. According to the design of the structure, this principle can be exploited to obtain guided modes compatible with the perfect phase-matching condition. In particular, considering an SHG process, if u denotes the mode at higher frequency and v the one at lower frequency, the waveguide should be engineered in order to achieve $n_u(2\omega) = n_v(\omega)$, as shown in Figure 2.2a for one

[2]The concentration of aluminium has a direct and controllable impact on the value of the effective nonlinear susceptibility, as will be detailed in Section 2.2.1.

of our structures. In fact, this is the method used in the presented work, and the design details will be described in the following.

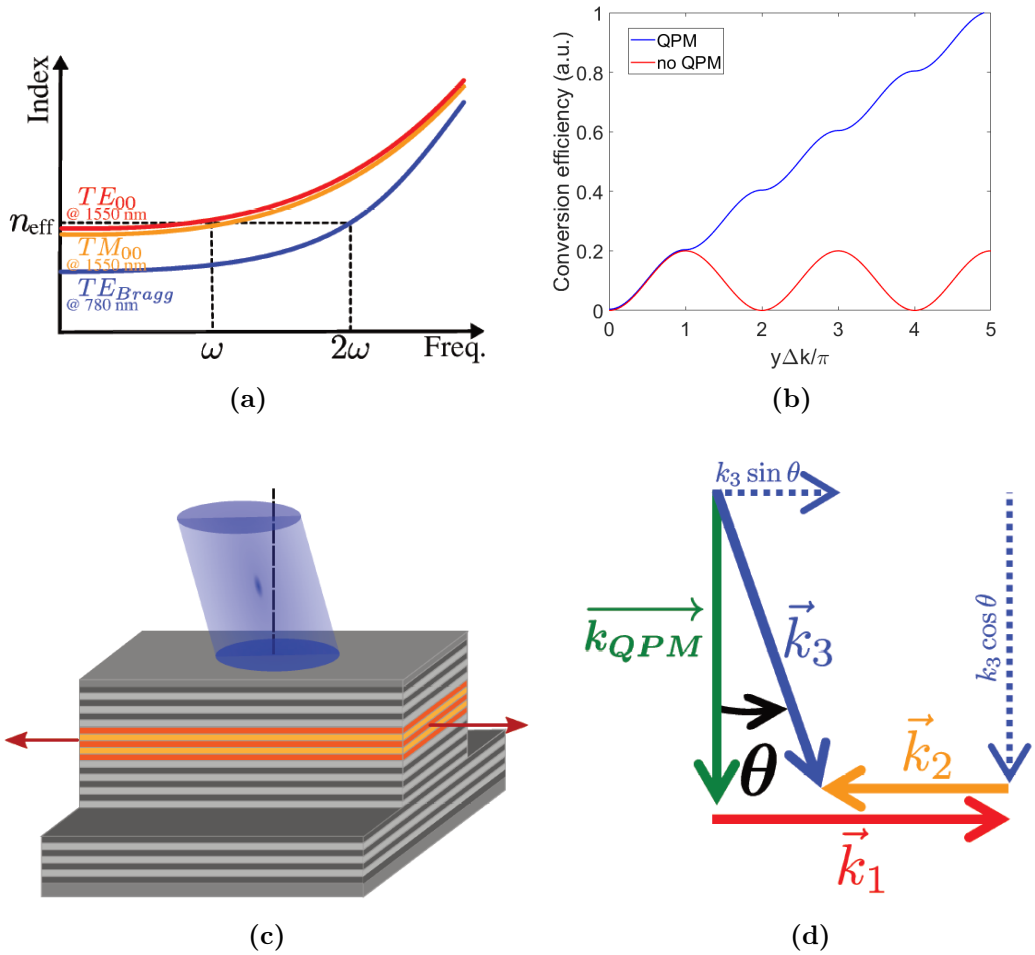

Figure 2.2: (a) Typical dispersion curves in AlGaAs structures, and example of modal phase-matching strategy. (b) QPM profile for the conversion efficiency, compared to the efficiency profile in case of phase-mismatch. (c) Sketch for the counter-propagating phase-matching scheme, with (d) detailed vectorial sum. (a), (c) and (d) from [21].

2.1.3. Nonlinear tensor in AlGaAs

As stated in conclusion of section 1.1.4, the nonlinear tensor, reduced to the effective susceptibility matrix, determines which parametric processes are allowed in a given structure. We consider now the specific case of GaAs (and AlGaAs: they are equivalent from the point of view of symmetry properties): its crystal unit cell, displayed in Figure 2.3a, belongs to the $\bar{4}3m$ symmetry group. This leads to only three (equivalent) non-zero elements in the susceptibility matrix [50], that will appear, in the basis of the GaAs crystallographic

axes – $x' = [100]$, $y' = [010]$, $z' = [001]$ –, as:

$$d = \begin{pmatrix} 0 & 0 & 0 & d_{14} & 0 & 0 \\ 0 & 0 & 0 & 0 & d_{14} & 0 \\ 0 & 0 & 0 & 0 & 0 & d_{14} \end{pmatrix}. \tag{2.8}$$

By plugging this matrix in the Equation (1.14) of the nonlinear polarization generated by SFG ($\omega_3 = \omega_1 + \omega_2$), we get:

$$\begin{pmatrix} P^{NL}_{3,x'} \\ P^{NL}_{3,y'} \\ P^{NL}_{3,z'} \end{pmatrix} = 2\epsilon_0 d_{14} \begin{pmatrix} E_{1,y'}E_{2,z'} + E_{1,z'}E_{2,y'} \\ E_{1,x'}E_{2,z'} + E_{1,z'}E_{2,x'} \\ E_{1,x'}E_{2,y'} + E_{1,y'}E_{2,x'} \end{pmatrix}, \tag{2.9}$$

where the subscripts 1, 2 and 3 stand for the respective frequencies. We can now apply the rotation matrix in order to rotate the $x'y'$ axes counterclockwise by an angle of $\pi/4$ around the z' (z) axis[3], and so be coherent with the reference system of the waveguide ($x = [\bar{1}10]$, $y = [1\bar{1}0]$, $z = [001]$ – it will soon be clear why we choose these crystallographic axes for our structure), obtaining:

$$\begin{pmatrix} P^{NL}_{3,x} \\ P^{NL}_{3,y} \\ P^{NL}_{3,z} \end{pmatrix} = 2\epsilon_0 d_{14} \begin{pmatrix} E_{1,z}E_{2,x} + E_{1,x}E_{2,z} \\ -E_{1,z}E_{2,y} - E_{1,y}E_{2,z} \\ E_{1,x}E_{2,x} - E_{1,y}E_{2,y} \end{pmatrix}. \tag{2.10}$$

If we now consider that the pump mode(s) can be either TE or TM[4], three processes are allowed according to Equation (2.10):

1. **Type II**: TE+TM↔TE $\Rightarrow P^{NL}_{3,x} = E_{1,z}E_{2,x} + E_{1,x}E_{2,z}$;
2. **Type I**: TE+TE↔TM $\Rightarrow P^{NL}_{3,z} = E_{1,x}E_{2,x}$;
3. **Type 0**: TM+TM↔TM $\Rightarrow P^{NL}_{3,z} = -E_{1,y}E_{2,y}$ and $P^{NL}_{3,y} = -E_{1,z}E_{2,y} - E_{1,y}E_{2,z}$.

Note that for Type 0 we consider different components of the field: in fact, it is accessible thanks to non-null components of the TM mode along the field propagation direction y [51]. In general, for a given process type, the nonlinear overlap is calculated as in Equation (2.1), by taking into account all the components of the involved modes, as done in [52].

[3]The matrix in question is:

$$R_z(-\pi/4) = \frac{1}{\sqrt{2}} \begin{pmatrix} 1 & 1 & 0 \\ -1 & 1 & 0 \\ 0 & 0 & 1 \end{pmatrix}.$$

[4]For a TE mode, E_x is non-null and $E_z = 0$; for TM the opposite. The value of E_y depends on the physical confinement within the waveguide.

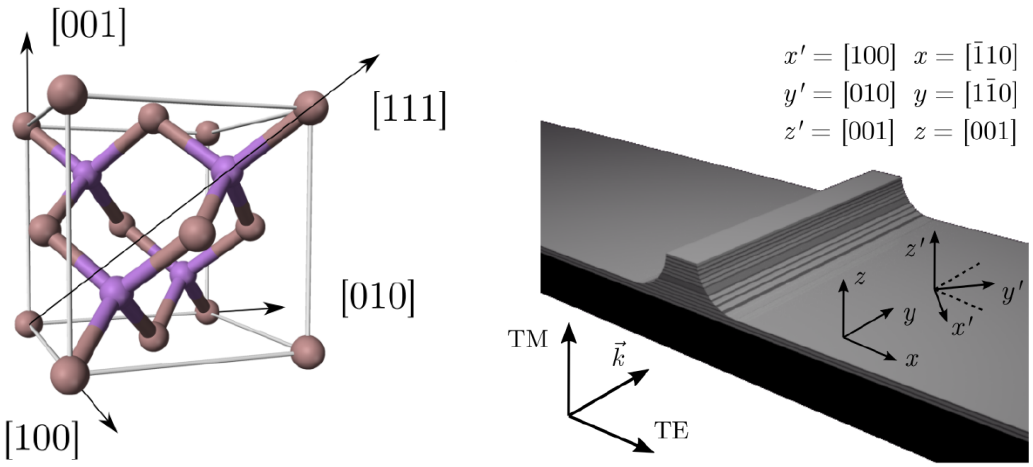

(a) (b)

Figure 2.3: (a) GaAs crystal unit cell and principal crystallographic directions. (b) Waveguide structure with specified crystallographic axes. From [53].

2.2. Design and fabrication

We introduce in this section the working principles of the Bragg reflector waveguide, with focus on the implementation in AlGaAs structures. The consequent design choices regarding the relevant parameters are then presented and motivated. Finally, the fabrication processes leading to the realization of the waveguides are described.

2.2.1. Bragg reflector waveguides

AlGaAs is obtained by replacing a percentage x (with $x \in (0, 1)$) of gallium species with aluminium atoms: the resulting alloy can be written in the form $Al_xGa_{1-x}As$, in order to specify the relative concentration of Al. By tuning this concentration, the refractive index can be engineered, as shown in Figure 2.4a, which is based on the Gehrsitz model [54]. When the concentration of Al increases, the refractive index decreases; being 80% the maximum allowed concentration of Al in our devices[5], the range of variation for the index in the telecom band ($\lambda \sim 1550nm$) is [2.9, 3.3]. Furthermore, the concentration of Al has a direct impact on the value of the second-order nonlinear susceptibility, that is reduced with respect to the one of GaAs, as shown in Figure 2.4b following the model of Ohashi [55].

A Bragg reflector waveguide, first introduced by Yeh and Yariv [57] and recently re-

[5]A fast oxidation process of the material would occur at higher aluminium concentrations, causing the degradation of its optical properties.

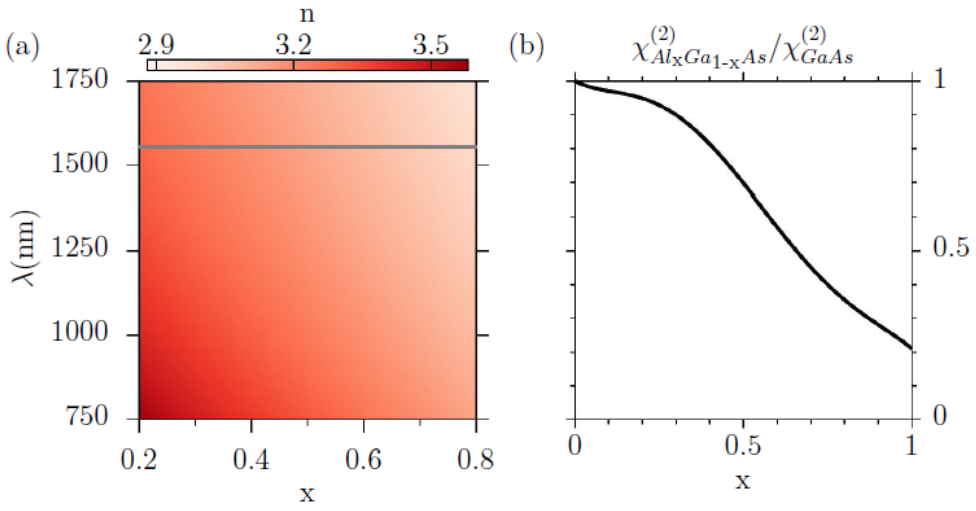

Figure 2.4: (a) $Al_xGa_{1-x}As$ refractive index as a function of Al relative concentration and wavelength; the grey line corresponds to $\lambda = 1550nm$. (b) Normalized $Al_xGa_{1-x}As$ second-order nonlinear susceptibility versus Al concentration. From [56].

investigated in [58], is a ridge waveguide consisting of a core sandwiched between two distributed Bragg reflectors along the vertical direction, as already shown in Figure 2.3b. Bragg reflectors (or mirrors) are realized in AlGaAs by alternating layers with either low or high concentration of Al and, thus, with respectively high (n_H) or low (n_L) refractive index. By selecting the proper composition and thickness of the layers ($t_H = \lambda/(4n_H)$ and $t_L = \lambda/(4n_L)$, where $t_H(t_L)$ is the thickness of the high(low) index layer and λ the mode wavelength), constructive interference occurs and the mode, which is therefore called "Bragg mode", is supported by the waveguide. In particular, our waveguide is designed to guide by total internal reflection (see Section 1.3.1) the TE and TM fundamental Gaussian modes at telecom wavelength ($\lambda \sim 1550nm$), and the TE and TM Bragg modes at double the frequency ($\lambda \sim 775nm$); the shape of these modes, obtained with a commercial 2D eigenmode solver (Lumerical MODE), is shown in Figure 2.5, together with the refractive index (at $\lambda = 1550nm$) and the second-order nonlinear coefficient profiles.

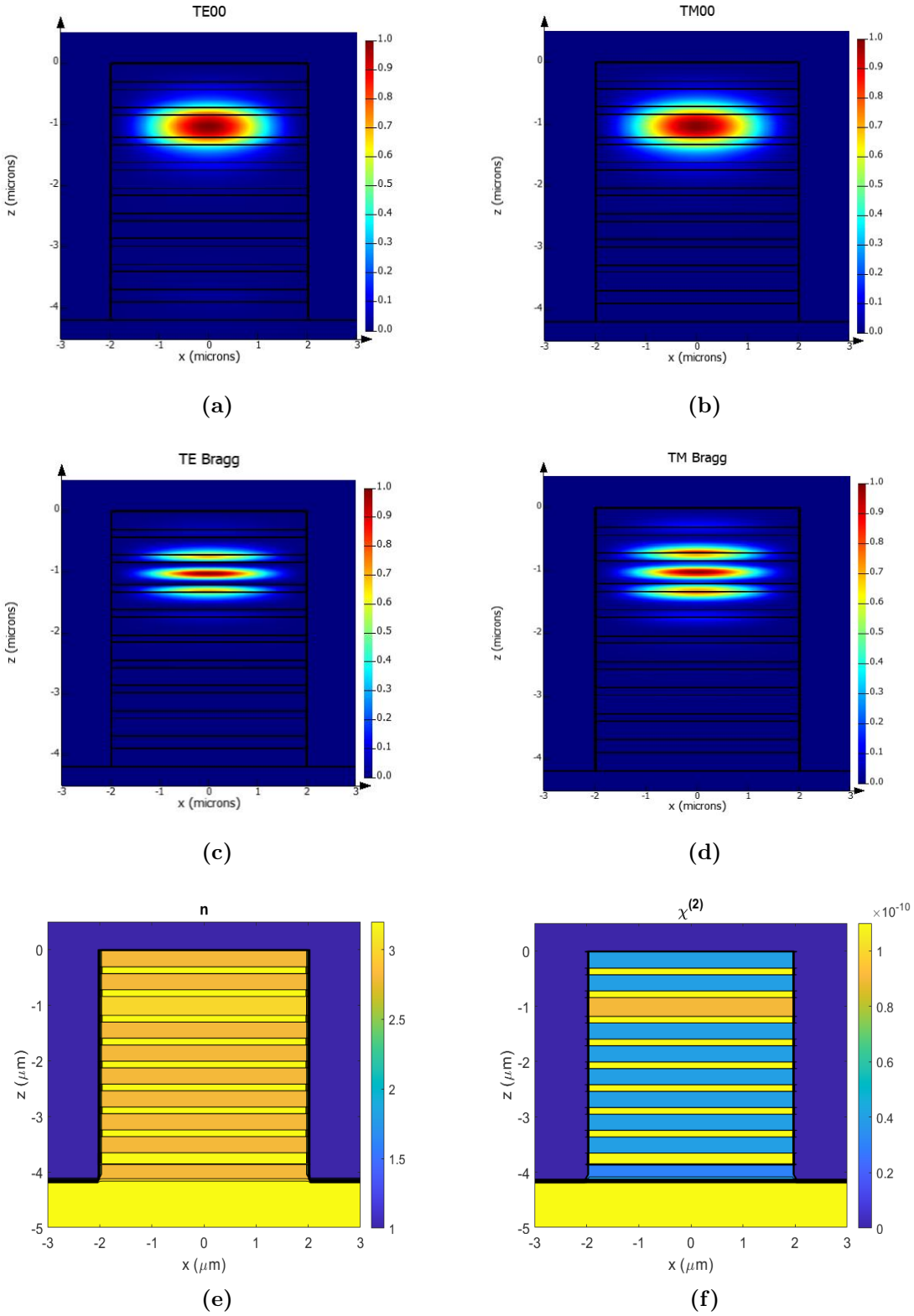

Figure 2.5: Electric field normalised intensity of the modes supported by the Bragg reflector waveguide: fundamental TE (a) and TM (b) modes at 1550nm, Bragg TE (c) and TM (d) modes at 775nm. Profile of (e) the refractive index (at $\lambda = 1550nm$) and (f) the second-order nonlinear susceptibility (in m/V).

The first design was conceived by A. Orieux [43]: the waveguide was composed by six Bragg mirrors ($x_L = 80\%$ with $t_L = 276nm$ and $x_H = 25\%$ with $t_H = 114nm$, where $x_H(x_L)$ is the Al concentration of the high(low) refractive index layer) per each side, a core of thickness 298nm and Al concentration 45% and a GaAs cap (thickness 250nm) and substrate. The devices used in this thesis, whose epitaxial structure is reported in Table 2.1, are slightly different. The main difference is the fact that on the upper side there are two Bragg mirrors only: simulations show no relevant reduction in the confinement capability, and the result is a more fabrication-friendly structure, with a more practical configuration in view of hybridization with other platforms, as will be explained in Section 4.2. Other differences are the reduction of the cap thickness and the presence of a layer of InGaP and of a so-called "etch-stop layer", whose function will become once again clear when considering the hybridization process. The layered structure can be visualized in Figures 2.5e and 2.5f, where the index and $\chi^{(2)}$ variations follow the aluminium concentrations, as described at the beginning of this section.

		M2AG018		**M2AG019**	
Layer	**Cycles**	Δz **(nm)**	x **(%)**	Δz **(nm)**	x **(%)**
Substrate	1	-	0	-	0
Etch-stop	1	300	85	300	85
Bottom cap	1	10	0	10	0
Bottom Bragg	6	320	80	280	80
		116	25	116	25
Core	1	364	25	364	45
Top Bragg	2	116	25	116	25
		320	80	280	80
Top cap	1	10	0	10	0
InGaP	1	10	-	10	-

Table 2.1: Nominal epitaxial structures of the two sources used in this work. Δz in the layer thickness, x is the relative Al concentration.

2.2.2. Modal phase-matching

In Section 2.1.2 we introduced the concept of modal phase-matching, which will be here applied to the case of our sources. In particular, we will focus our attention on how the design choices affect the phase-matching condition and the nonlinear efficiency.

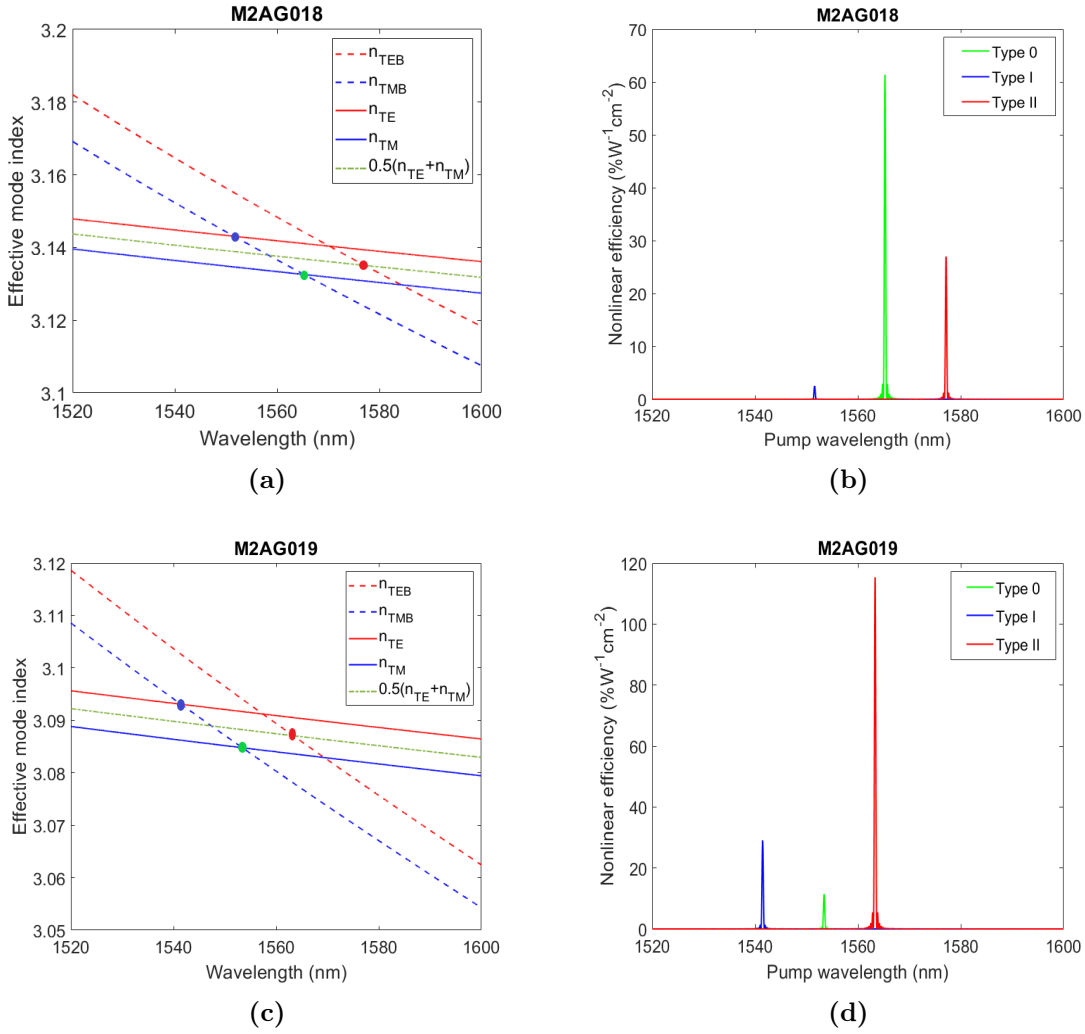

Figure 2.6: Simulated dispersion and SHG curves for the M2AG018 (a,b) and M2AG019 (c,d) waveguides. $n_{TE/TM}$ is the effective refractive index of the fundamental TE/TM modes, while $n_{TEB/TMB}$ is the one of the Bragg TE/TM modes; the values of $n_{TEB/TMB}$ refer to half the displayed wavelength, from 760nm to 800nm. The intersection points in the dispersion curves underline the different types of modal PM and have the same color coding used for the SHG profiles.

The dispersion curves, displayed in Figures 2.6a and 2.6c, are calculated with a 2D commercial eigenmode solver (Lumerical MODE): the fundamental and Bragg modes are retrieved per each frequency value, and the corresponding modal effective index is extracted. The PM condition, for the three types of available processes (see Section 2.1.3), can be written as:

1. **Type II**: $\omega_B n_{TEB}(\omega_B) = \omega_s n_{TE}(\omega_s) + \omega_i n_{TM}(\omega_i)$;

2. **Type I**: $\omega_B n_{TMB}(\omega_B) = \omega_s n_{TE}(\omega_s) + \omega_i n_{TE}(\omega_i)$;
3. **Type 0**: $\omega_B n_{TMB}(\omega_B) = \omega_s n_{TM}(\omega_s) + \omega_i n_{TM}(\omega_i)$,

where ω_B is the frequency of the Bragg mode, ω_s and ω_i the frequencies of the fundamental modes (such that $\omega_B = \omega_s + \omega_i$), $n_{TE/TM}$ the effective refractive index of the fundamental TE/TM modes, $n_{TEB/TMB}$ the one of the Bragg TE/TM modes. When considering the process of second harmonic generation, that is the degenerate case in which $\omega_i = \omega_s = \omega$ and $\omega_B = 2\omega$, the latter conditions turn into:

1. **Type II**: $n_{TEB}(2\omega) = \frac{1}{2}\left[n_{TE}(\omega) + n_{TM}(\omega)\right]$;
2. **Type I**: $n_{TMB}(2\omega) = n_{TE}(\omega)$;
3. **Type 0**: $n_{TMB}(2\omega) = n_{TM}(\omega)$.

Those conditions are satisfied in the points highlighted by colored circles in the dispersion curves, which let us thus retrieve the degeneracy or phase-matching wavelength. Starting from this information, together with the modes amplitude and phase and the $\chi^{(2)}$ profile (see Figure 2.5), we can calculate the nonlinear overlap integral with Equation (2.1) and simulate the SHG efficiency (Equation (2.3)) per unit of squared propagation length, as shown in Figures 2.6b and 2.6d. As will be discussed in Section 2.3, the degeneracy wavelength (or frequency) is a crucial parameter also for the generation of photon pairs: the photons produced by SPDC will be distributed around this wavelength within a certain bandwidth depending on the conversion process.

We can see how, by changing the parameters of the structure – thickness and concentration of the layers –, we can tune the phase-matching frequency and the conversion efficiency. In particular, the source M2AG018 was designed to optimize type 0 PM, while the M2AG019 to enhance type 1 and type 2 PM, keeping them within the telecom range. As a final observation, the degeneracy frequency can be also tuned with the temperature and the waveguide width, as discussed in [21]; here we considered a constant temperature of 300K and a waveguide width of 4μm.

2.2.3. Fabrication

We describe here the fabrication process to obtain the ridge AlGaAs waveguides used as photon pairs sources. This process is carried out in the clean rooms of the C2N laboratory (Palaiseau, France) and of the Université Paris Cité (Paris, France). After the epitaxial growth of the AlGaAs layers, the waveguides are etched either with chemical (after optical lithography) or inductively coupled plasma (ICP, after e-beam lithography) etching.

Sample growth

The heterostructure growth is performed by molecular beam epitaxy (MBE) at the Center of Nanoscience and Nanotechnology (C2N, Palaiseau, France) by Aristide Lemaître and Martina Morassi. The nominal epitaxial structures in Table 2.1 are grown on an undoped GaAs substrate along the [001] crystallographic direction, resulting in a layered wafer. During the MBE process, several molecular beams are sent on the wafer in ultra-high vacuum condition, and condense in a crystalline manner. It is therefore possible to finely control the chemical composition and the thickness of the deposited layer, with abrupt interfaces and low impurity level. The thickness uniformity is ensured by keeping the wafer in rotation during the deposition; the rotation can be stopped on demand to create structures with thickness gradient, for example to have different available phase-matching wavelength on the same sample (see Section 2.2.2). At the end of the growth, the wafer is analyzed with reflectometry spectroscopy (FTIR), from which we can retrieve information about the actual sample structure.

Sample preparation

Small portions (around 1cm by 1.5cm) of the epitaxially grown wafer are cleaved with the use of a diamond pen along the $[\bar{1}10]$ and $[1\bar{1}0]$ crystallographic axes. The sample is then carefully cleaned, to avoid the propagation of imperfections during the process. Thus, the sample is first stirred in an acetone bath, followed by an isopropanol bath and a deionized water bath; the surface cleaning is then completed with a light oxygen plasma, resulting in the neat structure in Figure 2.7a. The next step is the deposition of the photo-resist, functional to the lithography: the resist layer must be uniform to ensure a good lithography result. To do that, first an adhesion promoter is deposed to enhance the adherence of the resist, which is later spin-coated over it (Figure 2.7b). According to the type of lithography, we use a different combination of promoter and resist, as listed in Table 2.2. The resist thickness is set by the desired etching depth: the deeper the etching, the thicker the resist needed to protect the lithography pattern, at the cost of a reduction of accuracy. After the deposition, the sample is baked to remove all residual solvents from the resist.

	Optical litho	*Electronic litho*
Promoter	HMDS	SiO_2
Resist	S1805	HSQ

Table 2.2: Adhesion promoter and photo-resist according to the type of lithography.

Optical lithography and chemical etching

A glass mask with chromium patterns is used to drive the optical lithography. After the careful alignment between mask and sample, in order to have the waveguides patterns along the $[\bar{1}10]$ or $[1\bar{1}0]$ crystallographic axis, the system is exposed to ultraviolet (UV) radiation (Figure 2.7c): the exposure time changes the resist chemical nature, making it either soluble (positive resist) or insoluble (negative resist). The pattern is revealed through the resist development by means of its specific developer (MF319 in this case, Figure 2.7d).

The structure is now ready to be chemically etched (or wet etched). The most critical parameter is the etching height, set by the etching time. Our waveguides are typically either etched only in the top Bragg mirrors side (with the unetched core) or down to the end of the bottom Bragg mirrors, as it is the case for the structures considered in this work; in general, a deeper etching ensures higher modes confinement. The sample is slowly stirred at fixed temperature in a non-selective[6] isotropic etchant solution – hydrogen bromide (HBr), acetic acid (CH_3COOH) and potassium dichromate ($K_2Cr_2O_7$) in equal proportions – for around 25s per micrometer of etching. The remaining resist is then removed in an acetone bath, followed by an isopropanol bath (Figures 2.7e and 2.7f, for the case of a waveguide with unetched core). Finally, waveguides of the desired length (usually around 2mm) are produced by cleaving the sample with a diamond pen in the direction orthogonal to the waveguides; it is of great importance to check the quality of the obtained facets, to ensure good optical coupling.

The result is a waveguide with extremely smooth and curved flanks, being the chemical etching a highly isotropic process. This is not ideal for the control of the waveguide width, but the method is easy and rapid to implement, so extensively adopted. A scanning electron microscope (SEM) picture of a waveguide realized in this way is shown in Figure 2.8a.

E-beam lithography and ICP etching

For the e-beam lithography, a SEM module (Raith 5200 EBPG) is used to draw the waveguide patterns on the resist. The exposure to the electron beam changes the resist response to developer, and the exposure time is set by the employed dose and by the pattern length. The resist is then developed by a solution of Az400K and H_2O, which however does not remove the adhesion promoter – in our case, it is a 10nm layer of SiO_2 deposed via plasma enhanced chemical vapor deposition (PECVD). This is removed by

[6] All the layers, independently on their aluminium concentration, have to be etched in the same way.

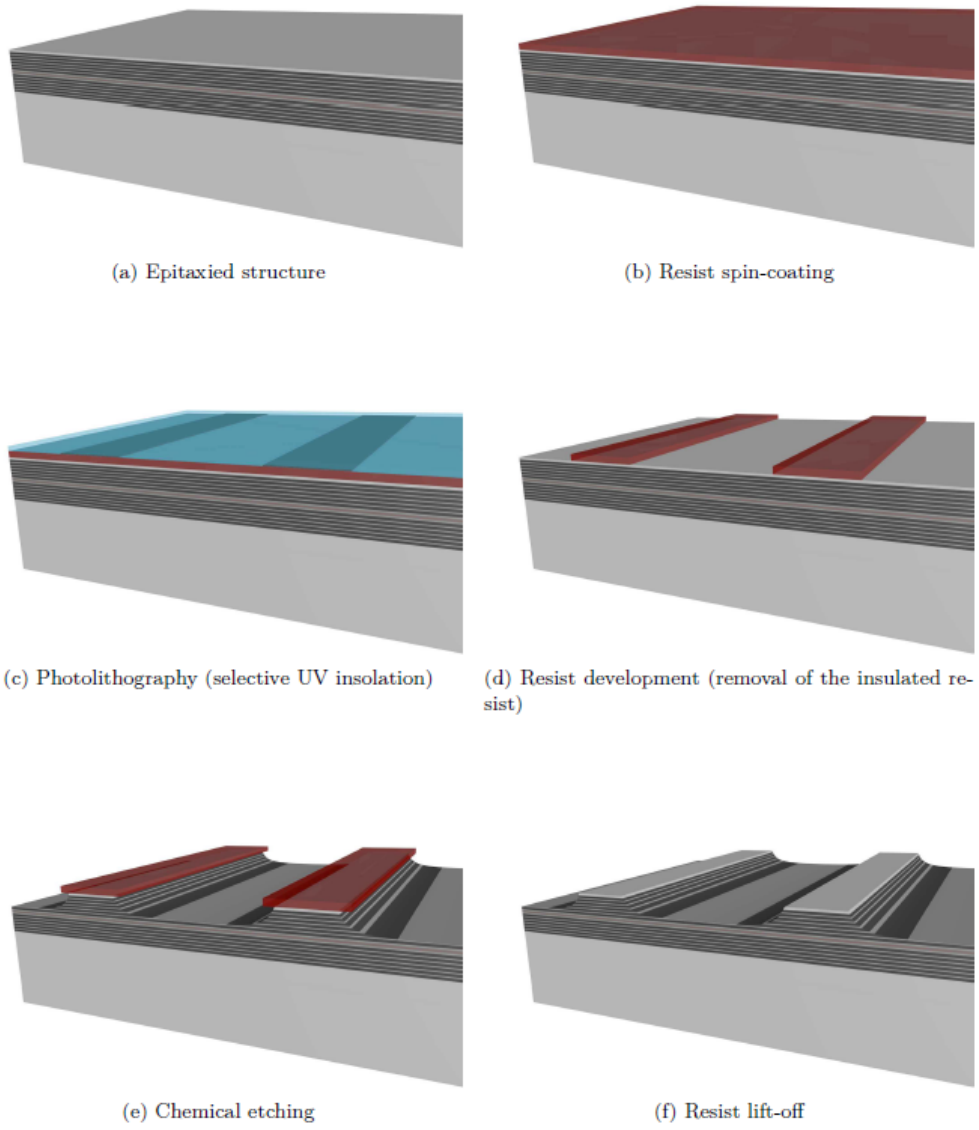

Figure 2.7: Steps for the optical chemical etching of the waveguide. From [21].

reactive ion etching (RIE), that does not affect neither the AlGaAs or the resist. The ICP etching (or dry etching) is at this point performed: it consists on a weakly chemically selective ion (in this case, mostly Br and O_2) bombardment of the sample to remove layers of material. Once finished, the remaining resist is lift off and the sample is cleaved.

This method is strongly directional, and the result is a waveguide with vertical sidewalls and finely defined width, as shown in Figure 2.8b. The drawbacks are the higher complexity and the longer process duration with respect to chemical etching.

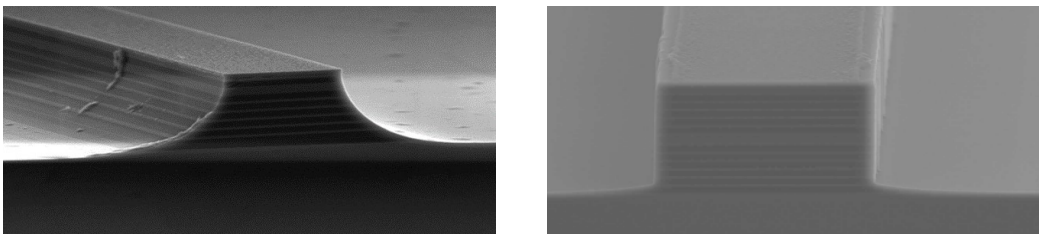

(a) (b)

Figure 2.8: SEM picture of (a) a chemically (wet) etched and (b) an ICP (dry) etched waveguide.

2.2.4. Electrically injected source

Here we briefly and essentially describe the electrically injected source based on AlGaAs Bragg reflector waveguides, demonstrated in our group [59]. Although it is not directly employed in this work, it represents its natural next development, as will be discussed in Section 4.3.2. It is therefore important to introduce the working principles, to have a better understanding of its potentialities, but also of the complexities to be faced. For the detailed and complete description of the device, we refer to the PhD thesis of A. Orieux [43].

The basic idea is to realize a semiconductor laser diode, in which the gain medium – in this case the AlGaAs, thanks to its direct bandgap – is a P-I-N junction. To do this, the different layers of our structure are properly doped during the epitaxial growth, and a quantum well, being a 10nm layer of $Al_{0.11}Ga_{0.89}As$, is grown in the core, in order to increase the laser efficiency thanks to the better confinement of the carriers. The scheme of the designed source is shown in Figure 2.9a. The cavity effect, necessary to amplify the radiation via stimulated emission, is naturally achieved at the facets of the waveguide, thanks to the high refractive index contrast between the guide itself and the air (around 3.2:1) and the high modal reflectivity of the Bragg mode (around 80%). The quantum well layer is too narrow to represent a dielectric guide for the laser mode, hence a separate confinement heterostructure scheme is used: the radiation is vertically confined by the layers of the core of the structure, at the condition that their refractive index is higher than the one experienced within the Bragg mirror layers.

The structure is designed to match the laser action, that must take place at $\lambda \sim 775nm$ generating a Bragg mode, with the nonlinear action of the waveguide, in order to produce photon pairs in the telecom range via SPDC (in the case of the demonstrated device, for type II phase-matching). The fabrication process becomes significantly more complex,

because of the deposition of the metallic contacts for the electrical pumping, as well as for the the doping of the layers within the growth process. A scheme of the final device is shown in Figure 2.9b.

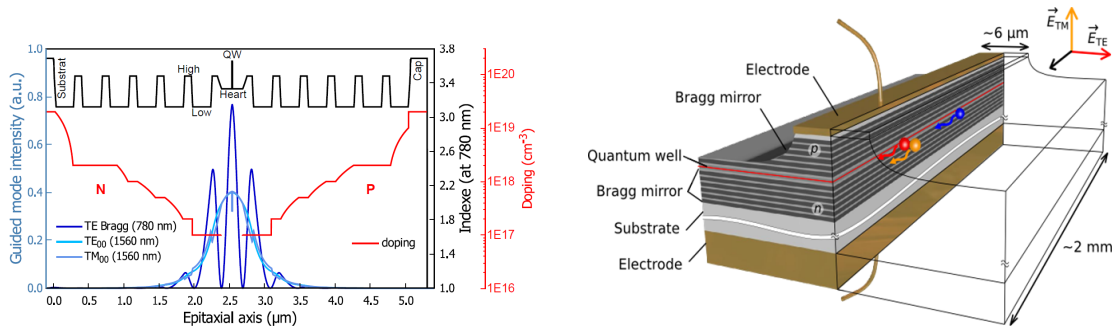

(a) **(b)**

Figure 2.9: Scheme of (a) the relevant design properties and of (b) the final device for the electrically injected source. From [21].

2.3. Generating quantum states

In this section, we develop the quantum theory of SPDC for the case of nonlinear waveguides and colinear propagation of the pump and the generated photons. The spectral properties of the generated quantum states are then discussed through the introduction of the joint spectral amplitude (JSA) function.

2.3.1. Colinear spontaneous parametric down-conversion

In Section 1.2.1, we built a simple model for explaining the spontaneous parametric down-conversion process; here we consider the case in which this process happens in waveguides. First of all, it is therefore necessary to take into account the fact that we are dealing with electromagnetic modes confined in the guide, with a given transverse profile (Bragg mode for the pump, fundamental Gaussian modes for the generated photons; see Figure 2.5). Considering that we are in a guided regime, the wavevector of mode i is $\mathbf{k}_i = k_i(\omega)\hat{\mathbf{u}}_\mathbf{y}$, with $k_i > 0$. The pump mode, which can be considered undepleted during the process due to the very low conversion efficiency, can be treated classically and be written as:

$$\mathbf{E}_p(\mathbf{r},t) = \frac{1}{\sqrt{2\pi}} \int_0^{+\infty} \mathrm{d}\omega \hat{\mathbf{u}}_p E_p(\mathbf{r},\omega) e^{i(k_p(\omega)y - \omega_p t)} + c.c., \tag{2.11}$$

where $\hat{\mathbf{u}}_p$ corresponds to either a TE or TM polarized pump mode, according to the type on phase-matching selected for the process. Signal (s) and idler (i) modes can be

expressed as quantum field operators, and take the form of [60]:

$$\begin{aligned}\hat{\mathbf{E}}_l(\mathbf{r},t) &= \sqrt{\frac{L}{2\pi}}\int_0^{+\infty} \mathrm{d}\omega_l \hat{\mathbf{u}}_l \frac{1}{\sqrt{v_g^l(\omega)}} E_l(\mathbf{r},\omega) e^{i(k_l(\omega)y-\omega_l t)}\hat{a}(\omega) + H.c. \\ &= \hat{\mathbf{E}}_l^{(+)}(\mathbf{r},t) + \hat{\mathbf{E}}_l^{(-)}(\mathbf{r},t),\end{aligned} \tag{2.12}$$

where $l \in (s,i)$, $\hat{\mathbf{u}}_l$ is set by the phase-matching type, the term $\sqrt{L}$ arises from the modes normalization given the continuity of k along the propagation direction, and the term containing the group velocity $v_g^l = \partial\omega_l/\partial k$ is added to ensure a canonical form for the annihilation and creation operators in the frequency domain. The operator $\hat{\mathbf{E}}_l^{(+)}(\mathbf{r},t)$ annihilates a photon in the l mode, while its Hermitian conjugate, $\hat{\mathbf{E}}_l^{(-)}(\mathbf{r},t)$, creates one.

The Hamiltonian operator describing the second order interactions driven by the nonlinear medium within the waveguide structure can be written as:

$$\hat{H}_{NL}(t) = \epsilon_0 \int_V \mathrm{d}^3\mathbf{r}\chi^{(2)}\hat{\mathbf{E}}_p(\mathbf{r},t)\hat{\mathbf{E}}_s(\mathbf{r},t)\hat{\mathbf{E}}_i(\mathbf{r},t). \tag{2.13}$$

Between all possible interactions, we consider the one in which a pump photon annihilates and a signal and an idler photon are generated, represented by $\hat{\mathbf{E}}_p^{(+)}\hat{\mathbf{E}}_s^{(-)}\hat{\mathbf{E}}_i^{(-)}$, where $\hat{\mathbf{E}}_p^{(+)}$ is, by analogy, the first term on the right-hand side in Equation (2.11)[7]. Thus, the Hamiltonian describing our interaction turns into:

$$\hat{H}_{NL}(t) = \epsilon_0 \int_V \mathrm{d}^3\mathbf{r}\chi^{(2)}\hat{\mathbf{E}}_p^{(+)}(\mathbf{r},t)\hat{\mathbf{E}}_s^{(-)}(\mathbf{r},t)\hat{\mathbf{E}}_i^{(-)}(\mathbf{r},t), \tag{2.14}$$

which is the equivalent of Equation (1.21) when considering that the interaction is taking place in a waveguide.

The temporal evolution of the state of the system, $|\Phi(t)\rangle$, is governed by the Schrödinger equation; in low pump regime we can adopt a perturbation approach, such that the state at time t can be written as:

$$\begin{aligned}|\Psi(t)\rangle &= |0\rangle + \frac{1}{i\hbar}\int_{-\infty}^{t} \mathrm{d}t\hat{H}_{NL}(t)|0\rangle \\ &= |0\rangle + \beta|\psi\rangle,\end{aligned} \tag{2.15}$$

where we have assumed that the initial state is the vacuum state, $|0\rangle = |0_s, 0_i\rangle$. $|\psi\rangle$ is

[7]Note that the equivalence between the pump field operator and its expectation value – which is the classical field expression in this case – is valid within the parametric approximation, as discussed in Section 1.2.1.

the biphoton state generated after the interaction, and β is the generation probability amplitude. Therefore:

$$|\psi\rangle = \frac{1}{i\beta\hbar}\int_{-\infty}^{t} \mathrm{d}t\hat{H}_{NL}(t)|0\rangle; \tag{2.16}$$

when plugging Equations (2.14), (2.11) and (2.12) into (2.16), we obtain:

$$\begin{aligned}|\psi\rangle = \frac{\epsilon_0 L}{i\beta\hbar(2\pi)^{3/2}}\iiint \mathrm{d}\omega_p\mathrm{d}\omega_s\mathrm{d}\omega_i \int_V \mathrm{d}^3\mathbf{r}\chi^{(2)}(\mathbf{r})E_p(\mathbf{r},\omega_p)E_s(\mathbf{r},\omega_s)E_i(\mathbf{r},\omega_i) \\ \times\frac{e^{i\Delta k y}}{\sqrt{v_g^s(\omega_s)v_g^i(\omega_i)}}\left(\int \mathrm{d}t e^{-i\Delta\omega t}\right)\hat{a}_s^\dagger(\omega_s)\hat{a}_i^\dagger(\omega_i)|0\rangle,\end{aligned} \tag{2.17}$$

where $\Delta k = k_p(\omega_p) - k_s(\omega_s) - k_i(\omega_i)$ is the phase mismatch between the three interacting photons, $\Delta\omega = \omega_p - \omega_s - \omega_i$ is the difference between their frequencies. We note that:

$$\int \mathrm{d}t e^{-i\Delta\omega t} = 2\pi\delta(\Delta\omega) \tag{2.18}$$

is simply the condition of energy conservation, so that the integral over ω_p results in the same expression but with the substitution $\omega_p \to \omega_s + \omega_i$. We can now introduce the so-called *joint spectral amplitude* (JSA) function, $C(\omega_s, \omega_i)$, such that the two-photon state can be written as:

$$|\psi\rangle = \iint \mathrm{d}\omega_s\mathrm{d}\omega_i C(\omega_s,\omega_i)\hat{a}_s^\dagger(\omega_s)\hat{a}_i^\dagger(\omega_i)|0\rangle. \tag{2.19}$$

2.3.2. The joint spectral amplitude

The JSA is a complex-valued probability amplitude: its modulus squared, $|C(\omega_s,\omega_i)|^2$, which goes under the name of *joint spectral intensity* (JSI), gives the probability that the two-photon state is composed by a signal photon at frequency ω_s and an idler photon at frequency ω_i. Note that, for this reason, the JSI function must be normalized: $\iint \mathrm{d}\omega_s\mathrm{d}\omega_i|C(\omega_s,\omega_i|^2 = 1$; being a spectral density, the JSA has the dimension of a time ([s]), in accordance with the normalization condition. By comparing Equations (2.17) and (2.19) we get:

$$\begin{aligned}C(\omega_s,\omega_i) = \frac{\epsilon_0}{i\beta\hbar\sqrt{2\pi}}\frac{L}{\sqrt{v_g^s(\omega_s)v_g^i(\omega_i)}} \\ \times\underbrace{\int \mathrm{d}^3\mathbf{r}\chi^{(2)}(\mathbf{r})E_p(\mathbf{r},\omega_s+\omega_i)E_s(\mathbf{r},\omega_s)E_i(\mathbf{r},\omega_i)e^{i\Delta k y}}_{\star}.\end{aligned} \tag{2.20}$$

As long as pump, signal and idler are supported by the waveguide, their transverse spatial distribution can be considered constant with the frequency, so that: $E_{s,i}(\mathbf{r}, \omega_{s,i}) \approx E_{s,i}(x,z)$ and $E_p(\mathbf{r}, \omega_s + \omega_i) \approx \phi_p(\omega_s + \omega_i) E_p(x,z)$, being $\phi_p(\omega_s + \omega_i)$ the pump spectral distribution. The star term in Equation (2.20) can be thus rewritten as:

$$\begin{aligned} \star &= \phi_p(\omega_s + \omega_i) \int \mathrm{d}y e^{i\Delta k y} \iint \mathrm{d}x \mathrm{d}z \chi^{(2)}(x,z) E_p(x,z) E_s(x,z) E_i(x,z) \\ &= \phi_p(\omega_s + \omega_i) \phi_{PM}(\omega_s, \omega_i) \bar{\Gamma}, \end{aligned} \tag{2.21}$$

where $\bar{\Gamma}$ is the non-normalized[8] nonlinear overlap integral (compare with Equation (2.1)), and we defined the *phase-matching function*, ϕ_{PM}, as:

$$\phi_{PM}(\omega_s, \omega_i) = \int_0^L \mathrm{d}y e^{i\Delta k y} = L e^{i\Delta k \frac{L}{2}} \mathrm{sinc}\left(\Delta k \frac{L}{2}\right), \tag{2.22}$$

where the dependence on the signal and idler frequencies is embedded in the phase mismatch term. Finally, by substituting the new expression of the star term in Equation (2.20), we can write:

$$C(\omega_s, \omega_i) \propto \phi_p(\omega_s + \omega_i) \phi_{PM}(\omega_s, \omega_i). \tag{2.23}$$

For what concerns the pump spectral distribution, it is typically assumed to have a Lorentzian shape, such that:

$$\phi_p(\omega) = \frac{1}{\pi \Delta\omega_p} \left[\frac{\Delta\omega_p^2}{(\omega - \omega_p)^2 + \Delta\omega_p^2}\right], \tag{2.24}$$

being $\Delta\omega_p$ the full width at half maximum (FWHM) of the function. In the condition of narrow pump[9], it can be approximated with a Dirac delta function, so that $\phi_p(\omega) \propto \delta(\omega - \omega_p)$: in this case, strong frequency anti-correlation arises between the generated photons, due to the fact that $\omega_p = \omega_s + \omega_i \simeq const.$ In Figure 2.10 the pump spectral distribution is displayed in the (ω_s, ω_i) domain for different linewidths: the narrower the spectral distribution, the stronger will be the anti-correlation.

Note that in all this discussion we have ignored the cavity effects induced by the reflectivity of the waveguide facets. For a detailed analysis we refer to the PhD thesis of G. Maltese [56].

[8] To be more precise, the field amplitudes involved in the computation are not, here, normalized.

[9] This condition is achieved when the linewidth of the pump is much narrower than the bandwidth of the emitted photons, set by the phase-matching function. This is the case for our experiments, as will be detailed in Section 3.3.1.

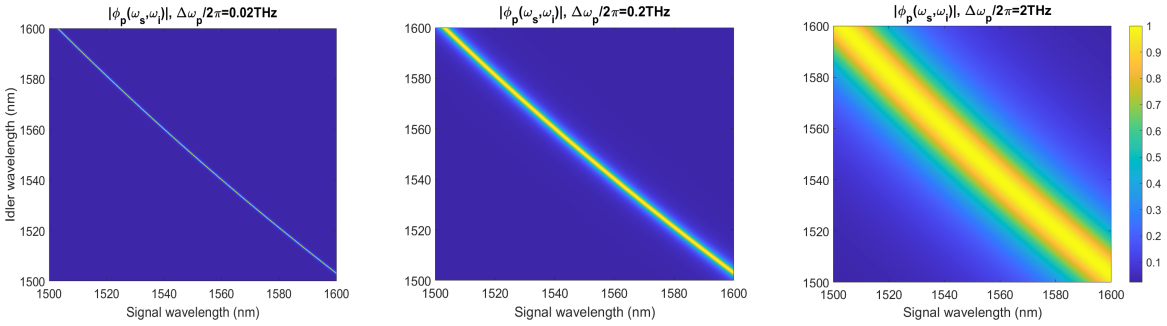

(a) **(b)** **(c)**

Figure 2.10: Pump spectral distribution in the (ω_s, ω_i) domain, for different values of the Lorentzian linewidth: (a) 20GHz, (b) 200GHz and (c) 2THz.

2.3.3. Effect of the phase mismatch

For what concerns the phase-matching function (Equation (2.22)), the key role is played by the phase mismatch, Δk:

$$\begin{aligned}\Delta k &= \frac{1}{c}[\omega_p n_p(\omega_p) - \omega_s n_s(\omega_s) - \omega_i n_i(\omega_i)] \\ &= \frac{1}{c}\left[\omega_+ n_p(\omega_+) - \left(\frac{\omega_+ + \omega_-}{2}\right) n_s\left(\frac{\omega_+ + \omega_-}{2}\right) - \left(\frac{\omega_+ - \omega_-}{2}\right) n_i\left(\frac{\omega_+ - \omega_-}{2}\right)\right],\end{aligned} \tag{2.25}$$

where we have introduced a new useful basis, $(\omega_+, \omega_-) \leftrightarrow (\omega_s + \omega_i, \omega_s - \omega_i)$. Recalling that, at first order[10], we can write $n(\omega + \Delta\omega) \simeq n(\omega) + \Delta\omega \left.\frac{\mathrm{d}n}{\mathrm{d}\omega}\right|_\omega$, we are able to spot and separate three different contributions to the mismatch and their effect on ϕ_{PM}:

$$\Delta k = \Delta k_{modal}(\omega_+) + \Delta k_{birefringence}(\omega_-) + \Delta k_{dispersion}(\omega_-). \tag{2.26}$$

With reference to Figure 2.11, Δk_{modal} is the modal birefringence mismatch, related to the difference in effective index between the involved Bragg mode and fundamental modes, Δn_{modal}:

$$\Delta k_{modal} = \frac{\omega_+}{c}\left[n_p(\omega_+) - \frac{n_s(\omega_+/2) + n_i(\omega_+/2)}{2}\right] = \frac{\omega_+}{c}\Delta n_{modal}(\omega_+). \tag{2.27}$$

[10]This approximation is valid as far as the bandwidth of the emitted two-photon state, $\Delta\omega$, is small enough compared to the degeneracy frequency, ω, so that $\Delta\omega/\omega \ll 1$.

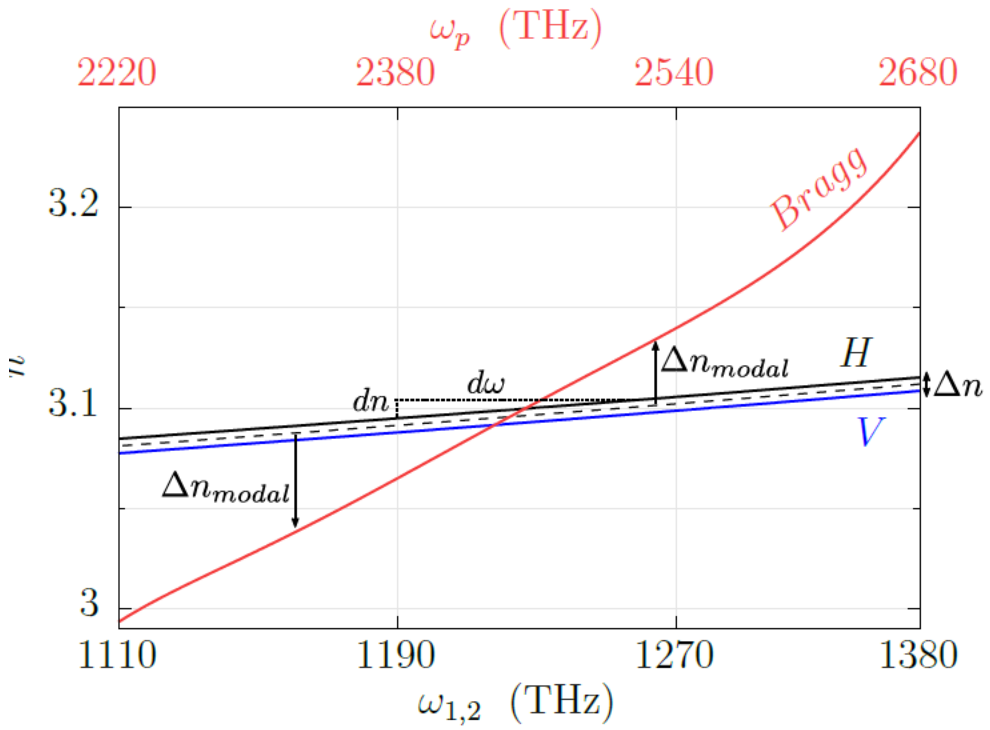

Figure 2.11: Simulated dispersion curves for the three interacting modes in a type II phase-matching process, with $\omega_{1,2} = \omega_{s,i}$. From [56].

We note that, independently from the respective polarization of the signal and idler photons, the variation of refractive index with the frequency is equivalent and linear: $\frac{\mathrm{d}n_s}{\mathrm{d}\omega}\Big|_{\omega_+/2} = \frac{\mathrm{d}n_i}{\mathrm{d}\omega}\Big|_{\omega_+/2} = \frac{\mathrm{d}n}{\mathrm{d}\omega}\Big|_{\omega_+/2}$. We can define Δn as the constant birefringence between signal and idler modes, thus getting:

$$\Delta k_{birefringence}(\omega_-) = -\left(\frac{\omega_-}{2c}\right)\left[n_s\left(\frac{\omega_+}{2}\right) - n_i\left(\frac{\omega_+}{2}\right)\right] = -\left(\frac{\omega_-}{2c}\right)\Delta n; \tag{2.28}$$

note that Δn is null for type 0 and type 1 phase-matching processes, and so the birefringence contribution to the phase mismatch. The last term remaining from the first order expansion is $\Delta k_{dispersion}$, being proportional to the chromatic dispersion ($\mathrm{d}n/\mathrm{d}\omega$) of the signal and idler modes:

$$\Delta k_{dispersion}(\omega_-) = -\left(\frac{\omega_-^2}{2c}\right)\frac{\mathrm{d}n}{\mathrm{d}\omega}\Big|_{\omega_+/2}. \tag{2.29}$$

Finally, we can rewrite the phase-matching function in (2.22) as:

$$\phi_{PM}(\omega_+, \omega_-) \propto \mathrm{sinc}\left\{\frac{L}{2c}\left[\omega_+\Delta n_{modal}(\omega_+) - \omega_-\left(\frac{\Delta n}{2} + \frac{\omega_-}{2}\frac{\mathrm{d}n}{\mathrm{d}\omega}\Big|_{\omega_+/2}\right)\right]\right\}. \tag{2.30}$$

The detailed discussion on the effect of all the different contributions is carried out in [56]. In particular, the dispersion term gives a parabolic profile to the JSA, while, if present, the birefringence term introduces a branch centred in $\omega_- = -\Delta n(\mathrm{d}n/\mathrm{d}\omega)^{-1}$ in the (ω_+, ω_-) plan. The final shape of the phase-matching function, for the case of a type 2 process, is shown in Figure 2.12a. The pump frequency sets the region of the JSA that we are slicing along the ω_+ axis, as highlighted by the grey line. The resulting JSA is shown in Figure 2.12b, where the bandwidth $\Delta\omega$ of the biphoton state is indicated.

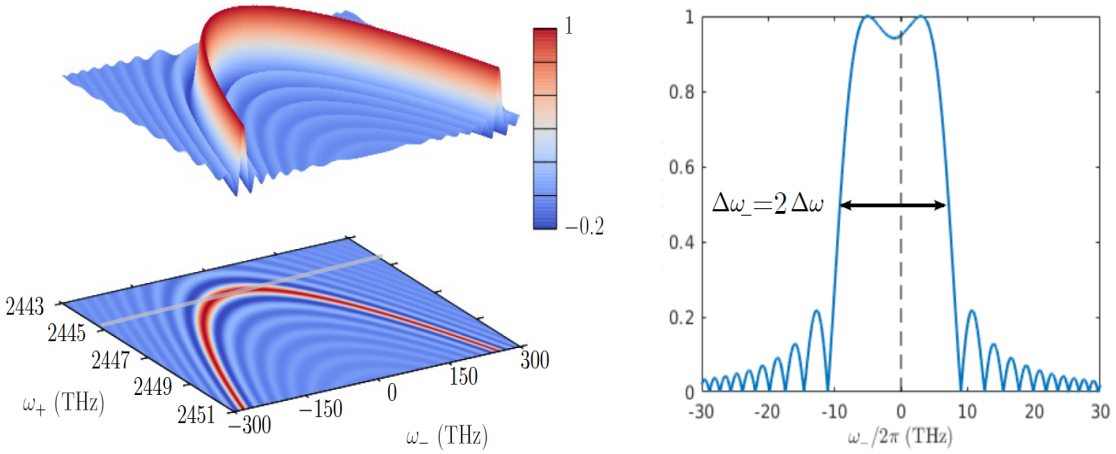

(a) **(b)**

Figure 2.12: (a) Simulated phase-matching function; (b) resulting JSA when pumping with a narrow spectrum pump at the frequency highlighted by the grey line.

3 | Device characterization

The device introduced in Chapter 2 is here characterized in terms of linear, nonlinear and quantum properties and performances. First, we describe how to evaluate the optical transmission of the waveguides; second, how to generate and collect second harmonics, so to determine the phase-matching frequency resonance. Finally, the photon pair production rate is measured, together with the level of entanglement in energy-time.

3.1. Optical losses

As pointed out in Section 1.3.2, low transmission losses are a crucial requirement for photon-pair sources, in order to ensure a large enough signal-to-noise ratio for the desired applications and for the obvious necessity of conserving both photons of the pair during the propagation through the waveguide. Here we describe a method for directly quantifying the optical losses for the fundamental TE and TM infrared modes supported by the structure, and the setup used for the measurement.

3.1.1. Fabry-Perot fringes method

Optical losses are characterized via the attenuation coefficient, α, describing the exponential decay of the optical intensity with the propagation through a medium of length L, such that:

$$I_{OUT} \simeq I_{IN} e^{-\alpha L}, \tag{3.1}$$

where $I_{IN,OUT}$ is the input or output intensity. The attenuation coefficient is thus measured in cm^{-1} (or in dB/cm, especially for low-loss materials), and the higher the coefficient, the higher the losses of the medium. To retrieve this coefficient, we use a method developed in [61] and extended to the case of semiconductor waveguides by our team [62]. The idea is to exploit the cavity effects induced by the waveguide itself (see Section 2.2.4); when injecting with a tunable narrow-band laser in the telecom range, interference phe-

nomena are visible in the beam transmitted by the guide[1], displaying Fabry-Perot fringes whose contrast is directly related to the attenuation coefficient. In particular:

$$T(\lambda) = \eta(1-R)^2\mathcal{F}(\lambda)e^{-\alpha L}, \tag{3.2}$$

where $T(\lambda)$ is the mode transmission at wavelength λ, R the modal reflectivity at the facets (simulated with Lumerical FDTD for a given structure and a given propagation mode), η the coupling efficiency into the waveguide mode and $\mathcal{F}$ the so-called Fabry-Perot function, defined as:

$$\mathcal{F}(\lambda) = \frac{1}{(1-Re^{-\alpha L})^2 + 4Re^{-\alpha L}\sin^2[\phi(\lambda)]}, \tag{3.3}$$

where the phase factor

$$\phi(\lambda) = \phi_0 + 2\pi n_{eff}\frac{L}{\lambda} \tag{3.4}$$

takes into account the phase accumulated during the propagation and causes the interference pattern. Note that n_{eff} depends on the frequency, but it can be considered constant in the measurement interval (typically few nanometers of wavelength variation). If we define the contrast of the Fabry-Perot fringes as $K = (T_{max} - T_{min})/(T_{max} + T_{min})$, we obtain:

$$\alpha = \frac{1}{L}\ln\left(\frac{RK}{1-\sqrt{1-K^2}}\right). \tag{3.5}$$

3.1.2. Experimental setup and results

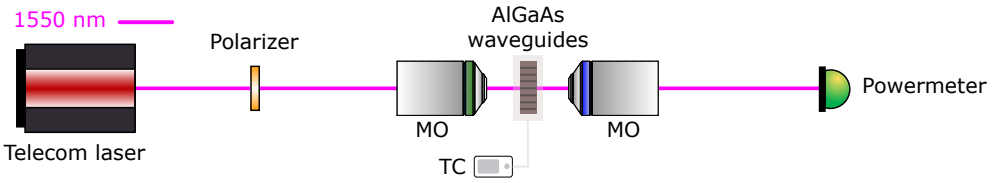

Figure 3.1: Scheme of the setup for the optical losses measurement. MO: microscope objective; TC: temperature controller.

In Figure 3.1, the setup used to perform this type of measurement: a continuous-wave (CW) laser (in our case, a *Tunics*, tunable from 1500 to 1630nm, with spectral width 2kHz) is coupled into the waveguide through a microscope objective (40x, 0.60 of numerical aperture, NA); the transmitted mode is collected via another microscope objective (63x,

[1]According to the selected input frequency and to the length of the cavity, we will have constructive or destructive interference, resulting, respectively, in maxima and minima of the transmitted optical intensity.

NA=0.90) and then sent to a powermeter, sensitive in the near-IR. The input polarization is set by a polarizer, while the temperature of the sample is kept constant through the use of an active temperature controller. The laser wavelength is swept within a given range (typically, few nanometers) with a fine step (typically, 0.01nm). Note that, according to Equation (3.5), the measurement of the attenuation coefficient is unaffected by the coupling efficiency, being a relative measurement based on the contrast. The results are shown in Figure 3.2. The slight variation of the peak power with the wavelength is induced by small variations of the polarization of the beam at the output of the laser, and by multi-mode effects [62]: however, the contrast within each oscillation period is constant, not depending on the input power. Note that, to resolve such fringes, the laser linewidth must be much narrower than their free-spectral range (FSR), which is defined by the length of the cavity; in this case, FSR≃25GHz (0.2nm), much larger than the laser linewidth.

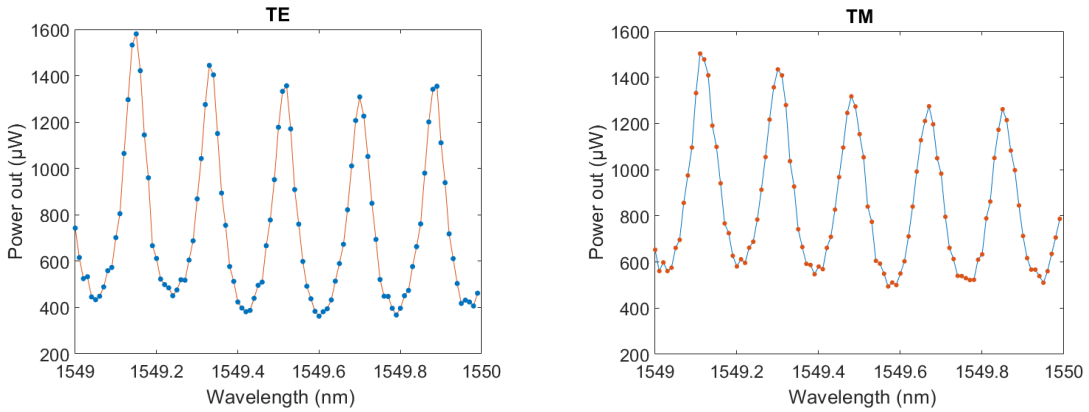

Figure 3.2: Measured optical transmission for (a) TE and (b) TM fundamental modes, for a M2AG018 ICP-etched waveguide of width 3.5μm.

In Table 3.1 we list a series of measured values of the attenuation coefficient for different analysed structures. In general, we observe that the simulated reflectivity is almost equivalent for dry or wet etched structures, while the reflectivity for the TE mode is significantly larger than the one for the TM mode. This leads to larger calculated losses for the TE mode with respect to the ones for the TM mode. No significant differences are observed between the transmission of dry and wet etched waveguides: in fact, the variation of width for the core in the wet etched structure is negligible within its thickness, as can be observed in Figure 2.8. For a given structure, the larger the waveguide, the lower the losses; for too large guides, though, multi-mode transmission becomes possible, eventually spreading the power between higher order modes. In general, losses for the TE

mode are lower than the ones of the TM mode for large structures, and higher for narrow structures; the reason is that the confinement of the TE mode, being the field distributed along the horizontal direction, is more affected by width (thus, horizontal) variations.

Epitaxy	**Etching**	**Mode**	R	α **(cm^{-1})**
M2AG018	*Wet*	TE	0.341	1.49
		TM	0.254	0.70
	Dry	TE	0.340	2.12
		TM	0.255	0.34
M2AG019	*Wet*	TE	0.287	1.60
		TM	0.234	0.34
	Dry	TE	0.287	1.32
		TM	0.235	0.43

Table 3.1: Measured attenuation coefficients (α) for TE and TM modes, for different epitaxial structures and etchings: for dry etching the ridge width is 4μm, for wet etching the width at the core centre is 4.22μm, as a result of setting the width of the cap to 4μm. The value of the facets reflectivity is simulated with Lumerical FDTD.

The attenuation coefficient can be also retrieved by directly measuring the input and output power: with the same setup as in Figure 3.1, the input power P_{IN} is measured by putting the powermeter right after the polarizer, while the output power P_{OUT} with the powermeter as shown. We can thus write:

$$P_{OUT} \simeq \eta P_{IN} e^{-\alpha L}, \tag{3.6}$$

so that:

$$\alpha = \frac{1}{L} \ln \left(\frac{\eta P_{IN}}{P_{OUT}} \right). \tag{3.7}$$

η is an efficiency factor, taking into account the injection efficiency, η_{IN}, of the first microscope objective – the portion of mode that is collected by and comes out from the injection objective –, the coupling efficiency η_c – the portion of mode that actually enters the waveguide – and the collection efficiency, η_{COL}, of the second objective, so that $\eta = \eta_{IN}\eta_c\eta_{COL}$. These quantities can be inferred and experimentally characterized; however, the result is strongly dependent on the setup alignment, which is not ideal. Cavity effects can be averaged out with a spectral average over the transmitted power, for estimating the mean optical transmission of the waveguide.

3.2. Second harmonic generation efficiency

Second harmonic generation is, conceptually, the inverse process to spontaneous parametric down-conversion: it represents an useful characterization of the second order nonlinearity of the device, and it is essential to retrieve the phase-matching resonance wavelength (λ_{PM}), as discussed in Section 2.2.2. Here, we introduce a further level of detail in the analysis, considering the contributions of linear losses and of cavity effects, and we describe the experimental setup used for the measurements, showing the obtained results.

3.2.1. Losses and cavity effects

The parametric conversion efficiency of the waveguide is characterized through a second harmonic generation process (see Equations (2.3) and (2.4)). In addition of what discussed in Section 2.1.1, for a more complete description, closer to the experimental reality, we need to include the combined effects of the optical losses, of the coupling efficiency and of the facets' reflectivity on the conversion process. Considering these contributions, we get [63]:

$$\begin{aligned} P_{SHG} =& \eta L^2 \eta^0_{SHG} P^2_{IR} (1 - R_{SHG})(1 - R_{IR,1})(1 - R_{IR,2}) \mathcal{F} \\ & \times \frac{\sin^2\left(\frac{\Delta k L}{2}\right) + \sinh^2\left((\alpha_{IR,1} + \alpha_{IR,2} - \alpha_{SHG})\frac{L}{4}\right)}{\left(\frac{\Delta k L}{2}\right)^2 + \left((\alpha_{IR,1} + \alpha_{IR,2} - \alpha_{SHG})\frac{L}{4}\right)^2} e^{-(\alpha_{IR,1}+\alpha_{IR,2}+\alpha_{SHG})\frac{L}{2}}, \end{aligned} \tag{3.8}$$

where P_{IR} is the IR pump optical power, R_{SHG} and α_{SHG} the modal reflectivity and the attenuation coefficient of generated Bragg mode, $R_{IR,i}$ and $\alpha_{IR,i}$ ($i \in 1, 2$) the modal reflectivities and attenuation coefficients of the involved pump modes, $\mathcal{F} = \mathcal{F}_{SHG}\mathcal{F}_{IR,1}\mathcal{F}_{IR,2}$ the combined Fabry-Perot function (see Equation (3.3)). Simulations showing the effects of the variation of some of the parameters in (3.8) – especially L and α_{SHG} – are displayed in Figure 3.3, in terms of normalized SHG function, defined as $P_{SHG}/(\eta L^2 \eta^0_{SHG} P^2_{IR})$. The cavity introduces an interference pattern, with maxima and minima according to the phase shift between the interacting modes; losses, as expected, exponentially decrease the transmitted power.

3.2.2. Experimental setup and results

Even if GaAs is one of the materials with the highest second order nonlinearity, the produced second harmonic signal is of the order of nanoWatts, when the pump beam power is around 10mW. For this reason, a more complex setup with a signal-recovery module is required. We use a lock-in amplifier (SRS830), combined with a beam chopper before

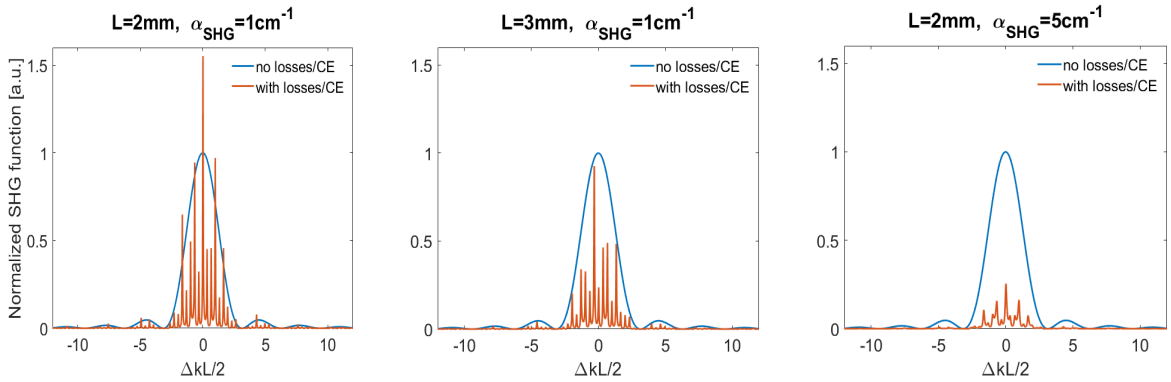

Figure 3.3: Numerical simulations of the normalized SHG function, with (orange curve) or without (blue curve) considering the waveguide losses and cavity effects (CE). Fixed parameters: $\alpha_{IR,i} = 1cm^{-1}$ and $R_{IR,i} = 0.25$ for $i \in 1, 2$, $R_{SHG} = 0.8$.

the input objective, modulating the input field at a given frequency (in our experiments, 600Hz); the amplitude and the phase of the modulated signal are then recovered. A scheme of the setup is shown in Figure 3.4: the pump beam coming from the narrow-band CW telecom laser is polarized, modulated and coupled into the waveguide, which is kept stable in temperature by an external controller. At the output of the sample, if we are pumping at the resonance wavelength for the phase-matching (see Section 2.2.2), we will collect both the transmitted pump and the SHG signal, at double the frequency. The transmitted pump is cut off with a low-pass[2] filter (cutoff wavelength 1000nm), and the SHG signal is sent to a Si photodiode, whose electric output signal is amplified and fed into the lock-in amplifier.

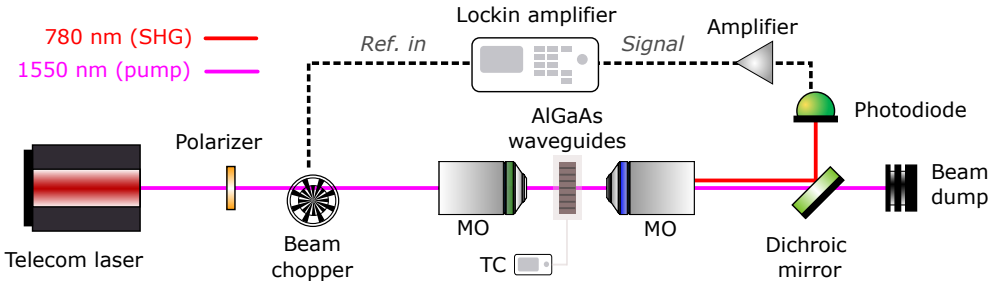

Figure 3.4: Scheme of the setup for the SHG measurement. MO: microscope objective, TC: temperature controller.

According to the polarization of the pump beam, we will be able to excite different processes, among the available ones:

[2]Low-pass in terms of wavelength, high-pass in terms of frequency: if not specified differently, we will always refer to the wavelength in the followings.

1. **TM-polarized pump**: type 0 conversion, TM($2\lambda_{PM0}$)+TM($2\lambda_{PM0}$)→TM(λ_{PM0});
2. **TE-polarized pump**: type 1 conversion, TE($2\lambda_{PM1}$)+TE($2\lambda_{PM1}$)→TM(λ_{PM1});
3. **45°-polarized pump**: both type 0 and type 1 processes, and type 2 phase-matching conversion, TE($2\lambda_{PM2}$)+TM($2\lambda_{PM2}$)→TE(λ_{PM2}).

Note that the selected conversion process determines the values of the modal reflectivities and of the attenuation coefficients to be inserted in Equation (3.8). In our structure, we where able to retrieve all the three types of conversion, as shown in Figure 3.5, where we recorded the amplitude of the generated beam at λ_{PM} as a function of the pump wavelength, $2\lambda_{PM}$. The input polarization was set to 45°, in order to have access to all the conversion processes; for verifying the phase-matching type, one can simply add a polarizer at the output of the collection microscope. Later, we repeated the experiment with the TM or TE polarized pump, to retrieve the actual conversion efficiencies for the type 0 and type 1 processes.

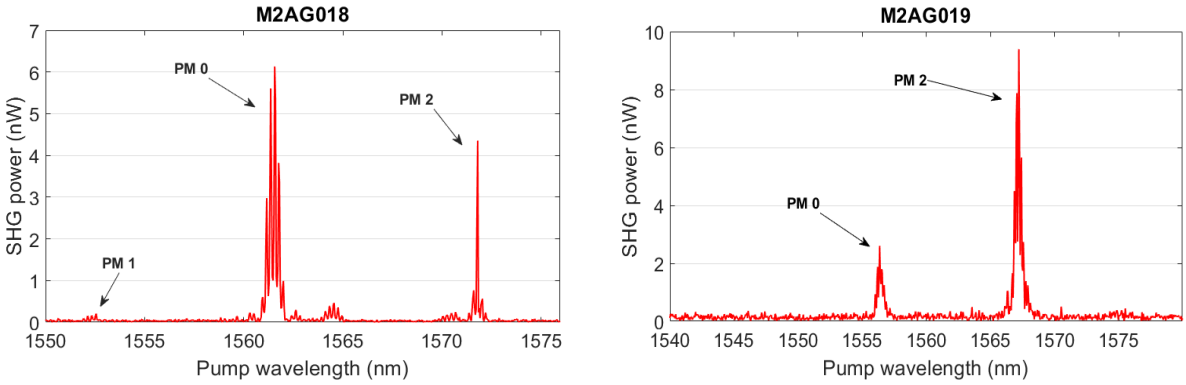

(a) (b)

Figure 3.5: Result of the SHG measurement, with the three phase-matching types indicated, where detected. Epitaxy (a) M2AG018 and (b) M2AG019, wet etching, ridge width 4.5μm, temperature 25°C.

By comparing Figure 2.6b with Figure 3.5a, we can say that, for the epitaxy M2AG018, the experimental results reproduce with good accuracy what expected from simulations, at least for what concerns the relative efficiencies and positions of the peaks. From the point of view of the absolute conversion efficiency, we have a factor of around 100 between the predicted and the measured SHG optical power: this is compatible with the combined effect of the losses and the cavity – as discussed at the beginning of this section –, but also of the limited coupling and detection efficiency, whose overall contribution is estimated to be $\eta \sim 10\%$. Focusing on the peaks' positions, we analysed their variation as a function

of the ridge width: an array of dry etched waveguides[3] with different widths was used for the measurement, whose result is shown in Figure 3.6a. The theoretical models are able to predict with good precision the degeneracy wavelength for the three phase-matching types: slight offsets are mainly due to non-idealities between the nominal structure and the fabricated one. Therefore, the ridge width is demonstrated to be an additional parameter to adjust λ_{PM}, whose fine control is crucial for several applications [64].

Considering the SHG measurement for the epitaxy M2AG019 displayed in Figure 3.5b, the very same comments can be done for type 0 and type 2 phase-matching peaks. However, the type 1 process does not give the expected results: the reason is unclear, and the analysis is still ongoing. In the same way, for the measurements reported in Figure 3.6a, above a certain width value the type 1 peak becomes undetectable also for the waveguide M2AG018. As a last remark, in Figure 3.6b we have analysed via simulation, for a given waveguide nominal structure – in this case, the one of the epitaxy M2AG019 –, the behaviour of the conversion efficiency with respect to the aluminium concentration of the core, which appears to be one of the most relevant parameters in this sense. In conclusion, we list in Table 3.2 the simulated and measured conversion efficiencies for our structures; note that the experimentally calculated values are affected by the uncertainty on the knowledge of the coupling coupling efficiency and of the losses and cavity effects, given the difficulty in precisely evaluating all the parameters on which they depend, as discussed so far.

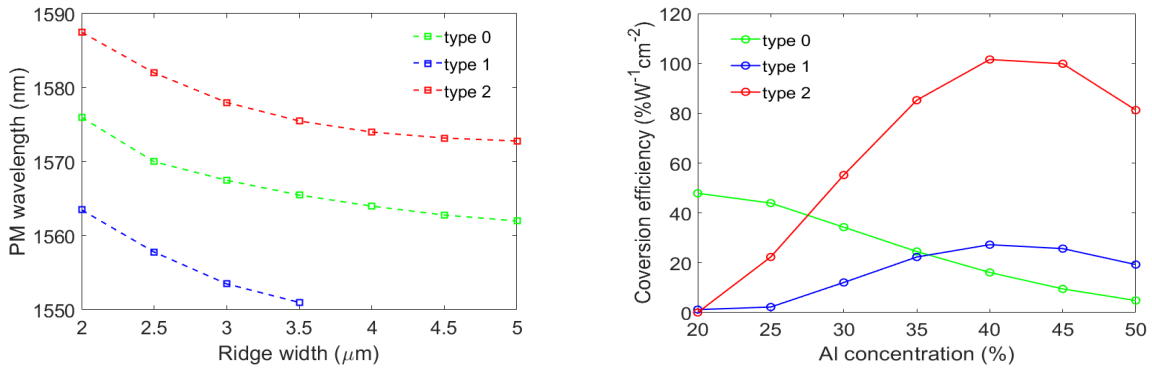

(a) (b)

Figure 3.6: (a) Experimental variation of the phase-matching wavelength ($2\lambda_{PM}$) with the waveguide's ridge width, for the three types of available phase-matching. Epitaxy M2AG018, dry etching, temperature 25°C. (b) Simulated variation of the conversion efficiency with the core Al concentration; nominal structure: M2AG019.

[3]In this way, we could have fine control on the ridge width, the parameter of interest, as explained in Section 2.2.3.

		Efficiency ($\%W^{-1}cm^{-2}$)		
Epitaxy	**Result**	**Type 0**	**Type 1**	**Type 2**
M2AG018	*Simulation*	62	3	29
	Experimental	60	2	42
M2AG019	*Simulation*	11	32	117
	Experimental	24	/	105

Table 3.2: Simulated and measured SHG efficiencies for the three types of available phase-matching.

3.3. Photon-pair production

Spontaneous parametric down-conversion is used to produce photon pairs with defined quantum properties: in this Section, we introduce the experimental setup implemented for the different available conversion processes, and we determine the performances of our sources, following what described in Section 1.3.3.

3.3.1. Experimental setup

Once the degeneracy wavelengths are identified through the SHG measurements, we can produce photon pairs via SPDC. The experimental setup is shown in Figure 3.7. The optical pump should be at λ_{PM}, so the CW laser is a tunable diode laser (*TOPTICA*, TM Photonics DL Pro 780) working in the red-NIR spectral region. The pump beam is polarized accordingly to the type of phase-matching process that we want to target[4] and coupled into the waveguide through the use of a microscope objective (63x, NA=0.90); the sample is always kept stable in temperature through the use of an external temperature controller. The light at the output of the guide (transmitted pump and produced pairs) is collected by another microscope objective (40x, NA=0.60). First a dichroic mirror and then a high-pass filter separate the residual pump beam from the photon pairs (extinction ratio for the pump around 10^{-12}), which are coupled into a single mode fiber (SMF28) via a fiber collimator.

In case of type 2 SPDC, the produced photons have orthogonal polarizations: they can be deterministically separated by a fibered polarization beam splitter (PBS). A fibered polarization controller (PC) is used to ensure to reach the maximum splitting ratio, compensating for the rotations of polarization occurring in the fiber. In case of type 0 or

[4]TM polarization for both type 0 and type 1, TE for type 2; check Sections 2.2.2 and 3.2.2.

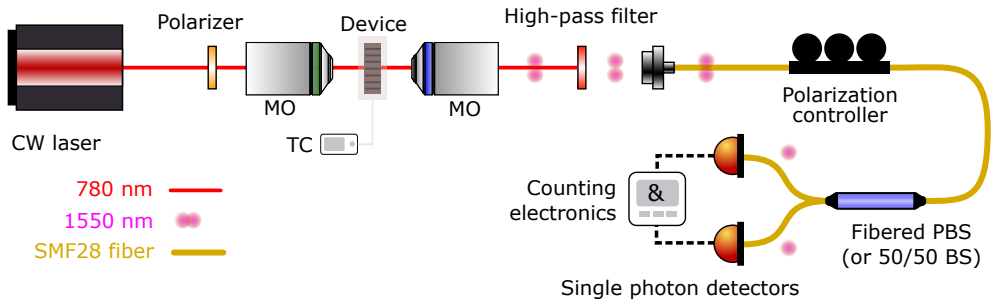

Figure 3.7: Scheme of the setup for the SPDC measurement. MO: microscope objective; TC: temperature controller.

type 1 SPDC, the produced photons have parallel polarizations: a 50/50 beam splitter (BS) is used to separate them; note that in this way the separation is not deterministic, so it is effective only for 50% of the pairs, causing half of the signal to be lost. Finally, the two photons are respectively detected with superconducting nanowire single photon detectors (SNSPD, *Quantum Opus*) featuring a 85% detection efficiency and $10s^{-1}$ dark count rate[5]. Those detectors are sensitive to the polarization of the photons: thus, we add a fibered PC in each arm of the (P)BS, to maximize the number of counted photons (or single counts, S). Back to photons produced via type 2 SPDC, the optimization of the splitting ratio is generally achieved by placing a TE or TM polarizer at the output of the collection objective, in order to select only one photon of the pair; the PC is then adjusted to annihilate the single counts of one of the two detectors, so to ensure the alignment of the polarizations of the photons with the optical axes of the PBS.

The electrical signals generated by the detectors upon the detection of a photon are fed into the TCSPC module (a time-to-digital converter – TDC –, *quTau*), counting the "start-stop" events within a time buffer of $4\mu s$. The coincidence histograms recorded for the three types of phase-matching are shown in Figure 3.8. Each time bin is 163ps large, corresponding to the temporal bin resolution set on the TDC; note that, even if the emission times of the photons of the pair are supposed to be perfectly correlated, the signal peak spans over few bins: this is caused by the finite timing jitter of both the detectors and the counting electronics. For this acquisition, we used the epitaxy M2AG019 and a waveguide of $3.2\mu m$ ridge width, kept at 26°C. The input optical power measured before the input objective was 25mW and the pump wavelength was set to the λ_{PM} value corresponding to each process. As expected, the most efficient frequency conversion is obtained for the type 2 PM, followed by the type 0; a weak type 1 signal is recorded as

[5]The dark counts are set by the bias current: typically, increasing the bias, the responsivity of the detectors is increased, as well as the dark count rate; there will be an optimal combination of the values of these quantities for the given application.

well, even if no SHG was detected for that process (see Figure 3.5b): this might come from the fact that the sensitivity of the coincidence measurement is higher, while the noise level is generally lower, being the signal in the IR range.

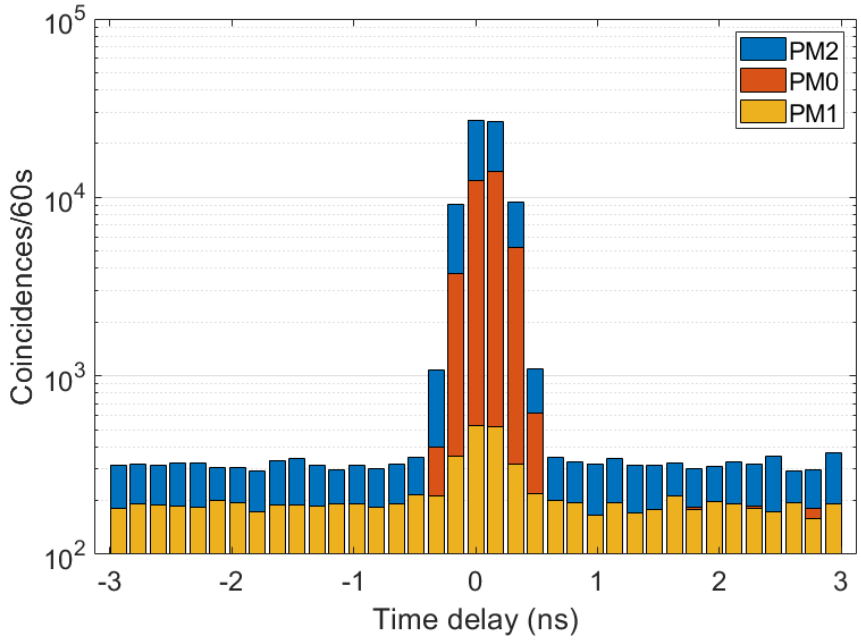

Figure 3.8: Histograms of coincidences for the three types of conversion processes. Epitaxy M2AG019, P_{IN}=25mW, T=26°C, ridge width 3.2μm, wet etching, integration time 60s, semi-logarithmic scale.

3.3.2. Source performances

On the recorded histogram of coincidences, we can define a *signal window* of width Δ_s containing the temporal bins corresponding to the SPDC process (in the case of Figure 3.8, $\Delta_s = 6$ bins), and a *noise window* of width Δ_n, usually set close enough to the coincidence peak, without including it. The number of counted events in the signal window within a given integration time Δt corresponds to the *raw* coincidence number, C_{raw}, while the ones falling in the noise window are the accidental counts, A. The accidental counts are normalized with respect to the signal window width, hence representing an average of the background noise: for this reason, we typically set $\Delta_n \gg \Delta_s$. The *net* number of coincidences is retrieved as:

$$C_{net} = C_{raw} - A\frac{\Delta_s}{\Delta_n}, \tag{3.9}$$

while the coincidence-to-accidental ratio as:

$$CAR = \frac{C_{net}}{A\frac{\Delta_s}{\Delta_n}} = \frac{C_{raw}\Delta_n}{A\Delta_s} - 1, \tag{3.10}$$

representing the experimental related version of Equations (1.36) and (1.37). We can therefore study the dependence of the coincidence rate and of the CAR on the input optical power (Figure 3.9a) and on the pump wavelength (Figure 3.9b), in order to find the best working conditions. The results presented here refer to the type 2 PM process for a 3.2μm wide waveguide from the epitaxy M2AG019. We retrieve that the coincidence rate is linearly dependent on the input power, while the CAR is inversely proportional to the pump power, as expected assuming a pumping regime for which double-pair emissions are negligible [65]. Excessively increasing the pump power not only reduces the CAR – and hence the quality of the signal –, but might also lead to damaging the sample, in particular the waveguide facets; for this reason, we keep the pump power measured before the input objective below 40mW. For what concerns the dependence on the pump wavelength, we note that both the coincidence rate and the CAR follow the (almost) same profile, peaked at the phase-matching wavelength, where the nonlinear conversion efficiency is maximized.

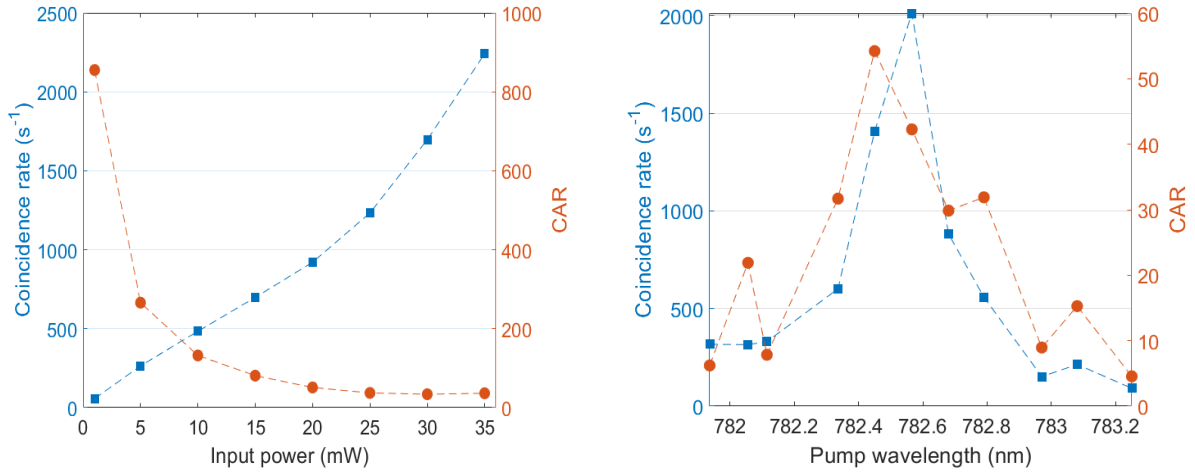

Figure 3.9: Coincidence rate and CAR as function of (a) the input pump power (with constant pump wavelength, 782.566nm) and of (b) the pump wavelength (with constant input pump power, 25mW). Epitaxy M2AG019, ridge width 3.2μm, type 2 PM process.

For a quantitative comparison with other available photon-pair sources, it is useful to evaluate the pair generation rate (R) and the source brightness (B), which are the per-

formance indicators independent from the particular adopted experimental setup. With reference to Equation (1.36), we have:

$$R = \frac{C_{net}}{\eta_s \eta_i}. \tag{3.11}$$

For the estimation of the combined collection/detection efficiencies η_s and η_i, we can exploit the knowledge on the single counts' rates:

$$\begin{cases} S_s = \eta_s R + d_s & \text{(3.12a)} \\ S_i = \eta_i R + d_i, & \text{(3.12b)} \end{cases}$$

where we have assumed that signal and idler are each always revealed by the same detector, whose dark counts are, respectively, d_s and d_i. By including Equation (3.11) in the system of equations (3.12), we can directly evaluate the three parameters of interest – R, η_s, η_i –, as done in [66]. In alternative, η_s and η_i can be estimated independently from the PGR by introducing a controllable attenuation before the beam splitter, as done in [53]. Therefore, we were able to retrieve $\eta_s = 10.4\%$ and $\eta_i = 10.6\%$; in Table 3.3, we list the best results obtained for the different epitaxies and phase-matching types of conversion processes. For the brightness calculation, we estimated the pump optical power confined into the waveguide to be 1mW, and the bandwidth to be 60nm for PM2 and 80nm for PM0 and PM1 processes (values coming from the numerical simulation of the JSA, as the one shown in Figure 2.12b).

Epitaxy	**PM type**	C_{net} **(s^{-1})**	R **(s^{-1})**	B **(s^{-1}mW^{-1}nm^{-1})**	**CAR**
M2AG018	**0**	5.2×10^3	4.7×10^5	5.9×10^3	26
	1	3.2×10^2	2.9×10^4	3.6×10^2	1.5
	2	2.9×10^3	2.6×10^5	4.4×10^3	15
M2AG019	**0**	8.5×10^3	7.7×10^5	9.6×10^3	34
	1	1.3×10^3	1.2×10^5	1.5×10^3	3.2
	2	2.5×10^4	2.3×10^6	3.8×10^4	78

Table 3.3: Measured net coincidence rate, PGR, brightness and CAR of the analysed sources, for the different phase-matching types of conversion processes.

With reference to the state of art peak performances reported in [33], our results are comparable with the ones of integrated sources with similar characteristics (high compactness and wide bandwidth signal). In addition, our source shows a great versatility in terms of available conversion processes within the telecom band: in this sense, the optimization of the type 1 phase-matching conversion process is a further important step for the

demonstration of hybrid devices.

3.4. Measurement of energy-time entanglement

In the framework of this master thesis work, we chose to characterize the quantum state of the produced photon pairs in terms of energy-time entanglement quality. This type of entanglement, as discussed in Section 1.2.4, is an intrinsic property of the pairs produced via an SPDC process stimulated by a narrowband optical pump, independently from the selected phase-matching type and, hence, from the resulting polarizations of the two photons. In addition, high quality energy-time entanglement can be successfully exploited in quantum information protocols, as well as, for example, the more historical polarization entanglement [67]. In this Section, we describe the design and characterization of a fibered interferometer realized during my master thesis, followed by the experimental results; moreover, we present a theoretical model that I have developed for explaining the correlation between the Franson's visibility and the spectral properties of the produced quantum state.

3.4.1. The Franson interferometer

In Section 1.2.4 we introduced the basic scheme of a Franson interferometer (see, in particular, Figure 1.4); in this scheme, for ensuring the indistinguishability between the paths ($s_A - s_B$ and $l_A - l_B$), it is assumed that the two unbalanced interferometers (A and B) are perfectly identical, meaning that the time differences between the two arms of each interferometer – respectively, ΔT_A and ΔT_B – are equivalent. In practice, this condition is met when $|\Delta T_A - \Delta T_B| \equiv \Delta\tau \ll \tau_c$, where τ_c is the coherence time of each photon of the pair. Therefore, the conditions to be fulfilled for the experiment can be summarized in the following expression:

$$\overbrace{\Delta\tau \ll \underbrace{\tau_c}_{I}, \tau_{jit} \ll \overbrace{\Delta T}^{III}}^{II} \ll \tau_p, \tag{3.13}$$

where:

I. τ_c is typically of the order of few picoseconds, meaning that the precision required for the knowledge of the differences in optical paths between the two interferometers is of the order of few tens of micrometers[6]. This precision is not easily achieved,

[6] Assuming $\tau_c \simeq 1$ps, the corresponding difference in optical path Δl should respect $\Delta l \ll c\tau_c/n_{eff} \simeq 200\mu$m, where n_{eff} is the effective index of the fundamental mode propagating into the interferometer

especially for self-made instruments; a possible solution is to adopt the so-called *folded* configuration [68], in which both photons are sent to the same unbalanced interferometer, doubled by the use of a mirror at the end of each path, so that the mismatch between the two interferometers is in principle avoided.

II. In the folded configuration, $\Delta T = 2\Delta L n_{eff}/c$ is the actual difference between the two arms of the interferometer, being ΔL the difference in optical path and n_{eff} the effective refractive index. Not only we require this difference to be much larger than τ_c in order to avoid single-photon interference, but also much larger than the combined jitter of the detector and of the counting electronics, τ_{jit}, amounting to around 500ps; this is necessary to be able to experimentally distinguish the non-interfering path combinations ($s_A - l_B$ and $l_A - s_B$). Thus, in practice, the minimum interferometer size is defined by τ_{jit}, since $\tau_{jit} \gg \tau_c$. In our interferometer, we set $\Delta L = 54$cm, corresponding to $\Delta T = 5.2$ns.

III. The time at which either photon is emitted is initially uncertain over a time interval corresponding to the coherence time of the pump beam[7], τ_p. In order to have two-photon interference, this coherence time must be much larger than ΔT. For this reason, we use a narrow-band laser (*TOPTICA*, TM Photonics DL Pro 780) with $\tau_p > 1\mu$s as pumping source, satisfying the required condition.

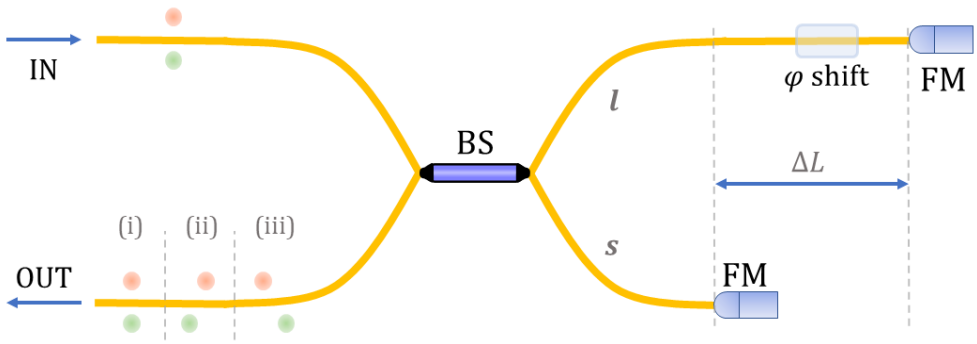

Figure 3.10: Scheme of the fibered Franson interferometer in the folded configuration. BS: 50/50 beam splitter, FM: Faraday mirror, l: long arm, s: short arm.

A scheme of the resulting structure is shown in Figure 1.4. The choice of realizing a fibered interferometer introduces several advantages, such as compactness, easy connection with

(here we took the one of telecom light in a single mode optical fiber).

[7] In the original article [11], Franson considers a three-level atomic system – upper state ψ_1, middle state ψ_2, ground state ψ_0 – in which the lifetime of ψ_1, τ_1, is much larger than the one of ψ_2, τ_2. In this way, the two photons (one generated by the trasmission $\psi_1 \to \psi_2$, the other by $\psi_2 \to \psi_0$) are emitted at times which are the same to within a small uncertainty τ_2, but the time at which either photon is emitted is initially uncertain over a much larger time interval τ_1. In our case, τ_c corresponds to τ_2 while τ_p corresponds to τ_1.

the existent telecom components, easy implementation of the phase control, possibility to move the instrument to other experiments and use it in a plug-and-play fashion. However, on the other hand, it introduces new problems to cope with, especially phase drifts due to birefringence and thermal instability, and the chromatic dispersion, which will be discussed in detail in the next Section.

Birefringence compensation

In single-mode fibers the polarization of light rotates during the propagation[8]: it is possible, for example, to change the polarization state by simply bending the fiber. In addition, for non perfectly circular symmetric fibers – as it is usually the case, also due to asymmetric bendings in the fiber disposition –, birefringence contributions arise, meaning that the field mode will experience a different effective refractive index according to its specific polarization. Consider now the two photons generated by SPDC entering the beam splitter, and consider only the outcomes corresponding to both of them taking the same path. The rotations of the polarization will not, in general, be the same for the l and for the s arms, introducing a certain degree of distinguishability between the state $|s\rangle|s\rangle$ and the state $|l\rangle|l\rangle$. This degree is even increased in the case of orthogonal photons produced by a type 2 phase-matching conversion process, for which stronger birefringence effects add up. The non-perfect indistinguishability affects the state of the quantum superposition, resulting in a reduction of the quantum interference visibility.

To compensate for all these effects, we introduce in the setup two (fibered) Faraday mirrors (FM, *ThorLabs*). Those mirrors not only reflect light, but also rotate the input polarization of the field by 90°. It is at this point useful to perform the detailed calculation to demonstrate the role of these optical components in compensating for the birefringence and for the rotations of polarization. To do this, we will make use of the Jones formalism [69], where polarization states in the transverse plane are described by two-element vectors and transformations occurring during the propagation by 2×2 unitary matrices[9]. Assume

[8] This is not the case for polarization maintaining fibers, where these rotations are avoided or at least strongly attenuated; however, other components, such as fiber connectors and mirrors, might introduce unwanted contributions in this sense.

[9] For example, $\begin{pmatrix}1\\0\end{pmatrix}$ represents a horizontally polarized mode, while $\begin{pmatrix}0\\1\end{pmatrix}$ a vertically polarized one; the matrix for the propagation in vacuum is the identity matrix, $I = \begin{pmatrix}1 & 0\\0 & 1\end{pmatrix}$, since no trasformation occurs during the propagation.

that the state of one photon of the pair is described by the generic vector:

$$\mathbf{V} = \begin{pmatrix} u \\ v \end{pmatrix}, \tag{3.14}$$

and the trasformations occurring during the forward propagation – from the BS to the mirrors – in one of the arms by the generic matrix:

$$M = \begin{pmatrix} A & B \\ C & D \end{pmatrix}; \tag{3.15}$$

further assuming that no significant alteration in the fiber occurs between the way in and the way back and that the propagation losses are negligible[10], the transformations for the backward propagation – from the mirrors to the BS – can be described by the transpose of M, M^T, with $M^T M = I$, where I is the identity matrix. The effect of the FM is to rotate the polarization by 90°, so that it can be described by the rotation matrix:

$$R_{FM} = \begin{pmatrix} 0 & -1 \\ 1 & 0 \end{pmatrix}. \tag{3.16}$$

The polarization state $\mathbf{V}'$ after the overall propagation, so when the photon returns back to the BS, will be then:

$$\mathbf{V}' = M^T R_{FM} M \mathbf{V} = \alpha \begin{pmatrix} v \\ -u \end{pmatrix}, \tag{3.17}$$

being α the determinant of M, equal to one. Note that $\mathbf{V} \cdot \mathbf{V}' = 0$: the two vectors are perpendicular. The same reasoning could be applied to the other photon of the pair, and independently from the particular M matrix[11]: therefore, the Faraday mirrors compensate for any birefringence effect and conserve the relative orientation between the polarizations of the two photons after the propagation through the arms of the interferometer. For a common mirror, the rotation matrix is:

$$R_M = \begin{pmatrix} 1 & 0 \\ 0 & -1 \end{pmatrix}; \tag{3.18}$$

[10] The first assumption is reasonable considering the very small amount of time required for the propagation (in our case, around 2.6ns); the second assumption is justified by the fact that in optical fibers in the telecom range losses are typically <0.2dB/km, leading to negligible losses for a propagation length of few meters.

[11] If the photons' polarizations are parallel, we have different M matrices according to the interferometer arm: M_l and M_s; if the photons' polarizations are perpendicular, we have different M matrices even within the same arm, due to birefringence: $M_{i,H}$ and $M_{i,V}$, with $i \in (s, l)$. The Faraday mirrors compensate for the action of any M matrix.

one can easily see that, when doing the calculation in Equation (3.17) with R_M in place of R_{FM}, no compensation is achieved, demonstrating the necessity of the Faraday mirrors.

The action of the Faraday mirrors can be tested with a fully classical interference experiment: a linearly polarized laser beam is sent through the BS, which will equally split the beam between the arms. With normal mirrors, the polarization rotation and the birefringence experienced in each arm will be in general different: when arriving back to the BS, the fields will not be projected along the same direction, resulting in an attenuated interference. Hence, when changing the phase φ, the interferogram will show a contrast lower than 1. On the other hand, if the FMs are implemented in the setup, the expected contrast for this kind of experiment is 1, since the two backward propagating fields arrive at the BS with the same polarization. This step is part of the classical characterization of the interferometer.

Thermal stability

The refractive index of a material depends on the temperature: local variations of temperature in the interferometer will change the index, and consequently the optical path, introducing an additional phase term. In practice, as will be detailed in the following, when performing an interference measurement, we record a certain number of acquisitions, n_{acq}, corresponding to different values for the phase φ; for each acquisition, we set an integration time Δt_{int}. The total measurement time, Δt_{meas}, will be $n_{acq} \times \Delta t_{int}$. To avoid thermal drifts during the measurement time Δt_{meas}, we need to have $\Delta t_{meas} \ll \Delta t_{th}$, where Δt_{th} is the temporal scale over which the thermal phase drift leads to a full oscillation in the interferogram.

We can evaluate the order of magnitude of the maximal allowed temperature variation, ΔT, should be limited, in order to satisfy the latter equation. If we consider a thermo-optic coefficient[12], α_{th}, of around $10^{-5}\mathrm{K}^{-1}$ for the fiber [70] and that the maximum acceptable thermal phase drift, $\Delta\phi_{th}$, is smaller than $2\pi/50$ rad (corresponding to a reduction of quantum visibility is smaller than 0.5% [71]), the phase and temperature variations are related by:

$$\Delta\phi_{th} = 2\pi \frac{L}{n_{eff}\lambda} \alpha_{th} \Delta T, \tag{3.19}$$

where $L = 2\Delta L$ is the the difference in propagation length where thermal variations are not compensated (assuming homogeneous thermal variations within the system). We deduce that the variation in temperature should be smaller than 5mK. Assuming a mea-

[12]The thermo-optic coefficient, expressed as $\mathrm{d}n_{eff}/\mathrm{d}T$, gives the linearized variation of the refractive index with respect to the temperature T in a given spectral range: $\Delta n_{eff} = \alpha_{th}\Delta T$.

surement time for the whole energy-time entanglement experiment of the order of one hour, the required thermal stability is $\lesssim 10^{-3}$mK/s. To achieve such stabilization, a first step is to dispose the interferometer onto a massive (high thermal inertia) metallic (good thermal conductivity) platform; then, a multi-layer thermal isolation is implemented, inserting the device in a thick polystyrene box, surrounded by a thermal isolating bag. The whole object is preferably kept in an environment with stabilized temperature. A temperature sensor is placed in the centre of the platform, and thermo-resistors are placed below it. Now, the stabilization can be reached either in a passive or in an active way: the passive method consists of letting the box thermalize for a long time; if the isolation is good enough, this will provide enough stability for the experiments. The active method consists of connecting the sensor to the input of a PID thermal controller (sensitivity 1mK), whose output controls the thermo-resistors. Experimentally, we obtained a better stabilization with the first method, probably due to the fact that our requirements are very close to the thermal controller sensitivity, so that the heating or cooling action is actually detrimental.

The stability characterization can be performed through a classical interference experiment, as done in [72]: a linearly polarized laser beam is sent to the BS and the optical power exiting the interferometer is collected and measured. If φ is kept stable, the resulting interference pattern will be set by thermal phase drift ϕ_{th}. By integrating for very long times – typically, several days –, we can determine Δt_{th} by looking at the oscillations' period. In Figure 3.11 we can see the stability growing during the thermalization. In particular, we where able to reach up to 3 hours of stability with the active method, and up to 10 hours with the passive one.

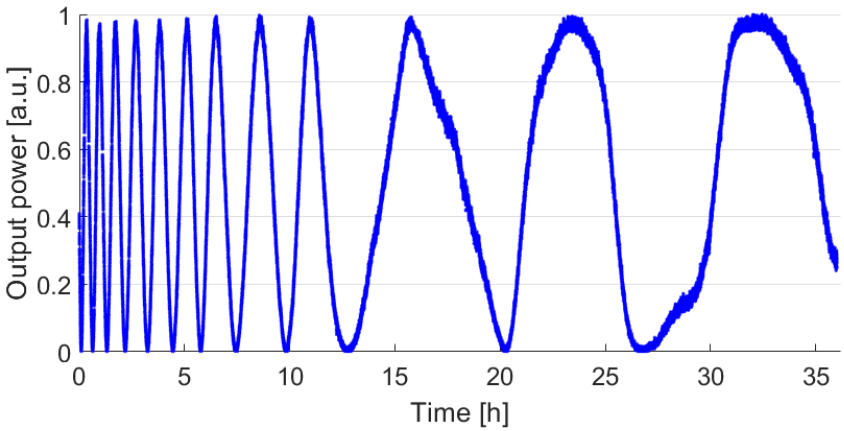

Figure 3.11: Classical interference experiment for the characterization of the thermal stability of the Franson interferometer.

Several hours of thermal stability still mean a limitation in the measurement time. To overcome such limit, an approach based on the active phase compensation – instead of active temperature stabilization – can be implemented. In practice, a reference narrow-band laser (coherence length much larger than ΔL) is sent into the interferometer, and it is used to reconstruct the value of the thermal phase drift in real time. This information is fed into a feedback loop, which sets the value of φ in order to have the target phase. In this way, no thermal isolation or stabilization is required, and the only limitation is the response time of the electronics involved in the feedback loop, which is typically of the order of 1ms, usually much lower than Δt_{int}. This approach has been successfully implemented in [71] and [73], representing an attractive perspective also for the next development of our interferometer.

Setup for the measurements

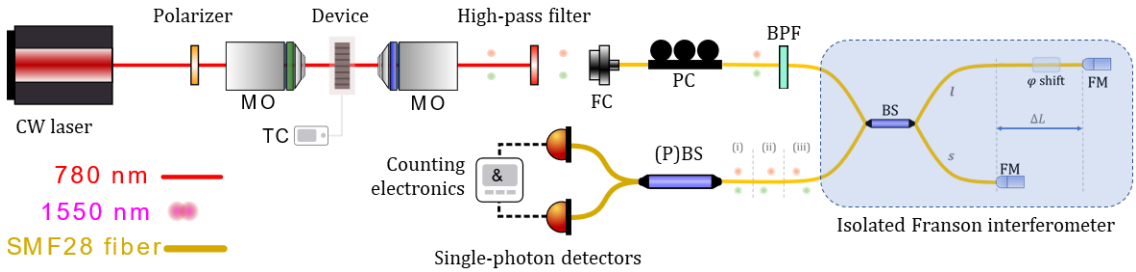

Figure 3.12: Scheme of the setup for the Franson interferometry measurement. MO: microscope objective, TC: temeperature controller, FC: fiber collimator, (P)BS: (polarization) beam splitter, PC: polarization controller, FM: Faraday mirror, BPF: band-pass filter.

Figure 3.12 presents the whole measurement setup for a Franson experiment. Up to the polarization controller, it is the same setup as for the SPDC generation measurement (see Section 3.3.1); the role of the band-pass filter (BPF) will be clarifired in Section 3.4.2. Then, pairs are sent into the thermally isolated Franson interferometer. The output signal is collected and separated by either a polarization beam splitter (in case of type 2 phase-matching SPDC) or a 50/50 beam splitter (in case of type 0 or 1 PM), in order to perform a coincidence measurement and record the coincidence histogram. Note that if the condition *II* introduced at the beginning of this Section is met, we can experimentally separate the case in which both the photons of the pair take the same path (both l or both s, case (i) in the Figure – see also Figure 3.10 for better resolution) from the ones in which they take different paths (cases (ii) and (iii)). The result will be a coincidence histogram with three well separated peaks: we can thus post-select only the central one,

corresponding to the quantum superposition state, and measure the interference pattern as a function of the phase φ, as described in Section 1.2.4.

The phase is varied through the use of a piezoelectric fiber stretcher (*Idil*): depending on the voltage across the stretcher, a different optical delay (or, equivalently, a different phase) is introduced in the pathway. A micro-controller is used to set the voltage and to keep it stable for the given integration time; the combined response time of the micro-controller and the stretcher is of the order of 1ms. For each acquisition, hence for each value of the phase, the coincidence histogram is recorded. A typical result is shown in Figure 3.13. We can see how the two lateral peaks, also called *satellite* peaks, are not affected by the phase changes, as expected; they are separated from the central one by a delay of around 5.2ns, corresponding to twice the length difference (ΔL) between the two arms of the interferometer. The central peak, corresponding to the quantum superposition between the two states $|s\rangle|s\rangle$ and $|l\rangle|l\rangle$, displays the expected interference pattern and can be extinguished for particular values of the phase. The quantitative analysis of these results is presented in Section 3.4.3.

3.4.2. Bandwidth, dispersion and quantum visibility

Optical fibers are characterized by chromatic dispersion, meaning that the effective refractive index changes with the wavelength; within our band of interest, this variations is low ($\mathrm{d}n/\mathrm{d}\lambda|_{1550\mathrm{nm}} \simeq -0.0012\mu\mathrm{m}^{-1}$, from [70]), but not null. Consider a pair of photons, at frequencies ω_s and ω_i such that $\omega_s + \omega_i = \omega_p$ for energy conservation, being ω_p the pump frequency, generated by SPDC: the narrow-band pump makes the frequencies of the two photons to be strongly anti-correlated, symmetric with respect to $\omega_p/2$. The JSA of the generated state determines the probability to generate the particular photon-pair with frequencies (ω_s, ω_i), as discussed in Section 2.3.2. Therefore, except for the perfectly degenerate case ($\omega_s = \omega_i = \omega_p/2$), we will have a *blue* – the one with higher frequency – and a *red* – the one with lower frequency – photon. Due to the chromatic dispersion, they will experience a different refractive index value in the fiber: as a consequence, the red photon will travel faster than the blue. When entering the Franson interferometer, during the propagation through the unbalanced part (ΔL, back and forth), the blue photon will acquire an additional delay with respect to the one acquired through the s arm: this introduces a degree of distinguishability between the $|s_s\rangle|s_i\rangle$ and $|l_s\rangle|l_i\rangle$ states[13], where s and i refer to the photons of the pair, thus affecting the entanglement visibility. The

[13]Note that any dispersion contribution acquired before or after the interferometer, or within the s arm and a portion of length $(l - \Delta L)$ in the l arm, will not introduce any distinguishability, but will only eventually shift the three peaks of the coincidence histogram.

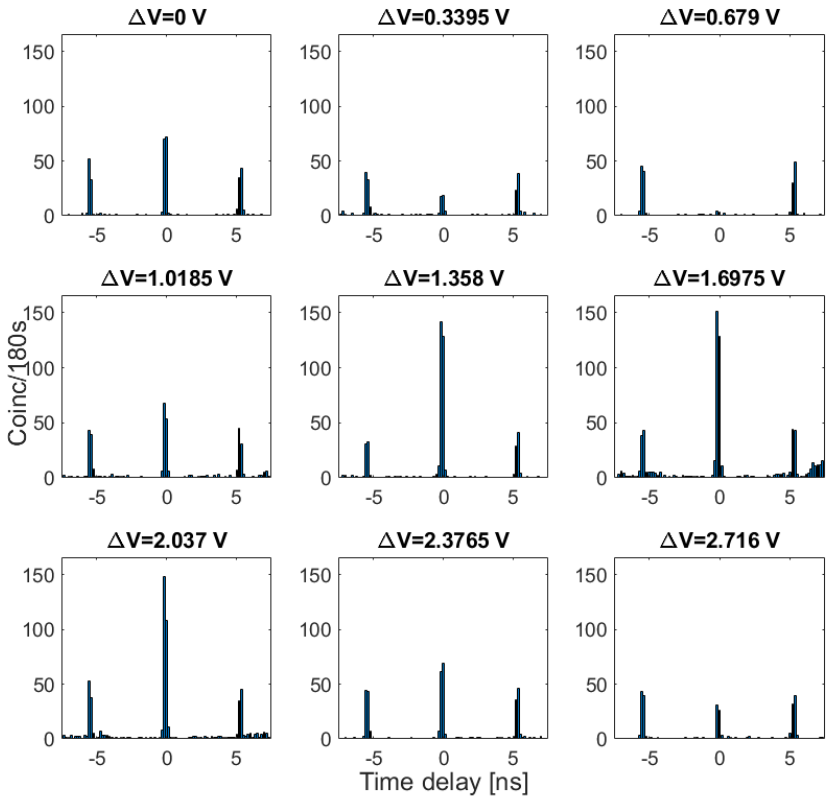

Figure 3.13: Recorder histograms of coincidences for a Franson experiment: ΔV is the voltage set across the piezoelectric fiber stretcher, so that to each voltage value corresponds a certain phase value φ.

amount of the delay can be estimated, at first order, as:

$$\Delta t_D = \frac{2\Delta L}{c} \left.\frac{\mathrm{d}n}{\mathrm{d}\lambda}\right|_{1550\mathrm{nm}} \Delta\lambda, \tag{3.20}$$

where $\Delta\lambda = |\lambda_s - \lambda_i|$ is the wavelength difference between the two photons. Assuming $\Delta\lambda \sim 100$nm, we get $\Delta t_D \simeq 450$fs, which is much smaller than the time resolution of our detectors (163ps): the photons will continue to fall in the central peak of the histogram, but the visibility of the interference pattern, so the entanglement visibility, will be reduced.

To quantitatively predict the effect of the chromatic dispersion on the entanglement visibility, given the JSA of the input SPDC signal, we performed the calculation for the propagation of the quantum state through the interferometer. We refer to the scheme in Figure 3.14 for a better following of the steps of the calculus; note that the effect of the Faraday mirrors is here schematized by duplicating the path, with the additional

condition of no birefringence contributions.

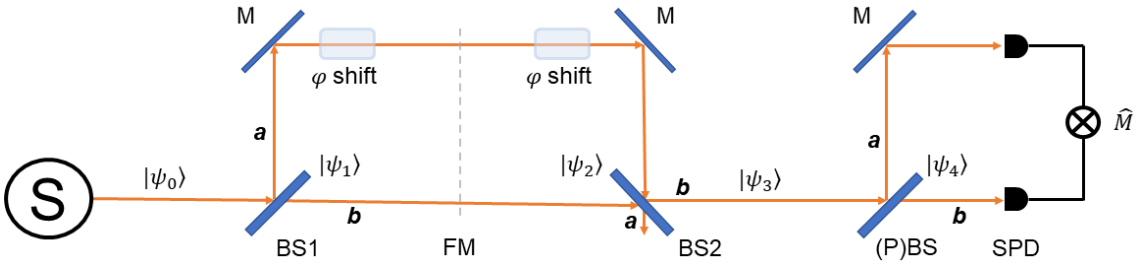

Figure 3.14: Scheme for the detailed calculus of the quantum state propagation through the Franson interferometer. ***a*** and ***b*** are the spatial modes. S: source, M: mirror, (P)BS: (polarization) beam splitter, SPD: single photon detector.

The state produced by the source is the one of Equation (2.19), which can be rewritten as:

$$|\psi_0\rangle = \iint \mathrm{d}\omega_S \mathrm{d}\omega_I C(\omega_S, \omega_I)|S, \omega_S\rangle|I, \omega_I\rangle, \tag{3.21}$$

where we made the substitutions $s \to S$ and $i \to I$ to avoid confusion with the imaginary unit, and we have assumed for the sake of simplicity that the JSA only depends on the photons' frequencies[14]. The effect of BS1 is:

$$\begin{cases} |S\rangle \to \dfrac{1}{\sqrt{2}}(i|a_S\rangle + |b_S\rangle) & \text{(3.22a)} \\ |I\rangle \to \dfrac{1}{\sqrt{2}}(i|a_I\rangle + |b_I\rangle), & \text{(3.22b)} \end{cases}$$

where a and b are the available spatial modes, corresponding to the arms of the interferometer, and $|a_S\rangle$ represents the presence of a signal photon at frequency ω_S in the spatial mode a – the corresponding notation holds for all the other combinations. Hence, the state just after BS1 is:

$$|\psi_1\rangle = \frac{1}{2}\iint \mathrm{d}\omega_S \mathrm{d}\omega_I C(\omega_S, \omega_I)(i|a_S\rangle + |b_S\rangle)(i|a_I\rangle + |b_I\rangle). \tag{3.23}$$

When propagating through the interferometer arms, considering only phase terms and

[14]In reality, this is true only for photon pairs produced by type 0 and type 1 phase-matching conversion processes. For type 2 photon pairs, birefringence effects will add up (see Section 2.3.3) and we will have a different JSA: in particular, $C_{H,V}(\omega_s, \omega_i) \neq C_{V,H}(\omega_s, \omega_i)$, where H and V refer to the polarization of signal and idler, respectively.

neglecting the losses, we have:

$$\begin{cases} |a_S\rangle \to e^{-i\omega_S t_a^S}|a_S\rangle, |a_I\rangle \to e^{-i\omega_I t_a^I}|a_I\rangle & \text{(3.24a)} \\ |b_S\rangle \to e^{-i\omega_S t_b^S}|b_S\rangle, |b_I\rangle \to e^{-i\omega_I t_b^I}|b_I\rangle, & \text{(3.24b)} \end{cases}$$

where t_a, b^j, with $j \in (S, I)$, is the propagation time of the photon j in the given arm of the interferometer and τ_j is the delay acquired in the unbalanced part of the interferometer, set by the delay line (ΔL) and by the phase control (φ), so that $t_a^j = t_b^j + \tau_j$. Note that, due to the chromatic dispersion, all these times are different. Therefore, the state just before the BS2 is:

$$|\psi_2\rangle = \frac{1}{2}\iint \mathrm{d}\omega_S \mathrm{d}\omega_I C(\omega_S, \omega_I) e^{-i\omega_S t_b^S} e^{-i\omega_I t_b^I} \times \left[-|a_S\rangle|a_I\rangle e^{-i(\omega_S\tau_S + \omega_I\tau_I)} + \underbrace{i|a_S\rangle|b_I\rangle e^{-i\omega_S\tau_S}}_{(i)} + \underbrace{i|b_S\rangle|a_I\rangle e^{-i\omega_I\tau_I}}_{(ii)} + |b_S\rangle|b_I\rangle \right]. \tag{3.25}$$

The terms (i) and (ii) represent the case in which signal and idler take different paths: since we have imposed that $\tau_c \ll \tau_S, \tau_I$, no interference will occur from these terms and they will correspond to the satellite peaks in the coincidence histogram. Therefore, we can neglect them from now on. The effect of BS2 is described by:

$$\begin{cases} |a_j\rangle \to \frac{1}{\sqrt{2}}(|a_j\rangle + i|b_j\rangle) & \text{(3.26a)} \\ |b_j\rangle \to \frac{1}{\sqrt{2}}(i|a_j\rangle + |b_j\rangle), & \text{(3.26b)} \end{cases}$$

with $j \in (S, I)$. We apply these transformations to the state $|\psi_2\rangle$ and we select the cases in which both photons take the spatial mode b, in the detection stage. This introduces a further loss of signal, which is reduced by a factor 4: in fact, we lose the cases in which the two photons are split in different paths or in which they both take the spatial mode a. To avoid this loss, one could implement a Franson folded interferometer where, instead of having a 2×2 beam splitter, we use an optical circulator combined with a 1×2 beam

splitter. Hence, the state $|\psi_3\rangle$ becomes:

$$|\psi_3\rangle = \frac{1}{2}\iint \mathrm{d}\omega_S \mathrm{d}\omega_I C(\omega_S,\omega_I) e^{-i(\omega_S t_b^S + \omega_I t_b^I)} |b_S\rangle |b_I\rangle e^{-i\frac{\omega_S\tau_S+\omega_I\tau_I}{2}} \cos\left(\frac{\omega_S\tau_S+\omega_I\tau_I}{2}\right), \tag{3.27}$$

where we have used the equivalence $(e^{ix}+e^{-ix})/2 = \cos(x)$. Now, if the pair is produced by a type 2 PM conversion process, the two photon polarizations are orthogonal and we can use a polarization beam splitter to separate them in a deterministic way[15], without loss of signal. In case of photons having parallel linear polarizations, we need to use a 50/50 beam splitter, introducing 50% of losses. Let us consider this latter case: the effect of the beam splitter is the same as BS1 in Equation (3.22) and we will only consider the cases in which the photons take different paths, corresponding to coincidence events. Thus:

$$\begin{aligned} |\psi_4\rangle = \frac{1}{4}\iint \mathrm{d}\omega_S \mathrm{d}\omega_I C(\omega_S,\omega_I) e^{-i(\omega_S t_b^S + \omega_I t_b^I)} \\ \times i(|a_S\rangle|b_I\rangle + |a_I\rangle|b_S\rangle) e^{-i\frac{\omega_S\tau_S+\omega_I\tau_I}{2}} \cos\left(\frac{\omega_S\tau_S+\omega_I\tau_I}{2}\right). \end{aligned} \tag{3.28}$$

We can associate an operator, $\hat{M}$, to the coincidence measurement [74]:

$$\hat{M} = \int \mathrm{d}\omega_a \hat{a}^\dagger(\omega_a)|0_a\rangle\langle 0_a|\hat{a}(\omega_a) \int \mathrm{d}\omega_b \hat{b}^\dagger(\omega_b)|0_b\rangle\langle 0_b|\hat{b}(\omega_b), \tag{3.29}$$

where $\hat{x}^\dagger(\omega_x)$ and $\hat{x}(\omega_x)$ are the operators describing the creation or annihilation of a photon at frequency ω_x in the spatial mode x, with $x \in (a,b)$. Finally, the normalized[16] coincidence probability will be:

$$\begin{aligned} P_{a,b}(\tau_S,\tau_I) &= \langle\psi_4|\hat{M}|\psi_4\rangle \\ &= \frac{1}{2}\iint \mathrm{d}\omega_S \mathrm{d}\omega_I |C(\omega_S,\omega_I)|^2 \left[1+\cos(\omega_S\tau_S+\omega_I\tau_I)\right]. \end{aligned} \tag{3.30}$$

As expected, the coincidence probability only depends on the delay acquired in the unbalanced part of the interferometer. If no chromatic dispersion is experienced, then we can write $\tau_S = \tau_I = \tau$; note that, in this case, $\cos(\omega_S\tau_S+\omega_I\tau_I) = \cos[(\omega_S+\omega_I)\tau] = \cos(\omega_p\tau)$.

[15] The role of the polarization controller before the input of the Franson interferometer (see Figure 3.12) is to maximize the splitting ratio.

[16] The factor before the integral is not important at this point, since we are interested in the visibility of the contrast. What is relevant from an experimental point of view is that we expect the coincidences collected in the central peak to be reduced by up to a factor 8 with respect to the coincidences measured without passing through the Franson interferometer, for what said so far.

Therefore, the term in square brackets can be taken out from the integral, since the pump frequency is constant: the visibility contrast will be, in this case, 100%. When considering the chromatic dispersion, it is useful to express the phase delays in terms of the known parameters and of the refractive index; in particular, we want to highlight the dependence of τ_S and τ_I on frequency and the voltage across the piezoelectric fiber stretcher. Thus:

$$\begin{cases} \omega_S \tau_S(\omega_S, \Delta V) = 2\left[\Delta L + \Delta L_{pz}(\Delta V)\right] \dfrac{\omega_S}{c} n(\omega_S) & \text{(3.31a)} \\ \omega_I \tau_I(\omega_I, \Delta V) = 2\left[\Delta L + \Delta L_{pz}(\Delta V)\right] \dfrac{\omega_I}{c} n(\omega_I), & \text{(3.31b)} \end{cases}$$

where $\Delta L_{pz}(\Delta V)$ is the length difference introduced by the fiber stretcher when the voltage is set to ΔV. Therefore, Equation (3.30) turns into:

$$\begin{aligned} P_{a,b}(\Delta V) = \frac{1}{2} + \frac{1}{2} \iint \mathrm{d}\omega_S \mathrm{d}\omega_I |C(\omega_S, \omega_I)|^2 \\ \times \cos\left[2\frac{\Delta L + \Delta L_{pz}(\Delta V)}{c}(\omega_S n(\omega_S) + \omega_I n(\omega_I))\right], \end{aligned} \tag{3.32}$$

where we have exploited the fact that the JSA is normalized. For simplicity, we can also consider the phase shift, $\varphi(\Delta V)$, introduced by the fiber stretcher to be independent from the frequency, so that the argument of the cosine becomes:

$$2\frac{\Delta L}{c}\left[\omega_S n(\omega_S) + \omega_I n(\omega_I)\right] + 2\varphi(\Delta V). \tag{3.33}$$

At this point we are able to simulate the effect of the chromatic dispersion on the entanglement visibility. We consider a Gaussian JSA centered at $\omega_p/2$ with FWHM of 80nm, which is a good approximation of the joint spectrum of our biphoton state, especially for the type 0 and type 1 phase-matching processes. We calculated the expected visibility for different values of ΔL, including the one adopted for our interferometer (54cm). Furthermore, we have investigated the effect of a rectangular spectral filter on the generated signal, centered at $\omega_p/2$: if $f(\omega_S, \omega_I)$ is the spectral transmission function of the filter, in Equation (3.32) we need to substitute $|C(\omega_S, \omega_I)|^2$ with $f(\omega_S, \omega_I) \times |C(\omega_S, \omega_I)|^2$; the visibility is then studied as a function of the bandwidth of this filter. The refractive index dispersion is taken into account by using the Sellmeier relations with the parameters taken from [75] for a temperature of 20°C. The result is displayed in Figure 3.15. The narrower the filter bandwidth, the higher the visibility: the effect of the chromatic dispersion will become more and more negligible as the photons get closer in frequency. The effect is stronger for larger ΔL: this is due to the fact that the more the photons travel in the unbalanced part, the larger is the delay acquired between them. However, ΔL cannot be

arbitrarily reduced: it is always limited by the conditions discussed at the beginning of this Section.

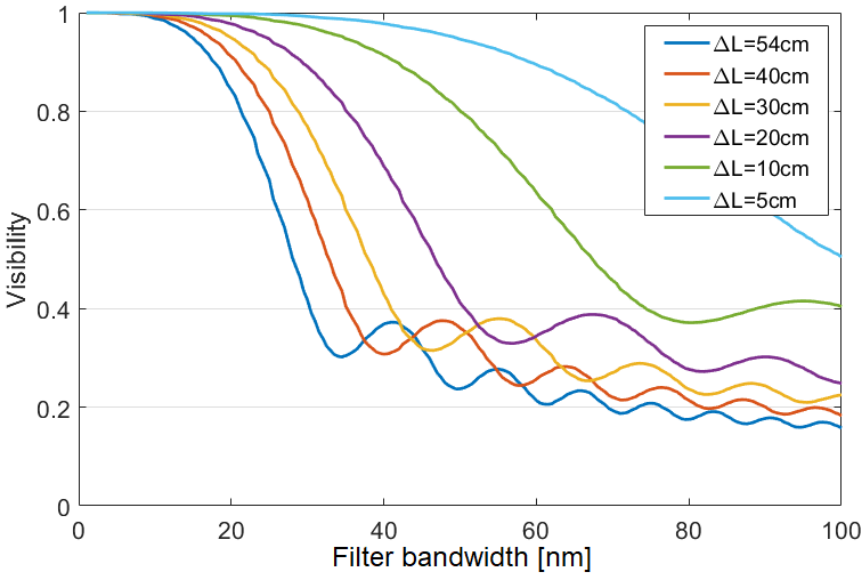

Figure 3.15: Simulated visibility for a Franson measurement, as a function of the interferometer unbalance ΔL and of the spectral filter bandwidth, assuming a pump wavelength of 780nm and a Gaussian JSA centered at $\omega_p/2$ with FWHM of 80nm.

The chromatic dispersion can be compensated by acting on the interferometer. A local cancellation can be achieved by replacing a portion of length ΔL of the long arm with a low-dispersion optical fiber: in this way, the effect of dispersion can be strongly reduced within the bandwidth of interest. Another solution, proposed by Franson [76], is the non-local cancellation of the dispersion. It can be implemented only in the original non-folded scheme (see Figure 1.4) and it consists of introducing an inversely dispersive medium in one of the interferometers, such that the dispersion experienced in one interferometer is the opposite of the one in the other. The demonstrated efficacy of this method resides into the true non-locality of the quantum entanglement, echoing the essence of the Einstein-Podolsky-Rosen paradox [9]. Both the local and non-local dispersion cancellations were demonstrated in [77] and it might represent a further upgrade also for our systems.

3.4.3. Experimental results

Considering the discussion in 3.4.2, we add a tunable – both in bandwidth and central wavelength – rectangular band-pass filter (BPF) to the measurement setup, as shown in Figure 3.12. For each type of available phase-matching conversion process (type 0 and type 2 in our case), we perform a series of measurements, with different filter bandwidth values.

The coincidence rate decreases with the bandwidth[17]: we compensate by increasing the integration time Δt_{int} per each acquisition, in order to keep a signal-to-noise ratio (we recall that the Poissonian noise associated to the detection event [78], grows as $\sqrt{N}$, where N is the total number of collected pairs in the central peak). Since the overall acquisition time is limited by the thermal stability, we limit the number of acquisitions, n_{acq}, to 20, to fully resolve around two oscillation periods of the interference pattern, with a resolution of 8/9 points per period. In this way, we keep the overall measurement time, $\Delta t_{meas} = n_{acq} \times \Delta t_{int}$, below one hour. For the results shown in the following, we used the epitaxy M2AG019, given the better performances in terms of pairs' production (see Table 3.3).

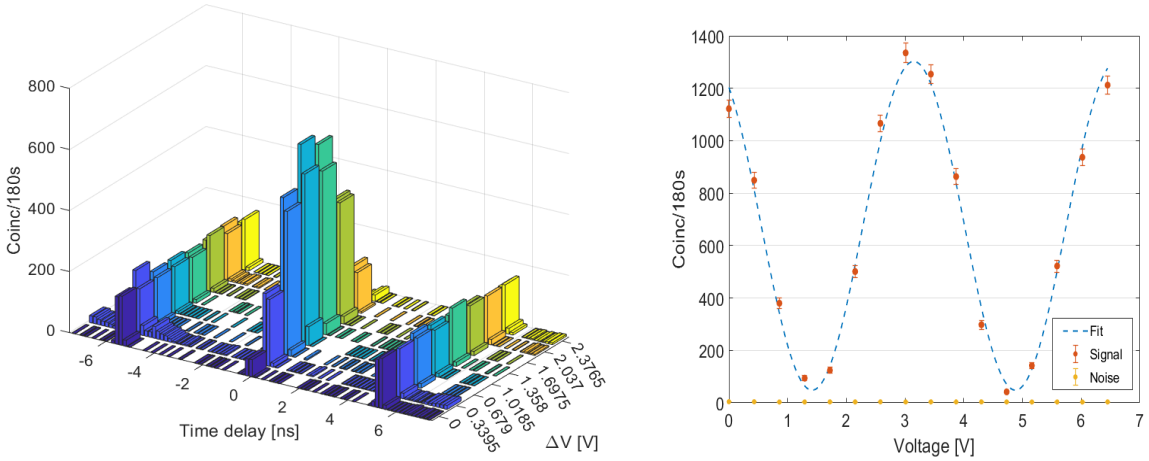

(a) (b)

Figure 3.16: (a) Histograms of coincidences for a full oscillation period, as a function of the voltage across the piezoelectric fiber stretcher ΔV and of the arrival time delay. (b) Number of detected coincidences in the central peak, as a function of the voltage across the piezoelectric fiber stretcher ΔV. Epitaxy M2AG019, type 2 PM process, 15nm linewidth filter, integration time 180s.

In Figure 3.16 we show the result of the measurement for a type 2 PM process, using a 15nm large spectral filter. In 3.16a we can see in a glance a full oscillation period in the collected central peak of the coincidence histogram, while the satellite peaks are not influenced by the phase introduced by the fiber stretcher when changing the voltage ΔV. In 3.16b we have the detail on the central peak: the red dots represent the number of coincidence events collected in the central peak within the integration time (180s in this case) and for the given ΔV across the piezoelectric stretcher; the errorbars correspond

[17]The filter itself introduces around 2dB of losses; the narrower the bandwidth, the lower the number of photons that are transmitted through the filter, for a fixed JSA.

to the Poissonian noise. The blue line is a sinusoidal fit of the points, which helps in visualizing the interference pattern and in retrieving the contrast. Finally, the yellow points are the noise collected in a very large noise window, normalized with respect to the signal window width: the value is extremely low, demonstrating that in a first approximation its impact on the visibility can be neglected.

The measured visibilities, for the different types of phase-matching process and filter bandwidths, are displayed in Figure 3.17, together with the theoretical prediction of the model presented in the previous Section. In this case, to have a more accurate modelling of our system, we first simulated the actual shape of the JSA for the type 0 and type 2 PM processes, and we inserted these functions in Equation (3.32), with the required adjustments when considering the type 2 process (different JSA according to the polarization of the signal, PBS in the last step). We can see that the experimental data follow well the model's trend, even if the experimentally obtained values are slightly lower than the corresponding theoretical ones. This might be due to some effects not yet included in the model that degrade the entanglement visibility (as multi-pair events and accidentals [77]), as well as residual birefringence effects due to the non-ideal behaviour of the Faraday mirrors. The experimental points in the tail of the curve were taken without any filter, so with the full signal bandwidth: the resulting visibilities are in accordance with the bandwidths deduced by the JSA. In conclusion, we have demonstrated that we are able to produce energy-time entangled photon with a very high entanglement visibility – up to 98% for type 0 and to 99% for type 2, after proper spectral filtering –, that can be exploited for quantum information protocols. In this sense, for the next generation devices, it will be useful to implement the dispersion compensation methods discussed in the last Section, to avoid the spectral filtering and the related loss of signal, in terms of number of pairs and of available bandwidth.

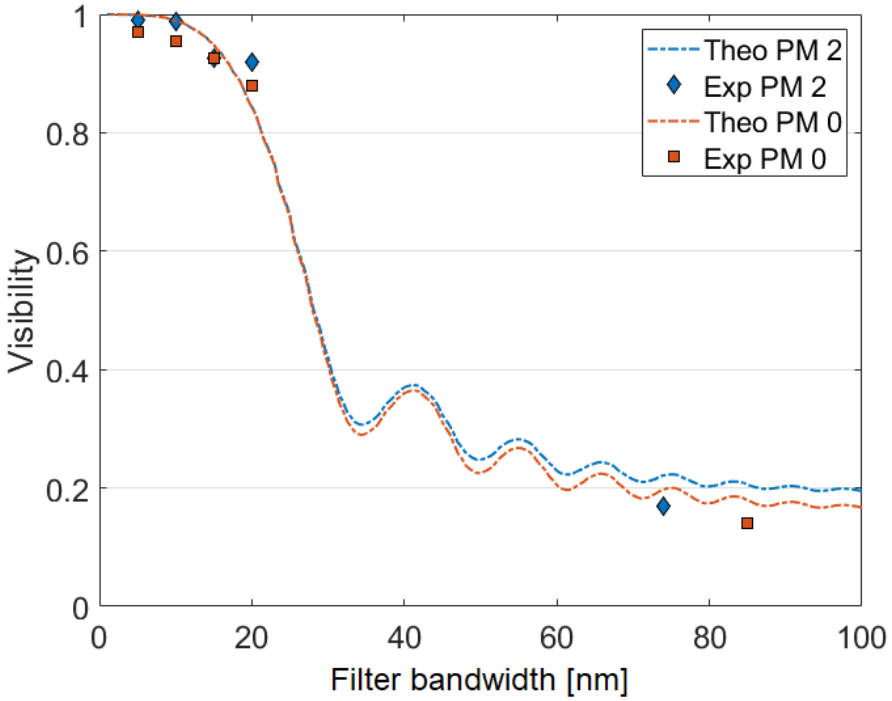

Figure 3.17: Measured entanglement visibilities for type 0 and type 2 phase matching processes, as a function of the bandwidth of the spectral filter.

4 | AlGaAs/SOI integration: the hybrid device

In this last Chapter, we introduce and describe the hybrid device resulting from the integration between the epitaxial AlGaAs wafer allowing to fabricate the two-photon sources and a standard SOI (silicon-on-insultator) wafer. We first give a brief overview on the integrated III-V/SOI devices, based on [79], focusing on the advantages that they can bring into the quantum photonics world; then, the working principles and the corresponding design of the device here proposed are presented. Finally, we discuss the obtained experimental results and the future developments.

4.1. III-V/SOI integration

The general concepts and methods towards the III-V/SOI hybridization are briefly presented in this Section, discussing the main criticalities and the implemented solutions. In particular, we describe the evanescent coupling method, for transmitting light from the III-V to the SOI waveguides. Furthermore, we present some available solutions for the injection and collection of light in and out the waveguides: this is not strictly related just to the hybrid devices, it is of interest also for monolithic solutions, but it becomes crucial at this point of the analysis.

4.1.1. Hybridization in a nutshell

In Section 1.3.2, we introduced the SOI platforms, describing some of their advantages (good mode confinement, moderate optical losses, high third order non-linearity, fabrication maturity and large-scale high-yield production capability) and disadvantages (absence of second order non-linearity). A further limitation of these platforms is the fact that silicon has an indirect bandgap, so that it is of great difficulty to achieve the laser action and, thus, realize a fully integrated source [80]. A solution to compensate for this limitation is to integrate the SOI with other platforms, more suitable for the electrically

pumped laser action. Monolithic integration has been demonstrated for germanium [81], compatible with CMOS fabrication processing but with indirect bandgap, and especially for GaAs and InP [82], III-V materials with direct bandgap, epitaxially grown on silicon. The direct growth is a critical step, due to the large mismatches between the crystal lattices and the thermal expansion coefficients. Therefore, although they represent very promising solutions, a lot of work is still needed to obtain efficient monolitically integrated sources, emitting in the telecom range and well coupled to the SOI circuits. Another solution, which is the one adopted for our device, is the heterogeneous integration of III-V on silicon: in this case, III-V stacks are separately grown onto their native substrate and later bonded on the already patterned silicon platform. At this point, the III-V waveguides are etched aligned with the SOI ones and the eventual metal deposition of the electrical contacts is performed[1]. Direct [83], adhesive [84] and metal [85] bondings have been demonstrated so far, showing trade-offs between tolerance to surface roughness, CMOS compatibility, thermal conductivity and optical absorption. The bonding is usually performed between single dies of III-V and silicon: direct wafer-to-wafer bonding is not efficient, due to the different wafer sizes (2", 3", 4" or 6" for the III-V, 8" or 12" for the SOI). Once the waveguides are etched, the confined optical mode will be evanescently coupled between the III-V and SOI, as described in Section 4.1.2.

Hybrid devices realized by heterogeneous integration show several advantages: the bonding is typically highly tolerant towards misalignment, while the alignment is easily achieved in at the photolithography stage; being the integration implemented at wafer level, it results in a cost-reduced simplified packaging. Moreover, very low coupling losses have been demonstrated [86], paving the way to the full exploitation of the silicon functionalities: although it is not a good light emitter, many elements useful for the laser action and for the light manipulation – feedback stage, cavity mirrors, wavelength selection, output coupling, modulators – can be implemented on the SOI platform, making use of the mature and well mastered CMOS fabrication technologies for obtaining reliable, high performance and high fabrication yields silicon components, while concentrating the nonlinear and gain action in the III-V medium. On the other hand, some constraints have limited the actual realization of complex hybrid photonic circuits. In fact, III-V materials are not yet within the standards of the CMOS fabrication platforms, hence they cannot be automatically employed for the silicon photonics. In this sense, another issue is that the metal used for the electrical contacts on the III-V waveguides for the electrically pumped laser action is gold-based, which is not compatible with the silicon fabrication processes, being one of

[1]If those steps are performed before the bonding, we talk about *external integration* of the laser source; this solution, which might appear simpler, in reality suffers from very low tolerance towards spatial misalignments.

its dopants. Furthermore, the thickness standard for the waveguides in the SOI circuits is 300nm, while the coupling is generally maximized for thicker waveguides (400-500nm). As a last remark, the III-V medium is typically 3-5μm high, avoiding the conventional multi-level metallization of the silicon platform, having approximately the same height and requiring a planar surface to be implemented. In conclusion, reaching the full value appreciation of the hybrid devices, requires to find solutions to effectively solve these trade-offs: a considerable research effort is pushing in this direction.

4.1.2. Evanescent coupling

In heterogeneously integrated devices, the coupling efficiency between the III-V and the SOI waveguides is of crucial importance. The distribution of the optical mode between them varies according to their geometry, which sets the amount of optical power in each side. In some hybrid devices, the optical mode is mainly confined in the silicon waveguide and evanescently coupled with the active medium [87], so that light is already well coupled into the photonic circuit, at the cost of affecting the gain and the nonlinear conversion; viceversa, a mode mainly confined in the III-V waveguide [88] will maximize the gain, while decreasing the efficiency of the coupling with the SOI circuits. To try to solve this trade-off, a possibility is to have first the mode well confined in the active region, to ensure a large gain and a large nonlinear overlap, and then to couple it with the silicon waveguide at the edges of the structure. This approach is the one chosen for our device, and it can be mathematically formulated with the coupled-mode theory, which will be here briefly introduced.

Consider two isolated loss-less waveguides, 1 and 2, whose fundamental modes can be written as:

$$E_{1,2}(x,y,z) = E_{1,2}(y)U_{1,2}(x,z)e^{-i\beta_{1,2}y}, \tag{4.1}$$

where $U_{1,2}(x,z)$ is the transverse field distribution, $\beta_{1,2} = 2\pi n_{eff}^{1,2}/\lambda$ is the propagation constant and we have considered the reference frame used so far, where y is the propagation direction. If the two waveguides are distant enough, the field magnitude will remain constant along the y axis. As soon as $U_1(x,z)$ and $U_2(x,z)$ begin to overlap, one field acts as a perturbation on the other, inducing variations in its distribution and magnitude, all along the propagation direction. Under the the weak coupling condition, this interaction can be described by a set of coupled differential equations, the so-called *coupled-mode equations* [89], whose solutions can be expressed using the *supermode* formalism. With supermode we refer to a coherent superposition of the two modes in the waveguides; a generic supermode, $\tilde{E}$, can be therefore represented with a column vector

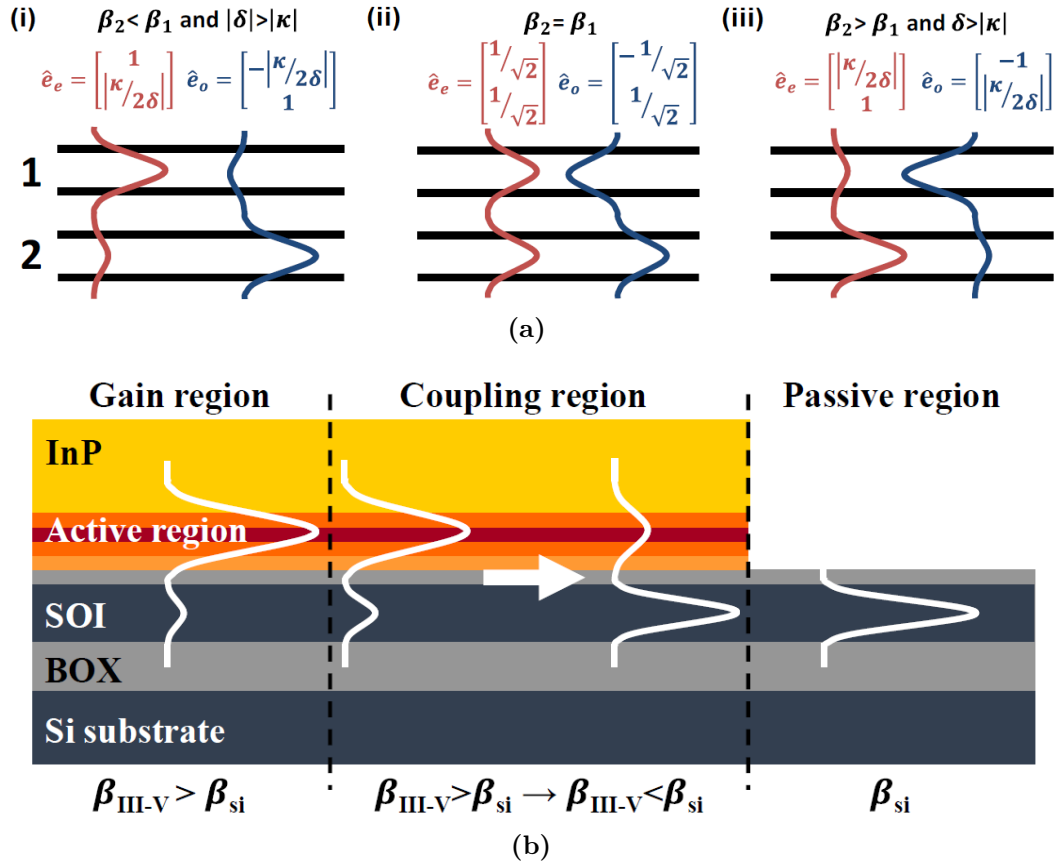

Figure 4.1: Schematic representation of (a) the even and odd supermodes and (b) of a practical implementation of the adiabatic coupling in an InP/SOI hybrid integration. From [79].

in the $(U_1(x,z), U_2(x,z))$ basis:

$$\tilde{E}(x,y,z) = \begin{bmatrix} E_1(y)e^{-i\beta_1 y} \\ E_2(y)e^{-i\beta_2 y} \end{bmatrix}. \tag{4.2}$$

The two solutions of the coupled-mode equations are the even ($\tilde{E}_e$) and odd ($\tilde{E}_o$) supermodes:

$$\begin{cases} \tilde{E}_e(x,y,z) = \dfrac{1}{\sqrt{2}} \begin{bmatrix} \sqrt{1-\delta/S} \\ \sqrt{1+\delta/S} \end{bmatrix} e^{-i(\bar{\beta}+S)y} = \hat{e}_e e^{-i\beta_e y} & \text{(4.3a)} \\ \tilde{E}_o(x,y,z) = \dfrac{1}{\sqrt{2}} \begin{bmatrix} -\sqrt{1+\delta/S} \\ \sqrt{1-\delta/S} \end{bmatrix} e^{-i(\bar{\beta}-S)y} = \hat{e}_o e^{-i\beta_o y}, & \text{(4.3b)} \end{cases}$$

with $\delta = (\beta_2 - \beta_1)/2$, $\bar{\beta} = (\beta_2 + \beta_1)/2$ and $S = \sqrt{\delta^2 + k^2} = (\beta_e - \beta_o)/2$, where β_e and β_o are the propagation constants of the supermodes and k is the coupling strength, proportional to the overlap between $U_1(x,z)$ and $U_2(x,z)$. In Figure 4.1a we show the

schematic representation of these solutions, for different values of β_1 and β_2.

Two different types of coupling can be achieved: the directional coupling and the adiabatic coupling. The directional coupling is obtained when the phase-matching condition $\beta_1 = \beta_2$ is satisfied, as depicted in Figure 4.1a.(ii). In this case, the supermodes are equally distributed in the two waveguides, but, according to the phase between them, they will interfere constructively or destructively in each guide. The phase difference varies during the propagation, since β_e is different from β_o when $k \neq 0$. In particular, if at some point the two supermodes have the same phase, all the optical power will be confined in the waveguide 2; after a propagation of length $L = 2\pi/k$, they will have acquired a phase difference of π, resulting in all the optical power being transferred in waveguide 1. In this ideal case the coupling efficiency is 100%; however, if the phase-matching condition is not perfectly satisfied, this efficiency can be strongly reduced. Therefore, although it is a very efficient method for transferring the optical power between two identical waveguides, it is not suitable for hybrid devices, composed of different materials for which the phase-matching condition is not, in general, satisfied. On the other hand, one could apply the transformation from Figure 4.1a.(i) to 4.1a.(iii), in which the even (odd) supermode is confined in the waveguide with the highest (lowest) propagation constant. Only one supermode is, in general, promoted to optical confinement or to lasing in the gain medium by the design; assume we promote the even supermode. Hence, by varying the geometry of the waveguide, we can change the effective refractive index and, thus, the propagation constant, in order to gradually move from (i) to (iii). The easiest way to implement this is to vary the width of the waveguide, forming *tapers*: this method is very effective in tuning the index of the TE modes (horizontally distributed), which are the ones typically supported by the silicon photonic circuits. A schematic representation of a hybrid III-V/Si – in this case, the III-V material is InP – device exploiting the adiabatic coupling solution is shown in Figure 4.1b: "adiabatic" stands for the fact that the taper is designed in order to avoid the optical power to be scattered into other modes. In conclusion, although with this method it is impossible to achieve 100% of coupling efficiency and the required coupling length is in general longer than the one for the directional coupling, the adiabatic coupling is significantly more robust in obtaining the mode transfer [90], thus resulting more suitable for hybrid structures.

4.1.3. Injection-collection solutions

In the experiment presented in the previous chapter, for the injection and collection of the optical modes in and out the waveguides, we have used two microscope objectives. This solution provides for the largest available numerical aperture, being extremely useful

especially in collection, since it makes it robust against misalignments. In addition, it offers a large choice in terms of working distances, while the transmission can be essentially wavelength independent; indeed, when varying the wavelength only the focal distance needs to be adjusted. Before and after the objectives, the optical mode is in free-space, which can be useful – for example, if you need to visualize the shape of the mode or to test its polarization – but can also induce unnecessary optical losses, especially if one needs a direct link with a fibered communication or measurement system. Moreover, using microscope objectives might not be the easiest way to achieve the optical alignment in more complex structures, such as the hybrid devices where the two waveguides are located at two different heights, and other options with higher coupling efficiency can be implemented taking benefit of the large variety of optical components developed in the silicon platforms. We will introduce here two solutions that will be used in the followings: micro-lensed fibers and grating couplers. These alternative coupling techniques and the corresponding setups were designed and implemented for the first time in the group for the demonstration of our hybrid device.

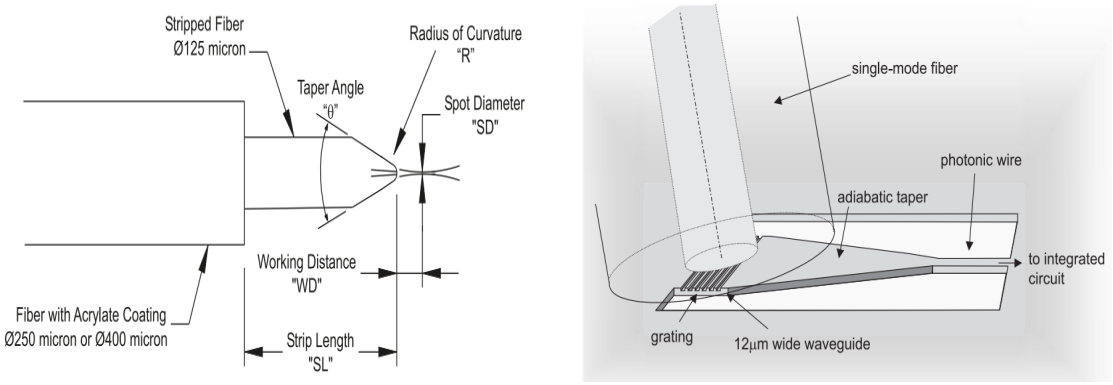

(a) **(b)**

Figure 4.2: Sketch of (a) a micro-lensed fiber (from [91]) and (b) a grating coupler (from [92]).

A micro-lensed fiber can be obtained from a common single-mode fiber: the external coating is first stripped away, the remaining part is cleaved and tapered in order to form a lens. According to the shape of the taper, different combinations of focal distances – also called *working distances* – and *spot sizes* can be achieved, being the spot size the diameter of the optical mode in the focal plane. In Figure 4.2a, the sketch of a micro-lensed fiber is displayed, indicating the useful parameters. By controlling the spot size, we can maximize the overlap between the fiber mode and the mode supported by the waveguide, enhancing the coupling efficiency. The smaller the spot size, the smaller the working distance, thus requiring higher stability and resolution for the moving stage. In fact, the optical mode

propagates, in a good approximation, as a Gaussian mode, diverging when getting far from the focal plane. These characteristics, together with a resulting strongly limited numerical aperture (<0.14), makes the micro-lensed fibers suitable for the injection of the optical mode into the waveguide. In complex structures, such as hybrid devices or waveguide arrays [93], it can be very useful to have a strong control on the injection point – a level of control that is hardly reached with, for example, a microscope objective, due to the large numerical aperture and the large working distance. On the other hand, the collection might be less efficient with a micro-lensed fiber, which is also far less robust towards small displacements.

Grating couplers offer one of the most efficient and robust coupling solutions to silicon integrated circuits. They exploit periodically etched structures to directly convey light coming from a cleaved optical fiber into the waveguide, as shown in Figure 4.2b. As described in [92], the Bragg diffraction principle is used for this scope. For this reason, the coupling efficiency of the gratings is strongly wavelength dependent and is characterized by a limited bandwidth – typically, few tens of nm. By changing the injection angle of the optical fiber, one can tune the center of the transmission bandwidth. Furthermore, the coupling efficiency is generally polarization selective, although polarization-independent couplers, featuring more complex designs, have been demonstrated [94]. More and more efficient grating couplers are being designed, relying on the mature management of the fabrication processes in silicon. Very high coupling efficiencies can be reached with this method [95]; in hybrid structures, they can be implemented for the efficient injection or collection of the optical mode on the silicon side.

4.2. Design and working principles

A first simple design for the hybrid AlGaAs/SOI device was proposed in our group by J. Belhassen [96], and was then greatly refined and experimentally realized by J. Schuhmann, a current PhD student of the group, with the additional help of F. Boeuf (from ST Microelectronics) for the design part and of F. Raineri (from C2N) for the fabrication part. Here we briefly present the fabrication protocol and the final design conceived for the device.

4.2.1. Fabrication

In Section 2.2.1, we described our AlGaAs epitaxial structures, whose composition is listed in Table 2.1. These structures are supposed to be employed for the realization of the hybrid device: they are covered by a 20nm layer of SiO_2 (deposited via atomic layer

deposition, ALD) and turned upside down, so that the top layer is bonded with the SOI chip. We implement an adhesive bonding, using a polymer layer of benzocyclobutene (BCB) as adhesive; with this technique, we do not have strong requirements towards the surface roughness. The BCB is spin-coated onto the SOI surface, together with an adhesion primer per each bonding side. Note that this step is also crucial in setting the gap distance between the two waveguides, which is a relevant parameter for the evanescent coupling efficiency. Once the bonding is completed, the GaAs substrate must be removed, in order to be able to proceed with the etching of the waveguides. The removal is done through a selective chemical etching, with an acid bath in a solution of citric acid and H_2O_2: the structure will be etched on the AlGaAs side down to the so-called etch-stop layer. This layer is later etched using the buffered oxide etching (BOE), which stops once the following thin layer of GaAs, representing now the top cap of the structure, is reached. Some bonding constraints might be released once the substrate is removed, hence this is a delicate step: the role of the previously deposited layer of SiO_2 is to help in relaxing these constraints and avoid the sample to be damaged. In Figure 4.3a, a picture of the hybrid device after the substrate removal is displayed: we can observe, in this case, the damages caused by the bonding constraints on the AlGaAs epitaxial structure (the darkest central rectangle – the rest is the SOI chip). They can be very detrimental for the final realization of the device, reducing the effective area where it is possible to etch the waveguides.

Once the substrate is removed, the AlGaAs waveguides can be etched. We use ICP etching, in order to be able to realize the tapers for the adiabatic evanescent coupling, as will be detailed in the following. Gold marks are previously deposited on the SOI to align the etching process, so to have the AlGaAs waveguides perfectly superimposed to the silicon ones. We can now cleave the the sample on the AlGaAs side, to realize the input facets; on the silicon side, the cleaving might or might not be necessary, depending on whether we implemented a grating coupler for the collection/injection of the optical modes. In Figure 4.3b, we have an optical microscope picture of the resulting AlGaAs facet, where we can observe the different material layers: we sketched the shape of the silicon waveguide, since on the AlGaAs side it is not visible (see Figure 4.5b). It is now clear why we chose to have only two Bragg mirrors on one side of the core: in this way, the distance between the two waveguides is reduced, and the evanescent coupling can be maximized, as it will be explained in the next Section. A SEM picture of the coupling region, showing the etched edge of the AlGaAs taper and the silicon waveguide beneath it, is displayed in Figure 4.3c. Finally, a schematic representation of the fabrication procedure is displayed in Figure 4.4.

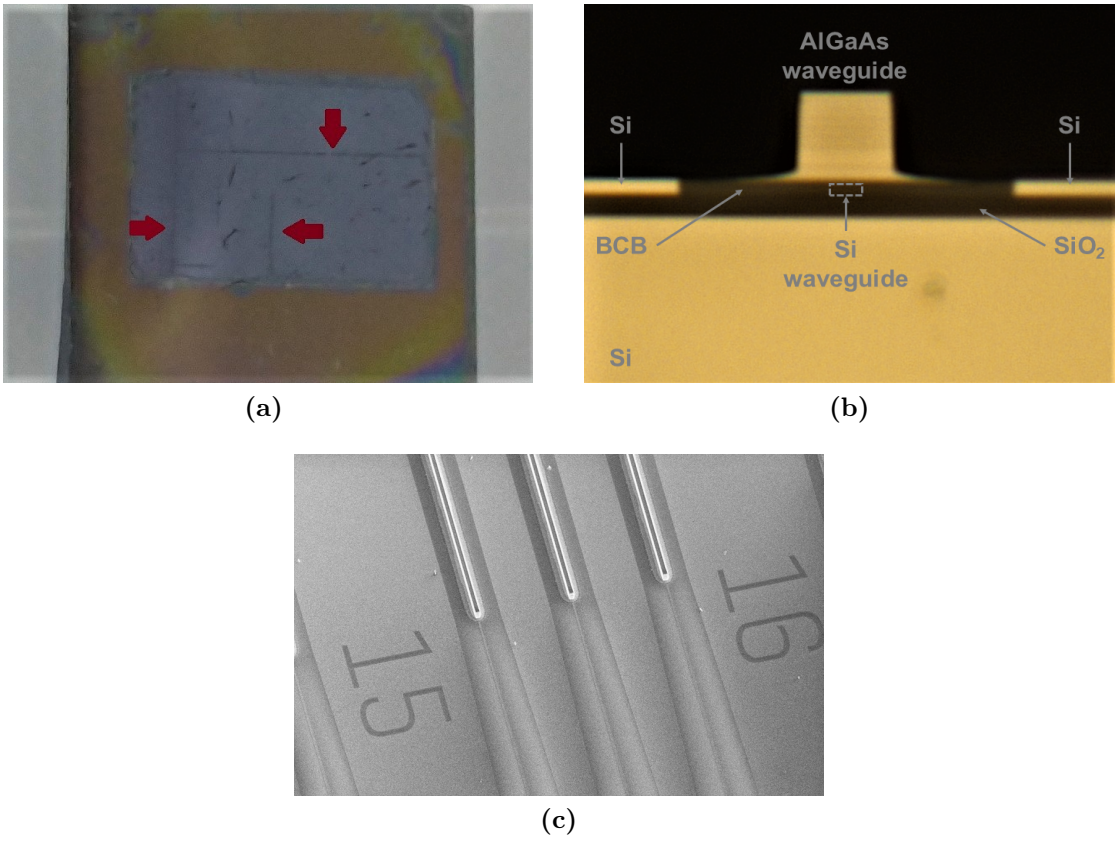

(a) (b)

(c)

Figure 4.3: Picture of (a) the hybrid device after the substrate removal – note the fractures resulting from the bonding constraints, indicated by red arrows – , (b) an etched AlGaAs waveguide, where the different material and epitaxial layers are visible (optical microscope picture) and (c) the coupling region after the AlGaAs etching (SEM picture).

4.2.2. Design

The design of the hybrid device has to cope with the three regions displayed in Figure 4.1b: we need a region where to have access to the material non-linearity, a coupling region where the optical mode is transferred from the III-V to the Si waveguide and, finally, the Si integrated circuit. In the nonlinear region, we placed a 4.5μm wide AlGaAs waveguide, whose length must be kept around 2mm, in order to maximize the trade-off between losses and second order conversion efficiency. The width is reduced, via a taper, to 1.1μm; in particular, the passage from 1.5μm to 1.1μm falls into the so-called coupling region (or area): an inverse tapered silicon waveguide, passing from 600nm to 1350nm with three different slopes, is placed exactly below the AlGaAs one. Finally, the Si waveguide, where the optical mode is supposed to be transferred, paves the way to the integrated SOI circuits. The plan and the frontal view of the proposed device are shown in Figure 4.5.

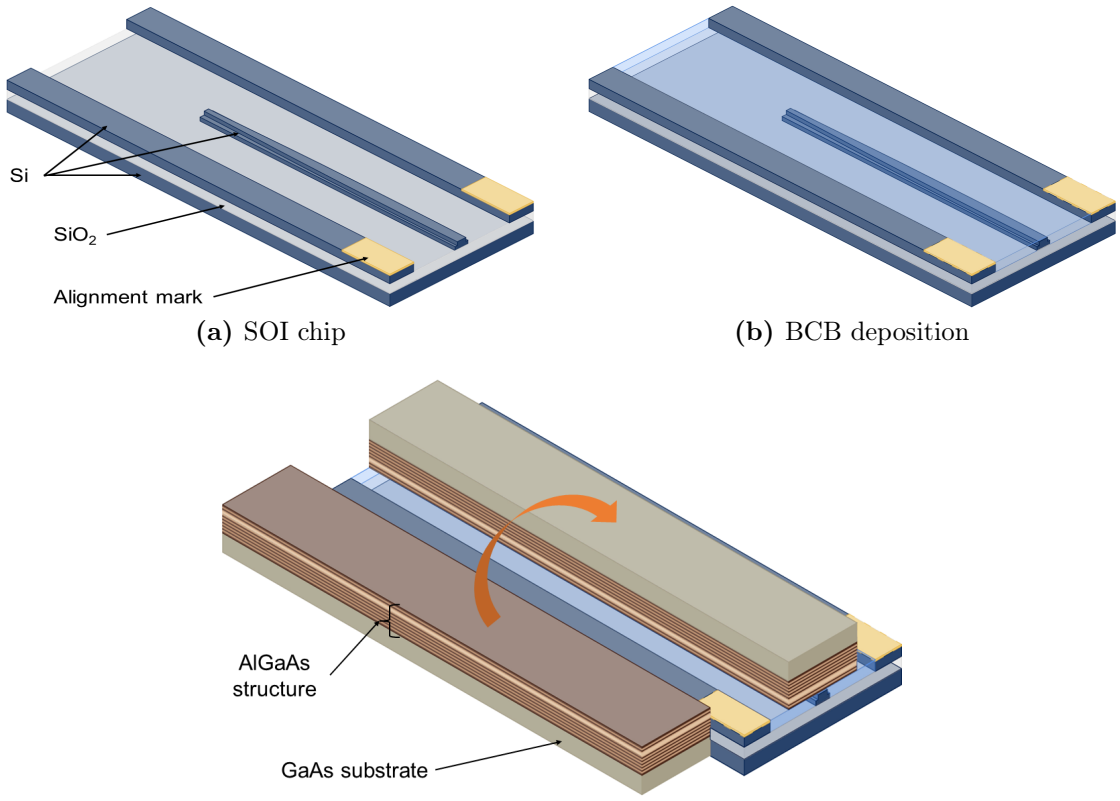

(a) SOI chip **(b)** BCB deposition

(c) Adhesive bonding

(d) Substrate removal **(e)** AlGaAs etching

Figure 4.4: Schematic representation of the steps involved in the fabrication procedure of the hybrid AlGaAs/SOI device. In blue: silicon layers; in light blue: BCB; in light gray: SiO_2; in shades of brown: AlGaAs layers.

Two different SOI chips where employed for our device: one realized by ST Microelectronics (ST) and one by the C2N lab. The first one is 300nm high, supports only the TE mode[2] and features a grating coupler (coupling losses smaller than 0.5dB) on the collection

[2]Actually, the TM mode can propagate as well, although with a lower confinement. In addition, on one hand its effective refractive index is significantly lower, making it more difficult to achieve the adiabatic coupling, and on the other hand the integrated components are typically optimized only for the TE mode, which ensures to have perfectly single-mode waveguides while minimizing the height of the structures.

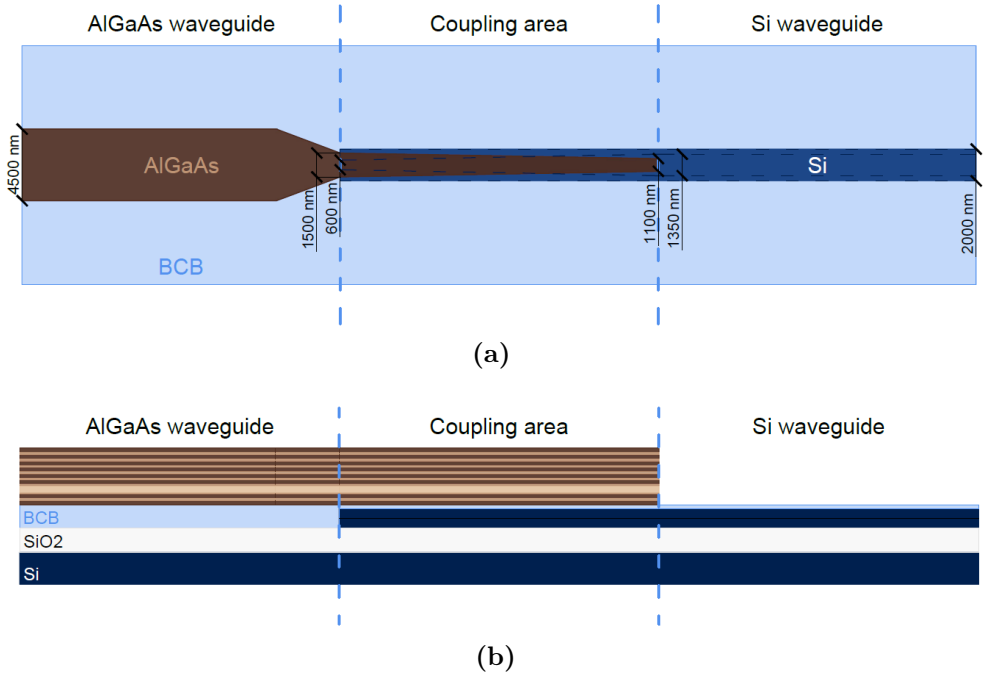

Figure 4.5: (a) Top and (b) side view of the proposed hybrid device, with the different regions and the real dimensions indicated; not on scale.

side; in the coupling area, in order to maximize the coupling efficiency, it is shaped as a pyramid, with two layers of different width, as shown in the transversal sections displayed in Figure 4.6a. The second one is 610nm high, supports both TE and TM modes and is a single-layer tapered waveguide. Here we discuss the optimization for the ST structure, but an equivalent procedure can be applied to the other one.

We can now study the coupling efficiency as a function of different parameters, in particular the coupling length, the gap and the displacement between the waveguides, the wavelength of the optical mode. This is done via numerical simulations in Lumerical MODE, which is a commercially available software optimized to propagate the electromagnetic field through the matter. The coupling length is a crucial parameter, since it sets the footprint of the device, which should be minimized. According to our simulations, we are able to achieve the complete transfer of the mode in a length of around 200μm. In Figure 4.7, we display the results of the simulations. We can see that the device is robust to displacements between the waveguides (Figure 4.7b – it is symmetric for negative displacements), so to eventual fabrication imperfections. Moreover, the transmission spectrum covers the whole telecom band (Figure 4.7c), therefore the full bandwidth of our signal can be efficiently transferred to the silicon chip. Last, we can observe that there is an optimal value for the gap, optimizing the coupling (Figure 4.7a): this might

Hence, we consider as if only the TE mode was supported.

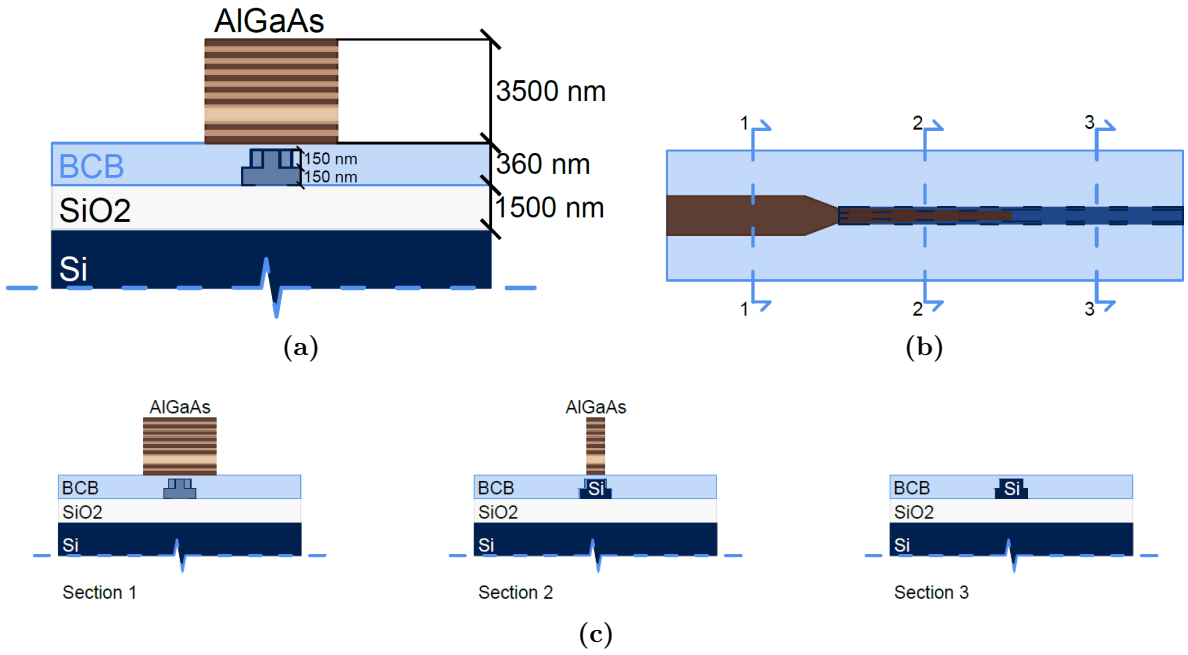

Figure 4.6: (a) Transverse section of the device, with the dimensions indicated. (b) Map of the sections displayed in (c), for different relevant parts of the device. Not on scale.

be counter-intuitive, but if the waveguides are too close, the transfer efficiency drops. The same kind of analysis can be performed to define the optimal shapes and dimensions of the tapers, as shown in Figures 4.8a and 4.8b, setting the final structure of the device.

4.2.3. Working principle

After having clarified the design choices and the fabrication protocol, we will discuss how this device can actually be tested and used for applications. In this thesis, we will concentrate on the passive device, optically pumped: the implementation of an electrically injected device will be the object of future work. The idea is to test the nonlinearity of the AlGaAs through the generation of second harmonics and to exploit it to produce photon pairs by SPDC. Recall that the silicon is not transparent to red light, which is strongly absorbed ($\alpha \simeq 10^3 \text{cm}^{-1}$, from [97]). Therefore, for the second harmonic generation, the infra-red optical pump is injected in the silicon side, while the generated red signal is collected from the AlGaAs side; on the contrary, for the photon-pair creation via SPDC, the red optical pump is injected in the AlGaAs waveguide, while the produced pairs are collected from the silicon circuit. The practical implementation of these experiments is presented in Section 4.3.1. Note that, according to the chosen silicon waveguide, we have access to different phase-matching processes: in the case of the ST waveguide, supporting the TE polarized mode, only the type 1 PM conversion, in which the infra-red pump or

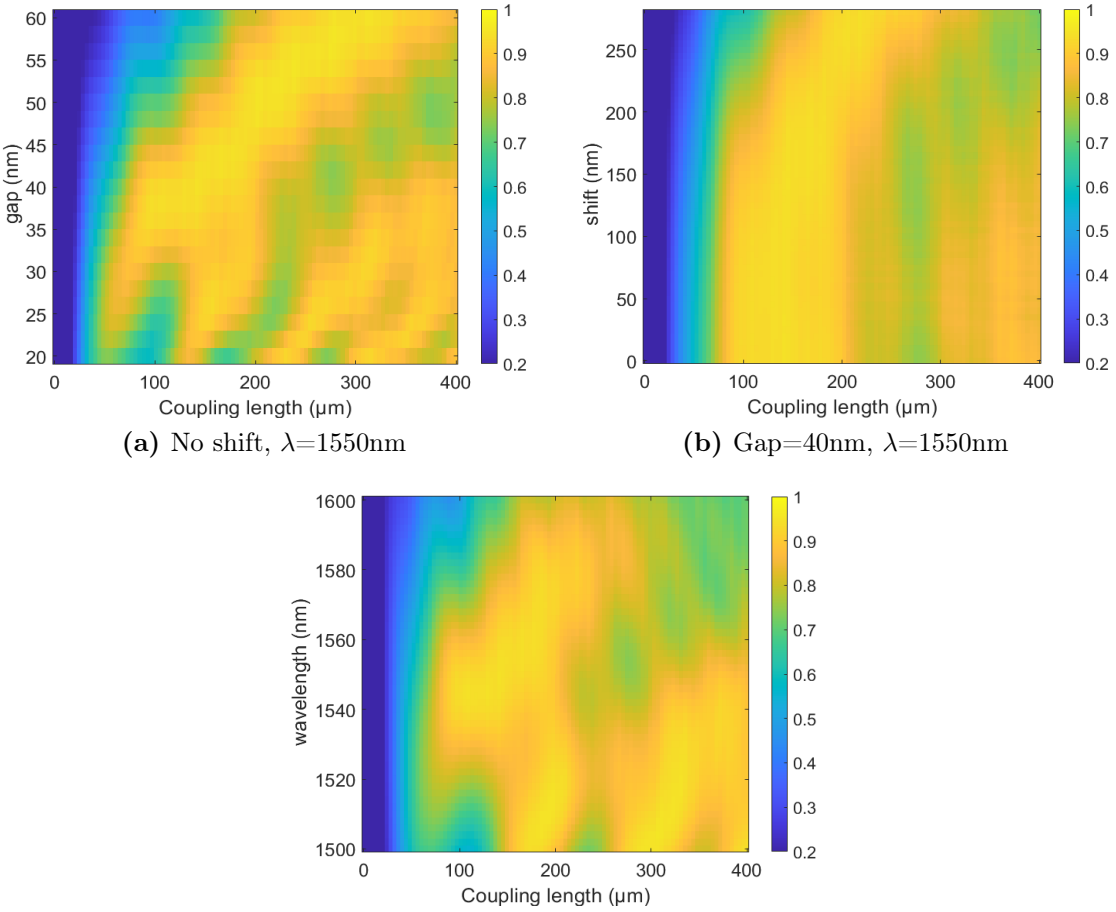

(a) No shift, λ=1550nm

(b) Gap=40nm, λ=1550nm

(c) No shift, gap=40nm

Figure 4.7: Optical mode transfer – from the AlGaAs to the Si waveguide – efficiency as a function of the coupling length and of (a) the vertical gap size, (b) the lateral offset (shift) between the waveguides and (c) the wavelength of the mode; the value of the fixed parameters is indicated in the picture caption.

signal is supposed to be TE-polarized, is accessible. However, as discussed in Sections 3.2.2 and 3.3.2, we have not observed a strong enough type 1 PM conversion process in our sample. Hence, we had to adopt the other structure, supporting also the TM mode, to have access to the type 0 and type 2 PM processes. In particular, the type 0 PM process is particularly suitable, since the two generated photons have parallel polarization, so the coupling efficiency to the SOI waveguide is the same. For this reason, we concentrated our attention on energy-time entanglement instead of on polarization entanglement produced in the type 2 PM conversion processes. In Figure 4.9, a 3D perspective of the described hybrid device is displayed, showing by means of coloured spheres – representing the involved photons – its working principle: in particular, in the case of SPDC, the photon-pair is produced in the AlGaAs waveguide from down-converted red pump, and the two pho-

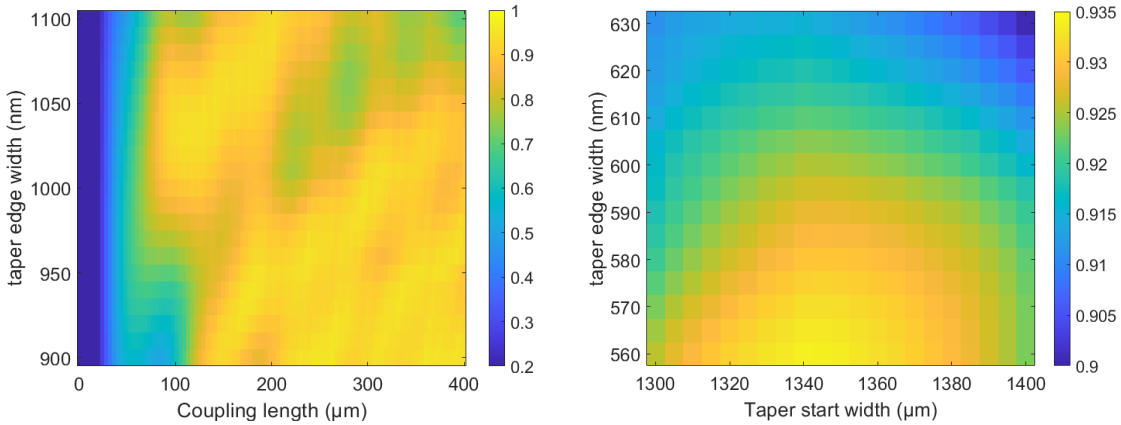

(a) AlGaAs taper **(b)** Si taper

Figure 4.8: Optical mode transfer – from the AlGaAs to the Si waveguide – efficiency as a function (a) of the coupling length and the final width of the taper in the AlGaAs waveguide and (b) of the starting and final widths of the taper in the silicon waveguide, for a coupling length of 180μm. Gap=40nm, no lateral offset, $\lambda = 1550$nm.

tons are later tranferred to the silicon waveguide via the adiabatic evanescent coupling. They can now be collected and experimentally characterized, in terms of performances and entanglement visibility, as discussed in Sections 3.3 and 3.4. Note that, thanks to the fact that the silicon strongly absorbs the red light, the optical pump is automatically filtered out once the signal enters the SOI circuit, without requiring additional integrated components: this is a great advantage of the proposed hybrid device.

4.3. Results and perspectives

In this last Section, we present the early experimental results obtained with the hybrid device and the measurement protocol elaborated for the demonstration of its operation in the classical and quantum nonlinear regime. The next steps are then discussed, both for the immediate and for the future developments.

4.3.1. Measurement protocol and first results

The necessity of developing a new measurement protocol comes from the fact that red light is not transmitted by the silicon waveguide, causing the optical alignment to be less straightforward. Hence, we make an alternate use of micro-lensed fibers and microscope objectives[3].

[3]We recall that, since no strong enough type 1 PM is generated from our sources, we are using the silicon chip that does not feature the grating coupler for the collection/injection; hence, this chip is

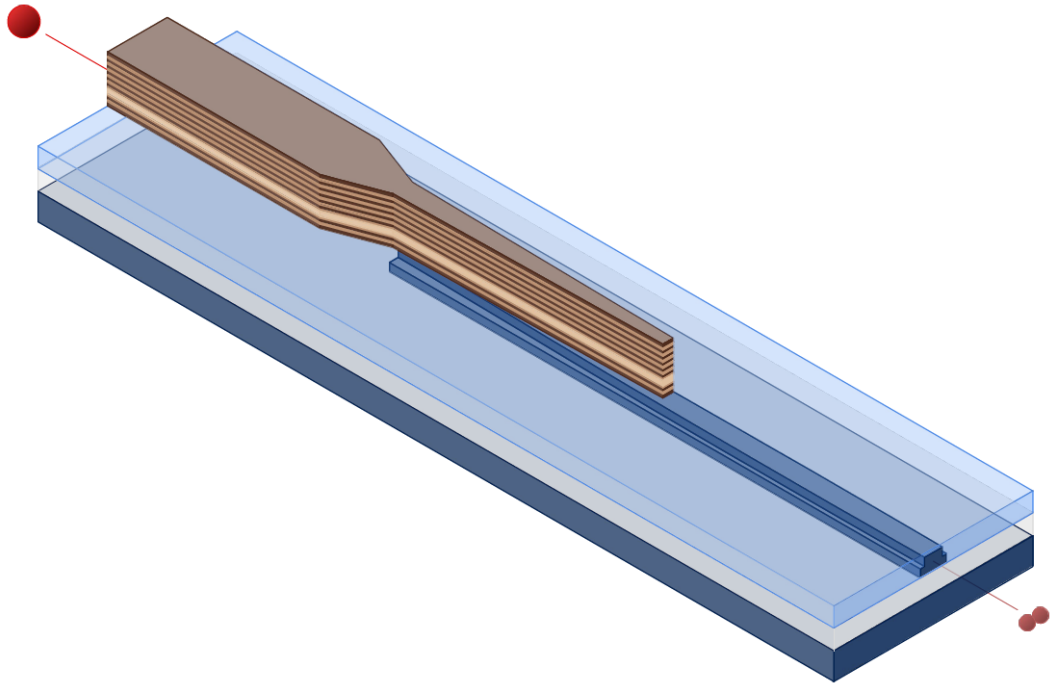

Figure 4.9: 3D representation of the hybrid device and its working principle: the red sphere represents a pump photon which is down-converted within the AlGaAs waveguide via SPDC into two infra-red photons (pink spheres), collected at the output of the Si waveguide; viceversa for the SHG process.

First, we measure the transmission of the IR optical mode of the device. Note that the method for the direct calculation of the attenuation coefficient from the Fabry-Perot interference fringes (see Section 3.1.1) cannot be applied, since the integrated device presents a combination of different cavities, resulting in a complex superposition of interference profiles. Therefore, we measure the absolute transmission. The first alignment is done using micro-lensed fibers both in injection and collection: on the Si side, we have a fiber with a 2.5μm spot size, while on the AlGaAs side a 4.5μm spot size, in order to better match the mode dimensions (the spot sizes roughly correspond to the widths of the waveguides). A very sensitive powermeter (*EXFO*, sensitivity down to -90dBm) is used to maximize the transmission. However, with the fibers, we do not have access to the polarization of the transmitted mode. Hence, we remove the collection fiber and we place a microscope objective: a polarizer can be now used to measure the polarization of the mode transmitted by the device, under the assumption that the polarization state is conserved during the propagation; this assumption can be later checked by replacing also the second fiber and directly setting the input polarization. The absolute transmission is measured with

cleaved in order to have good facets also on the Si side.

a free-space powermeter. In this way, we were able to measure a transmission value comparable with the one obtained with monolithic straight waveguides of the same length, both for TE and TM modes, validating the efficiency of the designed adiabatic coupling and the successful processing of the taper.

The demonstration of the optical mode transmission required a strong effort to develop an efficient measurement protocol. Following the results of these first tests, we optimized the design of the structure, further enhancing the transmission and avoiding the propagation through parasite waveguides, initially present in the silicon platform. It represents an important first step and now the effort is directed towards the demonstration of the nonlinear and quantum operation of the device.

4.3.2. Next steps

As already pointed out in the last Section, the two very first next steps are the measurement of the SHG and the detection of the photon-pairs produced by SPDC, characterized by their performances, especially in comparison to a straight monolithic AlGaAs waveguide, and by their degree of energy-time entanglement visibility. A new generation of devices, with the design optimized for achieving the best transmission and integrating new epitaxial structures – more robust to the bonding constraints relaxations after the substrate removal, see Section 4.2.1 –, is being fabricated to this purpose. Meanwhile, the experimental setup has been upgraded thanks to the preliminary tests, and a measurement protocol has been elaborated also for the nonlinear experiments.

The further development of the hybrid device goes in two directions. The first one is the implementation of an active, electrically pumped heterogeneously integrated device. The idea is to process the active AlGaAs source (see Section 2.2.4) after the bonding with the SOI chip, in order to obtain the laser action directly on-chip and avoid the optical pumping. This introduces new relevant challenges, both in the fabrication – especially for the metal contacts deposition – and in the design – in particular for the combination of the optical cavity required for the lasing action and the taper required for the evanescent coupling. On the second direction, the aim is to exploit the potentialities of the SOI circuitry to realize more and more complex operations directly on-chip, as done, for instance, in [98]. As an example, we could implement an on-chip Franson interferometer, in order to have an immediate access to the quantum properties of the generated state.

5 | Conclusions and perspectives

The latest advances in the field of quantum information tend towards the realization of compact, high yield and high reliability devices, where the main functions, from the generation to the manipulation of the quantum state carrying the information, are integrated on a single chip. Different material platforms are nowadays investigated and a considerable effort is devoted to merge the advantages offered by each one of them, creating efficient and competitive hybrid devices.

In this master thesis, we introduced the contributions brought in by integrated quantum photonics (Chapter 1): controllable quantum states can be produced via light-matter interaction and the information is delivered by photons, exploiting the robustness of their coherence in propagation. In particular, we discussed the adoption of AlGaAs as a material platform for the implementation of waveguides based on Bragg reflectors (Chapter 2), working at room temperature and featuring a direct bandgap suitable for exciting the laser action. We experimentally demonstrated, through second harmonic generation, the nonlinear properties of these waveguides, and we characterized their capability to produce photon pairs in the telecom range via SPDC, evaluating the absolute performances for the different types of available conversion processes satisfying the phase-matching condition (Chapter 3). The generated quantum state was investigated in terms of energy-time entanglement visibility, through the use of a fibered Franson interferometer, realized for the first time in the laboratory. We developed a theoretical model to correlate the measured visibility to the spectral properties of the generated quantum state; the model was experimentally validated by manipulating the signal spectrum with tunable spectral filters. In this way, we demonstrated an entanglement visibility up to 99%, confirming the suitability of our sources for the application in the framework of the quantum communication technologies. Finally, we discussed the design of an optically pumped hybrid device, integrating the AlGaAs source with the SOI platforms (Chapter 4), illustrating the working principles and the fabrication procedure. The first experimental results, demonstrating the transmission of the infra-red optical mode from the AlGaAs to the silicon waveguide exploiting the evanescent adiabatic coupling, were also presented.

On a short term, the next steps point towards three directions. The first one is the enhancement of the conversion efficiency for the type 1 phase-matching process, essential for the full exploitation of the SOI circuitry in the hybrid device and, at the same time, increasing the versatility of the source. The second one is the upgrade of the Franson interferometer, adopting an approach based on the active phase-drift compensation instead of the temperature stabilization and implementing the local cancellation of chromatic dispersion, in order to take advantage of the whole spectrum of the produced quantum state. The third direction is the demonstration of the nonlinear and quantum properties of the designed hybrid device, through the measurement of second harmonic generation, of photon-pair production via SPDC and of the energy-time entanglement visibility.

On a longer term, we envisage the realization of an active, electrically pumped hybrid device, exploiting the direct bandgap of the AlGaAs source to obtain the laser action, as described in Section 2.2.4. The light produced by lasing is expected to excite the nonlinear processes involved in the photon-pair generation via SPDC. Hence, we would have access to the generation of the desired quantum state directly on-chip by electrical injection. Thanks to the transfer of the photon pairs to the SOI circuitry, a further next step would be the manipulation of this quantum state making use of the integrated silicon components. The realization of a chip enabling the direct generation and manipulation of the quantum information is the final target. To this aim, the collaboration between our group and ST Microelectronics and C2N has been confirmed and extended for the next years.

Bibliography

[1] T. Maiman. Stimulated optical radiation in ruby. *Nature*, 187:493–494, 1960.

[2] W. F. Brinkman, D. E. Haggan, and W. W. Troutman. A history of the invention of the transistor and where it will lead us. *IEEE Journal of Solid-State Circuits*, 32 (12):1858–1865, 1997.

[3] F. Arute *et al*. Quantum supremacy using a programmable superconducting processor. *Nature*, 574:505–510, 2019.

[4] J. Yin *et al*. Entanglement-based secure quantum cryptography over 1,120 kilometres. *Nature*, 582:501–505, 2020.

[5] M. Giustina *et al*. Significant-loophole-free test of bell's theorem with entangled photons. *Physical Review Letters*, 115:250401, 2015.

[6] The LIGO Scientific Collaboration. A gravitational wave observatory operating beyond the quantum shot-noise limit. *Nature Physics*, 7:962–965, 2011.

[7] F. Flamini, N. Spagnolo, and F. Sciarrino. Photonic quantum information processing: a review. *Reports on Progress in Physics*, 82:016001, 2018.

[8] A. Aspect, P. Grangier, and G. Roger. Experimental tests of realistic local theories via Bell's theorem. *Physical Review Letters*, 47:460–463, 1981.

[9] A. Einstein, B. Podolsky, and N. Rosen. Can Quantum-Mechanical Description of Physical Reality Be Considered Complete? *Physical Review*, 47:777–780, 1935.

[10] C. H. Bennett and G. Brassard. Quantum cryptography: Public key distribution and coin tossing. In *Proceedings of IEEE International Conference on Computers, Systems, and Signal Processing*, pages 175–179, Bangalore, India, 1984.

[11] J. D. Franson. Bell inequality for position and time. *Physical Review Letters*, 62, 1989. 2205.

[12] E. Polino, M. Valeri, N. Spagnolo, and F. Sciarrino. Photonic quantum metrology. *AVS Quantum Science*, 2:024703, 2020.

[13] D. Bouwmeester, J.-W. Pan, K. Mattle, M. Eibl, H. Weinfurter, and A. Zeilinger. Experimental quantum teleportation. *Nature*, 390:575–579, 1997.

[14] P. Michler. A quantum dot single-photon turnstile device. *Science*, 290:2282–2285, 2000.

[15] P. G. Kwiat, K. Mattle, H. Weinfurter, A. Zeilinger, A. V. Sergienko, and Y. Shih. New high-intensity source of polarization-entangled photon pairs. *Physical Review Letters*, 75:4337–4341, 1995.

[16] H.-S. Zhong *et al*. Quantum computational advantage using photons. *Science*, 370: 1460–1463, 2020.

[17] C. Sparrow, E. Martín-López, N. Maraviglia, A. Neville, C. Harrold, J. Carolan, Y. N. Joglekar, T. Hashimoto, N. Matsuda, J. L. O'Brien, D. P. Tew, and A. Laing. Simulating the vibrational quantum dynamics of molecules using photonics. *Nature*, 557:660–667, 2018.

[18] J. Wang, F. Sciarrino, A. Laing, and M. G. Thompson. Integrated photonic quantum technologies. *Nature Photonics*, 14:273–284, 2019.

[19] P. Franken, A. Hill, C. E. Peters, and G. Weinreich. Generation of optical harmonics. *Physical Review Letters*, 7(4):118, 1961.

[20] R. Boyd. *Nonlinear Optics*. Academic Press, 2008.

[21] C. Autebert. *AlGaAs photonic devices: from quantum state generation to quantum communications*. PhD thesis, Université Paris Diderot - Paris VII, 11 2016.

[22] C. Gerry and P. Knight. *Introductory quantum optics*. Cambridge University Press, 2005.

[23] P. A. M. Dirac. On the Analogy Between Classical and Quantum Mechanics. *Reviews of Modern Physics*, 17(195), 1945.

[24] J. S. Bell. On the Einstein-Podolsky-Rosen paradox. *Physical Review*, 48:195–200, 1964.

[25] D. Leibfried, B. DeMarco, V. Meyer, D. Lucas, M. Barrett, J. Britton, W. Itano, B. Jelenković, C. Langer, and T. Rosenband. Experimental demonstration of a robust, high-fidelity geometric two ion-qubit phase gate. *Nature*, 422(6930):412–415, 2003.

[26] J. Beugnon, C. Tuchendler, H. Marion, A. Gaëtan, Y. Miroshnychenko, Y. R. P. Sortais, A. M. Lance, M. P. A. Jones, G. Messin, A. Browaeys, and P. Grangier.

Two-dimensional transport and transfer of a single atomic qubit in optical tweezers. *Nature Physics*, 3:696–699, 2007.

[27] Y. Makhlin, G. Scöhn, and A. Shnirman. Josephson-junction qubits with controlled couplings. *Nature*, 398(6725):305–307, 1999.

[28] P. Neumann *et al.* Multipartite entanglement among single spins in diamond. *Science*, 320(5881):1326–1329, 2008.

[29] J.-P. W. MacLean, J. M. Donohue, and K. J. Resch. Direct characterization of ultrafast energy-time entangled photon pairs. *Physical Review Letters*, 120, 2018.

[30] V. Jacquese, E Wu, F. Grosshans, F. Treussart, P. Grangier, A. Aspect, and J.-F. Roch. Experimental Realization of Wheeler's Delayed-Choice Gedanken Experiment. *Science*, 315(5814):966–968, 2007.

[31] J. D. Franson. Violations of a simple inequality for classical fields. *Physical Review Letters*, 67:290–293, 1991.

[32] M. Horne, A. Shimony, and A. Zeilinger. *Down-conversion photon pairs: A new chapter in the history of quantum mechanical entanglement*, pages 356–372. WORLD SCIENTIFIC, 1991.

[33] Y. Wang, K. D. Jöns, and Z. Sun. Integrated photon-pair sources with nonlinear optics. *Applied Physics Reviews*, 8(011314), 2021.

[34] F. Boitier, A. Orieux, C. Autebert, A. Lemaître, E. Galopin, C. Manquest, C. Sirtori, I. Favero, G. Leo, and S. Ducci. Electrically injected photon-pair source at room temperature. *Physical Review Letters*, 112(183901), 2014.

[35] S. May, M. Kues, M. Clerici, and M. Sorel. Second-harmonic generation in AlGaAs-on-insulator waveguides. *Optics Letters*, 44:1339–1342, 2019.

[36] T. J. Steiner, J. E. Castro, L. Chang, Q. Dang, W. Xie, C. Li, J. Norman, J. E. Bowers, and G. Moody. Entangled Photon Pair Generation from an AlGaAs-on-Insulator Microring Resonator. In *Conference on Lasers and Electro-Optics*, page FTh1O.4. Optica Publishing Group, 2021.

[37] J. Lin, F. Bo, Y. Cheng, and J. Xu. Advances in on-chip photonic devices based on lithium niobate on insulator. *Photonics Research*, 8(12):1910–1936, 2020.

[38] C. Op de Beeck *et al.* III/V-on-lithium niobate amplifiers and lasers. *Optica*, 8(10): 1288–1289, 2021.

[39] S. Atzeni, A. S. Rab, G. Corrielli, E. Polino, M. Valeri, P. Mataloni, N. Spagnolo, A. Crespi, F. Sciarrino, and R. Osellame. Integrated sources of entangled photons at the telecom wavelength in femtosecond-laser-written circuits. *Optica*, 5(3):311–314, 2018.

[40] OzOptics. DTS0158 - Broadband polarization-entangled photon source, 2022. URL `www.ozoptics.com/ALLNEW_PDF/DTS0158.pdf`.

[41] H. R. Brown and R. Q. Twiss. A new type of interferometer for use in radio astronomy. *Philosophical Magazine*, 45(366):663–682, 1954.

[42] C. K. Hong, Z. Y. Ou, and L. Mandel. Measurement of subpicosecond time intervals between two photons by interference. *Physical Review Letters*, 59(18):2044–2046, 1987.

[43] A. Orieux. *Sources semiconductrices d'états à deux photons à température ambiante*. PhD thesis, Université Paris-Diderot - Paris VII, 2012.

[44] J. M. Dallesasse, J. N. Holonyak, A. R. Sugg, T. A. Richard, and N. El-Zein. Hydrolyzation oxidation of $Al_xGa_{1-x}As$ - AlAs - GaAs quantum well heterostructures and superlattices. *Applied Physics Letters*, 57(26):2844–2846, 1990.

[45] A. Fiore, S. Janz, L. Delobel, P. van der Meer, P. Bravetti, V. Berger, and E. Rosencher. Second-harmonic generation at $\lambda = 1.6$ μm in $AlGaAs/Al_2O_3$ waveguides using birefringence phase matching. *Applied Physics Letters*, 72(2942), 1998.

[46] H. Guillet de Chatellus, A. V. Sergienko, B. E. Saleh, M. C. Teich, and G. Di Giuseppe. Non-collinear and non-degenerate polarization-entangled photon generation via concurrent type-I parametric downconversion in PPLN. *Optics Express*, 14 (21):10060–10072, 2006.

[47] M. Fiorentino, S. M. Spillane, R. G. Beausoleil, T. D. Roberts, P. Battle, and M. W. Munro. Spontaneous parametric down-conversion in periodically poled KPT waveguides and bulk crystals. *Optics Express*, 15(12):7479–7488, 2007.

[48] A. Grisard, E. Lallier, and B. Gérard. Quasi-phase-matched gallium arsenide for versatile mid-infrared frequency conversion. *Optical Materials Express*, 2:1020–1025, 2012.

[49] L. Lanco, S. Ducci, J.-P. Likforman, X. Marcadet, J. A. W. van Houwelingen, H. Zbinden, G. Leo, and V. Berger. Semiconductor waveguide source of counter-propagating twin photons. *Physical Review Letters*, 97(17), 2006.

[50] P. Yeh A. Yariv. *Optical Waves in Crystals: Propagation and Control of Laser Radiation*. Wiley, 1984.

[51] P. Abolghasem, J. Han, B. J. Bijlani, and A. S. Helmy. Type-0 second order nonlinear interaction in monolithic waveguides of isotropic semiconductors. *Optics Express*, 18 (12601), 2010.

[52] K. A. Rutkowska, D. Duchesne, M. Volatier, R. Arès, V. Aimez, and R. Morandotti. Second harmonic generation in AlGaAs nanowaveguides. *Acta Physica Polonica A*, 120(4):725–731, 2011.

[53] F. Appas. *AlGaAs quantum photonics: from device engineering to quantum information protocols*. PhD thesis, Université Paris Diderot - Paris VII, 1 2022.

[54] S. Gehrsitz, F. K. Reinhart, C. Gourgon, N. Herres, A. Vonlanthen, and H. Sigg. The refractive index of $Al_xGa_{1-x}As$ below the band gap: accurate determination and empirical modeling. *Journal of Applied Physics*, 87(11):7825–7837, 2000.

[55] M. Ohashi, T. Kondo, R. Ito, S. Fukatsu, Y. Shiraki, K. Kumata, and S. S. Kano. Determination of quadratic nonlinear optical coefficient of $Al_xGa_{1-x}As$ system by the method of reflected second harmonics. *Journal of Applied Physics*, 74(1):596–601, 1993.

[56] G. Maltese. *Generation and manipulation of high-dimensional photonics states with AlGaAs chips*. PhD thesis, Université Paris Diderot - Paris VII, 5 2019.

[57] P. Yeh and A. Yariv. Bragg reflection waveguides. *Optics Communications*, 19(3): 427–430, 1976.

[58] A. S. Helmy. Phase matching using Bragg reflection waveguides for monolithic nonlinear optics applications. *Optics Express*, 14(3):1243–1252, 2006.

[59] F. Boitier, A. Orieux, C. Autebert, A. Lemaître, E. Galopin, C. Manquest, C. Sirtori, I. Favero, G. Leo, and S. Ducci. Electrically Injected Photon-Pair Source at Room Temperature. *Physics Review Letters*, 112:183901, 2014.

[60] Z. Yang, M. Liscidini, and J.E. Sipe. Spontaneous parametric down-conversion in waveguides: a backward Heisenberg picture approach. *Physics Review A*, 77(3): 033808, 2008.

[61] R. Regener and W. Sohler. Loss in low-finesse Ti:LiNbO3 optical waveguide resonators. *Applied Physics B*, 36:143–147, 1985.

[62] A. De Rossi, V. Ortiz, M. Calligaro, L. Lanco, S. Ducci, V. Berger, and I. Sagnes.

Measuring propagation loss in a multimode semiconductor waveguide. *Journal of Applied Physics*, 97:073105, 2005.

[63] R. L. Sutherland. *Handbook of Nonlinear Optics. Optical Science and Engineering.* New York: CRC Press, 2003.

[64] F. Appas, F. Baboux, M. I. Amanti, A. Lamaitre, F. Boitier, E. Diamanti, and S. Ducci. Flexible entanglement-distribution network with an AlGaAs chip for secure communications. *npj Quantum Information*, 7(118), 2021.

[65] R. Horn, P. Abolghasem, B. J. Bijlani, D. Kang, A. S. Helmy, and G. Weihs. Monolithic Source of Photon Pairs. *Physical Review Letters*, 108:153605, 2012.

[66] S. Tanzilli, H. De Riedmatten, W. Tittel, H. Zbinden, P. Baldi, M. De Micheli, D.B. Ostrowsky, and N. Gisin. Monolithic Source of Photon Pairs. *Electronics Letters*, 37: 26–28, 2001.

[67] T. Zhong, H. Zhou, R. D. Horansky, C. Lee, V. B. Verma, A. E. Lita, A. Restelli, J. C. Bienfang, R. P. Mirin, T. Gerrits, S. W. Nam, F. Marsili, M. D. Shaw, Z. Zhang, L. Wang, D. Englund, G. W. Wornell, J. H. Shapiro, and F. N. C. Wong. Photon-efficient quantum key distribution using time–energy entanglement with high-dimensional encoding. *New Journal of Physics*, 17:022002, 2015.

[68] R. T. Thew, S. Tanzilli, W. Tittel, H. Zbinden, and N. Gisin. Experimental investigation of the robustness of partially entangled qubits over 11 km. *Physical Review A*, 66:062304, 2002.

[69] R. C. Jones. A new calculus for the treatment of optical systems, I. Description and Discussion of the Calculus. *Journal of the Optical Society of America*, 31:488–493, 1941.

[70] D. B. Leviton and B. J. Frey. Temperature-dependent absolute refractive index measurements of synthetic fused silica. *arXiv*, 0805.0091, 2008.

[71] F. Kaiser, L. A. Ngah, A. Issautier, T. Delord, D. Aktas, V. d'Auria, M. P. De Micheli, A. Kastberg, L. Labonté, O. Alibart, A. Martin, and S. Tanzilli. Polarization entangled photon-pair source based on quantum nonlinear photonics and interferometry,. *Optics Communications*, 327:7–16, 2014.

[72] D. Oser. *Integrated silicon photonics for quantum optics.* PhD thesis, Université Paris Saclay (COmUE), 7 2019.

[73] P. Roztocki, B. MacLellan, M. Islam, C. Reimer, B. Fischer, S. Sciara, R. Helsten,

Y. Jestin, A. Cino, S. T. Chu, B. Little, D. J. Moss, M. Kues, and R. Morandotti. Arbitrary Phase Access for Stable Fiber Interferometers. *Laser & Photonics Reviews*, 15:2000524, 2021.

[74] M. O. Scully and M. S. Zubairy. *Quantum optics*. 1999.

[75] G. Ghosh, M. Endo, and T. Iwasaki. Temperature-dependent Sellmeier coefficients and chromatic dispersions for some optical fiber glasses. *Journal of Lightwave Technology*, 12:1338–1342, 1994.

[76] J. D. Franson. Nonlocal cancellation of dispersion. *Physical Review A*, 45(5):3126–3132, 1992.

[77] T. Zhong and N. C. W. Franco. Nonlocal cancellation of dispersion in Franson interferometry. *Physical Review A*, 88(2):02013, 2013.

[78] S. Hasinoff. *Photon, Poisson Noise*, pages 608–610. 01 2014.

[79] T. Ferrotti. *Design, fabrication and characterization of a hybrid III-V on silicon transmitter for high-speed communications*. PhD thesis, Ecole Centrale de Lyon, 12 2016.

[80] D. Liang and J. E. Bowers. Recent progress in lasers on silicon. *Nature Photonics*, 4 (8):511–517, 2010.

[81] R. E. Camacho-Aguilera, Y. Cai, N. Patel, J. T. Bessette, M. Romagnoli, L. C. Kimerling, and Jurgen Michel. An electrically pumped germanium laser. *Optics Express*, 20:11316–11320, 2012.

[82] S. Chen, W. Li, J. Wu, Q. Jiang, M. Tang, S. Shutts, S. N. Elliott, A. Sobiesierski, A. J. Seeds, I. Ross, P. M. Smowton, and H. Liu. Recent progress in lasers on silicon. *Nature Photonics*, 10(5):307–311, 2016.

[83] A. W. Fang, H. Park, O. Cohen, R. Jones, M. J. Paniccia, and J. E. Bowers. Electrically pumped hybrid AlGaInAs-silicon evanescent laser. *Optics Express*, 14(20): 9203–9210, 2006.

[84] L. Constans, S. Combrié, X. Checoury, G. Beaudoin, I. Sagnes, F. Raineri, and A. de Rossi. III–V/Silicon Hybrid Non-linear Nanophotonics in the Context of On-Chip Optical Signal Processing and Analog Computing. *Frontiers in Physics*, 7: 11–20, 2019.

[85] L. Yuan, L. Tao, H. Yu, W. Chen, D. Lu, Y. Li, G. Ran, and J. Pan. Hybrid

InGaAsP-Si Evanescent Laser by Selective-Area Metal-Bonding Method. *IEEE Photonics Technologies Letters*, 25(12):1180–1183, 2013.

[86] G. Kurczveil, P. Pintus, M. J. R. Heck, J. D. Peters, and J. E. Bowers. Characterization of Insertion Loss and Back Reflection in Passive Hybrid Silicon Tapers. *IEEE Photonics Journal*, 5(2):6600410, 2013.

[87] Y. L. Cao, X. N. Hu, X. S. Luo, J. F. Song, Y. Cheng, C. M. Li, C. Y. Liu, H. Wang, L. Tsung-Yang, G. Q. Lo, and Q. Wang. Hybrid III–V/silicon laser with laterally coupled Bragg grating. *Optics Express*, 23:8800–8808, 2015.

[88] G. Roelkens, L. Liu, D. Liang, R. Jones, A. Fang, B. Koch, and J. Bowers. Characterization of Insertion Loss and Back Reflection in Passive Hybrid Silicon Tapers. *Laser & Photonics Review*, 4:751–779, 2010.

[89] L. A. Coldren, S. W. Corzine, and M. Mashanovitch. *Diode lasers and photonic integrated circuits*. N.J: Wiley, 2nd ed. hoboke edition, 2012.

[90] X. Sun. *Supermode Si/III-V Lasers and Circular Bragg Lasers*. PhD thesis, California Institute of Technology, 4 2010.

[91] OzOptics. DTS0080 - Tapered and Lensed Fibers, 2020. URL `www.ozoptics.com/ALLNEW_PDF/DTS0080.pdf`.

[92] D. Taillaert, F. Van Laere, M. Ayre, W. Bogaerts, D. Van Thourhout, P. Bienstman, and R. Baets. Grating Couplers for Coupling between Optical Fibers and Nanophotonic Waveguides. *Japanese Journal of Applied Physics*, 45(8R):6071–6077, 2006.

[93] H. Trompeter, U. Peschel, T. Pertsch, F. Lederer, U. Streppel, D. Michaelis, and A. Bräuer. Tailoring guided modes in waveguide arrays. *Optics Express*, 11:3404–3411, 2003.

[94] X. Chen and H. K. Tsang. Polarization-independent grating couplers for silicon-on-insulator nanophotonic waveguides. *Optics Letters*, 36:796–798, 2011.

[95] A. Bozzola, L. Carroll, D. Gerace, I. Cristiani, and L. C. Andreani. Optimising apodized grating couplers in a pure SOI platform to -0.5 dB coupling efficiency. *Optics Express*, 23:16289–16304, 2015.

[96] J. Belhassen. *Monolithic and hybrid III-V/Si photonic devices for quantum information*. PhD thesis, Université Paris Diderot - Paris VII, 12 2018.

[97] K. Bücher, J. Bruns, and H. G. Wagemann. Absorption coefficient of silicon: An

assessment of measurements and the simulation of temperature variation. *Journal of Applied Physics*, 75:1127–1132, 1994.

[98] X. Xu *et al.* Near-infrared Hong-Ou-Mandel interference on a silicon quantum photonic chip. *Optics Express*, 21:5014–5024, 2013.

List of Acronyms and Constants

Acronyms

Acronym	*Description*
BPF	Band Pass Filter
BS	Beam Splitter
CAR	Coincidence-to-Accidental Ratio
CMOS	Complementary Metal-Oxide-Semiconductor
CW	Continuous Wave
DFG	Difference Frequency Generation
FDTD	Finite Difference Time Domain
FM	Faraday Mirror
FTIR	Fourier Transform Infrared Spectroscopy
FWHM	Full Width at Half Maximum
HBT	Hanbury-Brown-Twiss
HOM	Hong-Ou-Mandet
ICP	Inductively Coupled Plasma
IR	InfraRed
JSA	Joint Spectral Amplitude
JSI	Joint Spectral Intensity
MBE	Molecular Beam Epitaxy
NA	Numerical Aperture
NIR	Near InfraRed
OPA	Optical Parametric Amplification
PBS	Polarizing Beam Splitter
PC	Polarization Controller

Acronym	*Description*
PECVD	Plasma Enhanced Chemical Vapor Deposition
PGR	Pair Generation Rate
PM	Phase-Matching
QKD	Quantum Key Distribution
RIE	Reactive Ion Etching
SEM	Scanning Electron Microscope
SFG	Sum Frequency Generation
SFWM	Spontaneous Four-Wave Mixing
SHG	Second Harmonic Generation
SOI	Silicon-On-Insulator
SPD	Single Photon Detector
SPDC	Spontaneous Parametric Down-Conversion
TC	Temperature Controller
TCSPC	Time-Correlated Single Photon Counting
TDC	Time-to-Digital Converter
TE	Transvers Electric
TM	Transverse Magnetic

Constants

Variable	*Description*	*Value*
c	speed of light in vacuum	2.998×10^{8} m/s
ϵ_0	vacuum permittivity	8.854×10^{-12} $\mathrm{Nm^2/C^2}$
μ_0	vacuum permeability	1.257×10^{-6} $\mathrm{N/A^2}$
$\hbar$	reduced Planck constant	1.055×10^{-34} Js

List of Figures

List of Tables